

**SEAFLOOR SEDIMENT CORING AND MULTICHANNEL
SEISMIC STUDIES OF GAS HYDRATE, OFFSHORE VANCOUVER
ISLAND**

By

Yanpeng Mi

B.Sc., Peking University, Beijing, People's Republic of China, 1995

A Thesis Submitted in Partial Fulfillment of the
Requirement for the Degree of

MASTER OF SCIENCE

In the School of Earth and Ocean Sciences
University of Victoria

We accept this thesis as conforming to the required standard



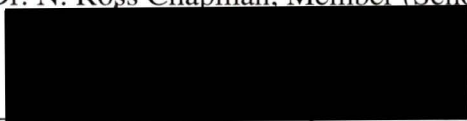
Dr. George D. Spence, Supervisor (School of Earth and Ocean Sciences)



Dr. Roy D. Hyndman, Member (Pacific Geoscience Centre, Geological Survey of Canada)



Dr. N. Ross Chapman, Member (School of Earth and Ocean Sciences)



Dr. David Mosher, Member (Pacific Geoscience Centre, Geological Survey of Canada)



Dr. Mel Best, External Examiner (Bemex Consulting International)

©Yanpeng Mi, 1998
University of Victoria

All right reserved. This thesis may not be reproduced in whole or part, by photocopy or other means, without the permission of the author.

Supervisor: Dr. George D. Spence

Abstract

Gas hydrate is an ice-like compound in which water molecules form a 3-D network trapping small gas molecules such as methane. Gas hydrates are important because they might be a significant future energy resource and because they may play a role in controlling global climate. The general objectives of this thesis are to determine the lateral variation of gas hydrate saturation in a small region on Cascadia Margin and to further understand the processes related to the formation of gas hydrate and free gas zone.

In the first part of this thesis, physical properties of seafloor sediment were measured in a region of hydrate occurrence on the middle continental slope offshore Vancouver Island. Seafloor sediment resistivity, velocity, bulk density, grain density, porosity and water content were measured. The measured physical properties complemented those of sediment cores from Ocean Drilling Program (ODP) Sites 889/890, in which the seafloor sediment is generally missing or incomplete. Porosity was found to vary consistently with resistivity and optimum Archie's Law parameters were used to predict seafloor sediment porosity. These parameters may be used in future resistivity surveys to provide seafloor porosity estimates. Sediment velocity was very close to that of seawater, which indicates that the reflection coefficient (RC) calculated from the seafloor bulk density can be safely used to constrain seismic RC. Measured bulk density appears to be lower in the deepwater region for the shallow sediments.

In the second part of the thesis, short-offset multichannel seismic (MCS) data collected in a tightly-spaced grid (400 m line separation) southwest of ODP Sites 889/890 were analyzed and interpreted. A 120 cubic inch airgun was recorded by a 24-channel ITC streamer with offsets ranging from 108 m to 292 m. Amplitudes were converted to RC values using a multiple/primary ratio method. A single conversion factor was calculated from seismic lines over several flat regions that are normally in the small slope basins. The seafloor RC determined from the seismic data was high in

the shallow water region (1200 m) and much lower in the deep sedimentary basin (2200 m), consistent with RC values calculated from bulk density values. This difference is mainly due to the tuning effect caused by the thickness variation of a soft mud layer covering the seafloor. Constrained by ground truth from measured seafloor impedance the seafloor RC derived from amplitude scaling can be safely used for transmission corrections in the BSR RC calculations.

The base of a gas layer below the BSR was clearly resolved on the western flank of a local topographic high. Forward modeling based on waveform matching showed subtle variations in the velocity and density structure that can generate a similar signature at the BSR and the base of free gas zone. Instead of a negative acoustic impedance boundary, the base of the free gas zone is positive. It is either caused by an interface between normal sediment and overconsolidated sediment or between free gas charged sediment and normal sediment. A clear density enhancement due to overconsolidation was observed below the BSR in core measurements from ODP site 892, where the BSR occurred at 74 mbsf. Unlike Site 892, however, the sediment bulk density below the BSR at ODP Sites 889/890 did not show a similar enhancement. This effect is probably because the BSR depth (225 m) at Sites 889/890 is much larger so that the sediment has lost more pore fluid through normal consolidation than the corresponding shallower sediment. The effect of overconsolidation on bulk density is too small to be resolved. Estimation of the gas saturation remains difficult because the velocity decreases dramatically with only a few percent of free gas. A maximum gas saturation of 5% pore space is suggested.

Gas hydrate saturation immediately above the BSR was calculated directly from the seismically derived BSR RC, with the assumption of a background velocity of 1600 m/s and average porosity of 50% at the depth of BSR. For RC ranging from 0 to 0.12, the gas hydrate saturation is no higher than 30%, typically 10% to 15% of the pore space.

Examiners:



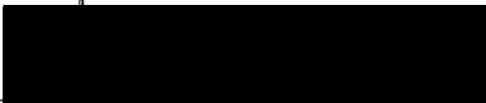
Dr. George D. Spence, Supervisor (School of Earth and Ocean Sciences)



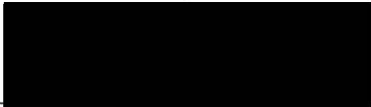
Dr. Roy D. Hyndman, Member (Pacific Geoscience Centre, Geological Survey of Canada)



Dr. N. Ross Chapman, Member (School of Earth and Ocean Sciences)



Dr. David Mosher, Member (Pacific Geoscience Centre, Geological Survey of Canada)



Dr. Mel Best, External Examiner (Bemex Consulting International)

TABLE OF CONTENTS

ABSTRACT.....	ii
TABLE OF CONTENTS	v
LIST OF TABLES	viii
LIST OF FIGURES	ix
ACKNOWLEDGEMENT	xii

CHAPTER ONE INTRODUCTION

1.1 Thesis Overview and Objectives	1
1.2 Gas Hydrate Chemical Structures, Stability Conditions and Formation Mechanism	2
1.3 Gas Hydrate and the Bottom Simulating Reflector.....	6
1.4 Natural Gas Hydrate Occurrence.....	7
1.4.1. Gas Hydrate in Polar Regions	7
1.4.2. Gas Hydrate in Oceanic Regions.....	8
1.5 Gas Hydrate Issues	9
1.5.1 Gas Hydrate as a Potential Energy Resource	10
1.5.2 Gas Hydrate As a Geologic Hazard	10
1.5.3 Effect of Methane hydrate on Global Climate	11
1.6 Geographic and Regional Plate Tectonics Setting of the Study Area.....	11
1.7 Previous Seismic Study of Cascadia Margin BSR	14
1.8 Introduction to the Survey Region	15

CHAPTER TWO PHYSICAL PROPERTIES OF SEAFLOOR SEDIMENTS

2.1 Core Physical Property Measurement	19
2.1.1 Resistivity Measurement	19
2.1.2 Compressional Velocity Measurement	24
2.1.3 Bulk Density, Grain Density, Porosity and Water Content Measurement	25

2.2 Source of Measurement Errors and Data editing	28
2.2.1 Porosity and Density Errors	28
2.2.2 Resistivity Errors	29
2.2.3 Velocity Errors	30
2.3 Physical Property Analyses	31
2.3.1 Index Physical Property Variation with Depth.....	31
2.3.2 Velocity	36
2.3.3 Prediction of Porosity and Velocity from Resistivity.....	37
2.4. Suggestions for Improvement in Methodology of Physical Property Measurement	39

CHAPTER THREE SEAFLOOR AND BSR REFLECTION COEFFICIENT STUDY

3.1 Data Acquisition	44
3.2 Seismic Data Processing.....	44
3.2.1 Data Processing Flow	44
3.2.2 Offset Dependent Receiver Ghost	46
3.3. Seafloor and BSR Amplitude Picking.....	57
3.4 Calculation of Reflection Coefficients	60
3.4.1 By Multiple/Primary Amplitude Ratio	60
3.4.2 By Amplitude Scaling	64
3.5 Distribution of Reflection Coefficients	66
3.6 Topography and Roughness Effects on Reflection Coefficient Calculation.....	70
3.7 Correlation of Seafloor Seismic Reflection Coefficient and Seafloor Density.....	74
3.8 BSR Depth Variation in Area 2	78
3.9 Tying Seismic Reflection Coefficients from MCS and SCS Data	81
3.10 Possibility of Seafloor Carbonate Pavement	83

CHAPTER FOUR GAS HYDRATE AND FREE GAS ZONE HARACTERIZATION

4.1 Free Gas Saturation Estimation	85
--	----

4.2 Gas Hydrate Saturation Estimation	85
4.3 Forward Modeling of Gas Hydrate and Free Gas Distribution Across BSR	89
4.4 Observation and Modeling of Second BSR below Primary BSR	91
4.5 Forward Modeling on the Second BSR, Determination of Velocity and Density Structure	94
4.5.1 Model Preparation	94
4.5.2 Modeling Results: Upper Bound of Thickness, Velocity and Density Contrast at the Second BSR	98
4.6 Interpretation of Velocity and Density Structures Across BSRs	98
4.6.1 Single Free Gas Zone and an Overconsolidated Layer	98
4.6.2 The Presence of Second Free Gas Zone	105
CHAPTER FIVE DISCUSSIONS AND CONCLUSIONS	107
BIBLIOGRAPHY	109

List of Tables

Table 2.1	The meaning of the symbols used in index property calculation.....	27
Table 2.2	Parameters used in fitting the porosity profile at ODP site 889/890	35
Table 3.1	Seismic data processing flow	45
Table 3.2	Amplitude of reflected wave at different thickness of soft layer	78

List of Figures

Figure 1.1 Unit cell of gas hydrate structures I and II.....	2
Figure 1.2 Gas hydrate stability zone under pure water and saline water.....	4
Figure 1.3 Gas hydrate formation mechanism at accretionary prism.....	5
Figure 1.4 Worldwide gas hydrate occurrence map.....	9
Figure 1.5 Geographic and regional tectonics regime of northern Cascadia subduction zone	12
Figure 1.6 The bathymetry and seismic track lines in Area2	13
Figure 2.1 MCS track lines and coring sites in Area 1 and Area 3	18
Figure 2.2 Resistivity of standard seawater.....	22
Figure 2.3 Standard sea water warming up process.....	24
Figure 2.4 Pure water compressional velocity	26
Figure 2.5 Index physical property variation with depth in data sets I and II	32
Figure 2.6 Index physical properties at Sites 889/890.....	33
Figure 2.7 Sediment velocity in Data Set I and II	37
Figure 2.8 Optimum fitting of Archie's Law on Data Set I and II	39
Figure 2.9 Correlation of predicted and measured porosity.....	41-43
Figure 3.1 Typical migrated seismic section in Area 2	47-56
Figure 3.2 Offset dependent receiver ghost wave.....	58-59
Figure 3.3 Picked seafloor and BSR amplitude in Area 2.....	61
Figure 3.4 Seafloor and BSR RC calculation using multiple/primary ratio	62
Figure 3.5 Seafloor amplitude conversion factor calculation	65

Figure 3.6 Seafloor and BSR reflection coefficient distribution.....	67
Figure 3.7 Map of seafloor raw amplitude and reflection coefficient.....	68
Figure 3.8 Map of BSR RC distribution (by amplitude scaling).....	71
Figure 3.9 Map of BSR raw amplitude.....	72
Figure 3.10 Method of calculating seafloor reflected amplitude with the presence of a soft mud layer.....	76
Figure 3.11 Seafloor reflected waveform and RC in the presence of a soft mud layer	77
Figure 3.12 Seafloor signature with different thickness of a soft mud layer.....	79
Figure 3.13 BSR time depth variation in Area 2.....	80
Figure 3.14 Correlation of seafloor RC from MCS and SCS data.....	82
Figure 4.1 Velocity and Poisson's ratio of gas-charged marine sediment	86
Figure 4.2 Gas hydrate saturation variation with BSR RC.....	89
Figure 4.3 Gas hydrate saturation immediately above the BSR in Area 2.....	90
Figure 4.4 Typical BSR reflection in Area 2.....	92
Figure 4.5 Observation of second BSR in Area 2	93
Figure 4.6 Sonic and VSP velocities	95
Figure 4.7 Time response, amplitude and phase spectrum of modeling input wavelet	97
Figure 4.8 Modeling results of velocity configuration I and II.....	99
Figure 4.9 Primary and second BSR waveform variation with the gradient velocity zone below the primary BSR.....	101
Figure 4.10 Two interpretations of the formation	

mechanism of the second BSR.....	103
Figure 4.11 GRAPE density, core bulk density and porosity at Site 892 D.....	104

Acknowledgements

First I would like to extend many thanks to my supervisor, Dr. George D. Spence. I could not have finished my thesis without his financial support and encouragement. It was his suggestion and advice that had been keeping me on the right track throughout the period of my thesis work. Also I want to direct my sincere thanks to my Committee Members, Dr. Roy Hyndman, Dr. Ross Chapman, Dr. Dave Mosher, and my External Examiner, Dr Mel Best, for their valuable suggestions, comments, helps and revisions to the thesis.

I am extremely grateful to Dr. Tianson Yuan, for his helps in seismic data processing/interpreting and scientific mapping; Dr. Rakesh Walia, for his valuable suggestions in many of the problems I encountered in my thesis work; and Mr. Nilanjan Ganguly, for his effort in data format converting and helps in computer programming.

I also wish to acknowledge the high quality physical property data (data set I) and some preliminary analyses provided by Tony Hewitt, and the seismic data collected by the scientific crew in survey PGC96004.

Seafloor Sediment Coring and Multichannel Seismic Studies of Gas Hydrate, Offshore Vancouver Island

Chapter 1. Introduction

1.1 Thesis Overview and Objectives

This thesis presents a detailed geophysical study of gas hydrates in the northern Cascadia subduction zone offshore Vancouver Island. By using high resolution multichannel seismic data and physical property analyses of seafloor sediment obtained in survey PGC 96004, we tried to determine the lateral variation of submarine gas hydrate in a small survey region on the Cascadia Margin and to further understand the gas hydrate/free gas zone formation mechanism. On the way of approaching these primary objectives, we also determined the seafloor physical properties, their correlation with seismically derived reflection coefficient, as well as the velocity/density structure across the base of gas hydrate stability zone. The study was divided into two major parts. In the first part, we tried to determine seafloor physical properties from core measurements in survey PGC96004 collected in the vicinity of ODP Sites 889/890, for which the shallow sub-seafloor portion is generally missing or incomplete. The velocity and density derived from the cores were used to determine seafloor reflection coefficients. The second part focused on the gas hydrate and free gas zone characterization determined from multichannel seismic data. Seafloor and bottom simulating reflector (BSR) reflection coefficients were estimated from the seismic data and analyzed in order to estimate hydrate saturation above the

BSR and free gas saturation below the BSR. Based on the observation of a secondary BSR below the primary BSR, forward modeling was carried out using 1D synthetic seismograms to determine the velocity and density structure at and below the base of the hydrate stability zone. Two formation models were proposed based on two possible velocity and density configurations derived from the forward modeling.

1.2 Gas Hydrate Chemical Structure, Stability Conditions and Formation Mechanism.

Clathrate gas hydrate is an ice-like nonstoichiometric inclusion compound with water molecules forming a three-dimensional network in which small atoms or molecules (guests) can be trapped in the empty voids. The structure differs from ice and depends on the guest molecules. Three different structural types have been characterized so far. The type I and II structures consist of 46 and 136 water molecules per unit cell, respectively (figure 1.1) [Makogon, 1974]. More recently, a third structure with hexagonal symmetry (structure H) has been identified, which is believed to be composed of 34 water molecules with three different type of cages [Ripmeester, 1994].

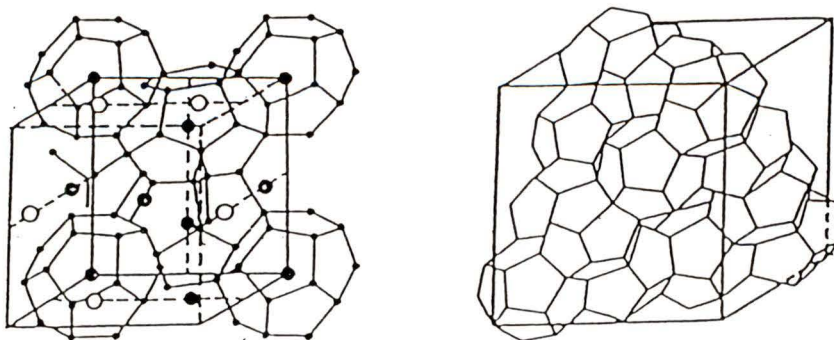


Figure 1.1 Unit cell of gas hydrate structures I and II, after *Makogon, 1974*.

The formation of gas hydrates requires two important conditions. The first one is appropriate pressure and temperature (P-T), for the given composition of the hydrocarbons or other hydrate forming constituents. Figure 1.2 shows the gas hydrate stability zone for pure water and for saline water. The formation of hydrate extracts freshwater from the pore fluids and expels salt to surrounding sediment [Hyndman and Davis, 1992]. With water extraction, the pore may collapse and the surrounding sediment may get overconsolidated [Hovland and Whiticar, 1995]. The second condition is that sufficient gas is provided, which is unfeasible without upward fluid migration. The amount of locally biogenerated gas is undoubtedly insufficient. Migration of fluid and the gas generation mechanism plays a key role in gas hydrate geology as it does in the conventional oil and gas industry. Migrating fluid flows in hydrate formations have been recognized by Brooks et al (1994). Geological structures favorable for rising fluid flow have been observed (faults, diapirs, landward-dipping bedding). Hydrate-bearing regions concurrently showed intensive sediment dewatering due to sediment horizontal compaction in accretionary prisms or delayed fluid expulsion in areas of high deposition rate. A conclusion has been drawn that migrating methane-bearing fluid is an important factor in gas hydrate formation (figure 1.3) [Hyndman and Davis, 1992].

The model of gas hydrate precipitation from upward migrating fluid flow is quite straightforward. Laboratory experiments on gas hydrate phase equilibrium with fluid and free gas showed that the solubility of gas decreased sharply with decreasing temperature when gas hydrate is present, opposite to the case when gas hydrate is absent at higher temperature [Ginsburg and Soloviev, 1997; Zatsepina and Buffet,

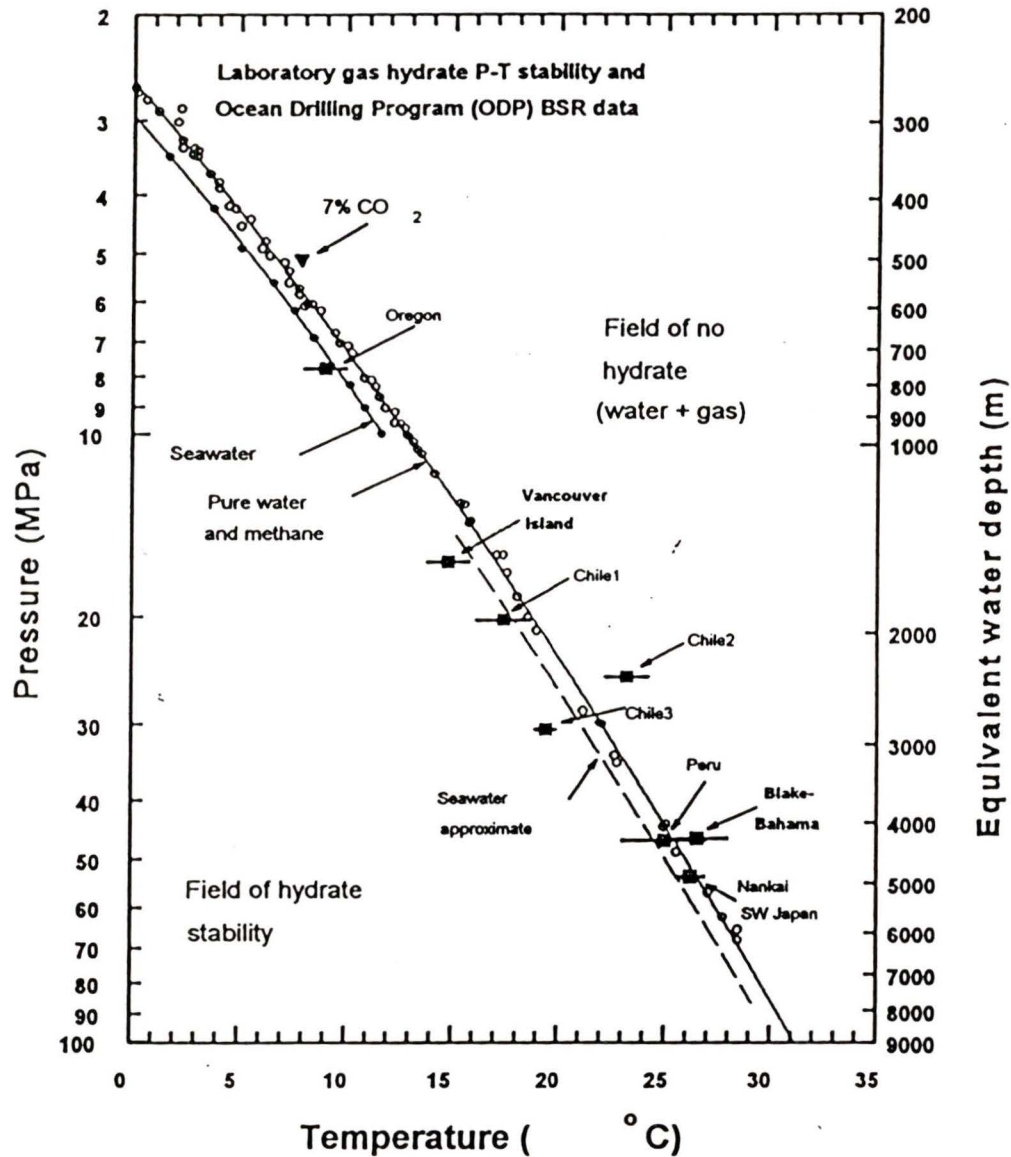


Figure 1.2 The pressure/temperature phase diagram for methane hydrate stability zone. The solid line sea water curve is from the equation-of-state computation for artificial seawater by *Englezos and Bishnoi*[1988] and *Dickens and Quinby-Hunt* [1994]. Extensive laboratory data for pure water/methane and limited data on the influence of CO₂ are also illustrated. Estimates of in situ P-T conditions at the base of hydrate stability field measured at DSDP/ODP sites agree very well with the laboratory data (from *Hyndman et al.*, 1994)

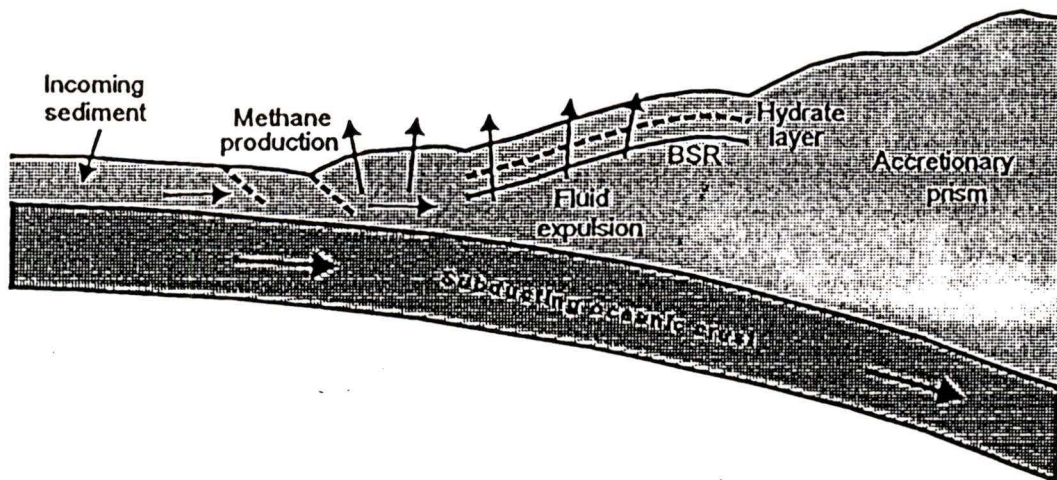


Figure 1.3 Illustration of the fluid expulsion model of hydrate BSR formation through methane removal from rising fluids that are tectonically expelled from an accretionary prism (Modified from *Hyndman and Davis*[1992]).

1997]. Due to this feature, the hydrate zone forms a gas geochemical barrier for the methane in upward-flowing pore fluids. Gas hydrate should precipitate at the base of the hydrate stability zone or just above it.

Another hydrate formation mechanism is water segregation by migrating gas which is associated with submarine gas-seepage fields. Examples are the gas hydrate zone associated with free gas flow discharging on the sea floor in the Gulf of Mexico [Brooks et al., 1987] and in the Okhotsk Sea [Ginsburg and Soloviev, 1997]. The calculated amount of free gas captured by the hydrate formation zone is five orders of magnitude lower than that escaping to the water column in the Okhotsk Sea. It appears that the gas does not have time to be stabilized as hydrate [Zonenshain et al., 1987]. This formation mechanism is different from that at the northern Cascadia accretionary prism.

1.3 Gas Hydrate and the Bottom Simulating Reflector (BSR)

Synthetic pure gas hydrate (methane hydrate) has a very high acoustic compressional wave velocity of 3730m/s [Pearson et al., 1983; Sloan, 1990]. Sediment with pore space fully or partially filled by this high velocity material has a higher velocity than normal sediment of the same type. If the region below the gas hydrate zone is either normal sediment or low-velocity gas-saturated sediment, then a strong negative polarity reflection is expected at the interface. The reflector is bottom simulating because its depth is mainly controlled by the geothermal gradient. In the absence of a recovery of actual hydrate samples, BSR is cited as the most common indicator of the base of the gas hydrate stability zone.

Unfortunately, *in-situ* information from the Deep Sea Drilling Program/Ocean Drilling Program (DSDP/ODP) on the BSR is very limited. Although early DSDP drilling penetrated the BSR in several holes, sampling and downhole logging were not sufficient to define the actual nature of the BSR and the P-T conditions in the sediment above and below. Much of the available information about the behavior and origin of the BSR has come from seismic reflection data analyses [Shipley and Didyk, 1981; Minshull and White, 1989; Miller et al., 1991; Hyndman and Davis, 1992; Hyndman and Spence, 1992; Yuan et al., 1996]. These studies involved forward modeling and inversion of seismic reflection data, the calculation of BSR reflection coefficients (RCs), reflection waveform modeling, and amplitude-versus-offset (AVO) analysis.

1.4 Natural Gas Hydrate Occurrence

Gas hydrate stability conditions are found in shallow sediments in two kinds of regions: (1) Continental margins, including continental shelves, at high latitudes where low surface temperatures are present ($<0^{\circ}\text{C}$) and (2) submarine continental slopes and rises where temperatures are above freezing but pressures are very high ($> 3\text{Mpa}$). Thus in polar regions, gas hydrate is found where temperature is low enough for onshore and offshore permafrost zones to be present. In offshore sediment of outer continental and insular margins, gas hydrate is found in water depths exceeding 300 m to 500 m, depending on bottom water temperature and the local geothermal gradient.

1.4.1 Gas Hydrate in Polar Regions

Low surface temperatures in polar regions promote the occurrence of permafrost and the resulting low temperature at depth leads to the appropriate P-T conditions for gas hydrate formation. Gas hydrate is known to be present at the Messoyakha gas field of the western Siberian platform and it is believed to occur in other permafrost areas in Russia, including the Timan-Pechora province, the eastern Siberian craton and the northeastern Siberian and Kamchatka areas.

Continental gas hydrate is also present in the North American Arctic. Well-log responses, consistent with the presence of gas hydrate, were obtained in the Mackenzie Delta; Sverdrup Basin, Arctic Platform, and Arctic Islands; and on the North Slope of Alaska. At a well between the Kuparuk River and Prudhoe Bay oil fields of the North Slope, pressure-core-barrel samples provided conclusive evidence for the presence of gas hydrate [Kvenvolden and Mcmenamin, 1980].

In addition to the onshore regions of permafrost in the Arctic, offshore permafrost is known to occur on the Beaufort Sea shelf of Canada. Studies on subsea permafrost and sea-level history have led to the inference that offshore relict permafrost may persist beneath any part of the Arctic shelf shoreward from about the 90-m isoplath [Rogers and Morak, 1980]. The distribution of gas hydrate associated with offshore permafrost is probably similar to that of gas hydrate associated with onshore permafrost.

The combined information from Arctic gas hydrate studies shows that in permafrost regions, gas hydrate exists at subsurface depths ranging from 130 m to 200 m. Gas hydrate may also occur in both onshore and offshore regions of Antarctica [MacDonald, 1983].

1.4.2 Gas Hydrate in Oceanic Regions.

Coring by the DSDP/ODP and marine geophysical surveys indicate that oceanic gas hydrate occurs in less than 10% of the total oceanic area. A compilation of worldwide gas hydrate occurrence was first undertaken by Kvenvolden and MacMenamin (1980). By 1982, the number of locations where subaquatic gas hydrate was identified increased to 18, and by 1990 this number increased to 36. An updated gas hydrate distribution map is shown in figure 1.4.

Among these locations, gas hydrate has been recovered at 14 locations, providing irrefutable evidence of subaquatic gas hydrate occurrence. Among the DSDP sites all around the world, gas hydrate has been recovered at nine sites (Offshore Peru, Costa Rica, Guatemala, Mexico, southeastern United States, western

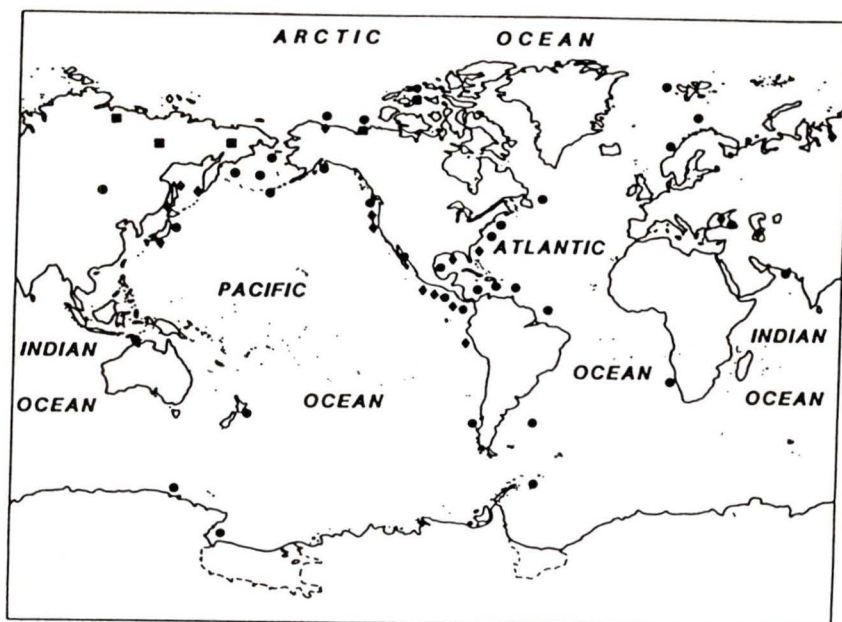


Figure 1.4 Worldwide locations of known and inferred gas hydrate deposits in continental (permafrost) regions (squares) and in oceanic (aquatic) sediments (circles). Locations where gas hydrate has been recovered are indicated (diamonds). Modified from *Kvenvolden, 1993*.

United States and Canada, two locations from offshore Japan and in the Gulf of Mexico). In some cases, only a single example of gas hydrate was recovered, but more often gas hydrates were observed in several cores in a given area. For example, in the Gulf of Mexico, gas hydrate was recovered at a DSDP site and at 13 piston core stations separated by more than 300 km. Offshore from Guatemala, gas hydrate was observed in cores at five drilling sites. In the southern Caspian Sea, gas hydrate has been found in 24 cores from two areas 40 km apart.

1.5 Gas Hydrate Issues.

The gas hydrate became known to chemists around the early part of 19th century [Sloan, 1990] and started to draw the attention of the petroleum industry in

the 1930s when this substance was discovered to be the cause of pipeline blockage during transmission of natural gas. It has been increasingly evident that naturally occurring gas hydrate is a significant physical-chemical component of the shallow geosphere and is a societally relevant issue in three ways: resources, hazard and climate.

1.5.1 Gas Hydrate as a Potential Energy Resource.

Due to the enormous amount of methane trapped in gas hydrates and its wide geographical distribution, gas hydrate is considered to be a major potential energy resource. The energy volume of methane gas hydrate is ten times greater than other unconventional sources of gas such as coal beds, black shales and deep aquifers and two to five times greater than the energy density of conventional natural gas [MacDonald, 1990]. However, the current expenses of gas recovery methods are prohibitively high so that gas hydrate can not be considered a feasible energy resource until the energy provided by recovered methane exceeds the energy cost of recovery.

1.5.2 Gas Hydrate As a Geologic Hazard.

Gas hydrate is considered a geologic hazard because of its possible connection to submarine slides and slumps. Lowering of sea level can decrease the stability of gas hydrate. In adjusting to the new pressure and temperature conditions, the gas hydrate dissociates to produce an enhanced fluidized layer at the base of gas hydrate. Submarine slope failure can follow, giving rise to debris flows, slumps, and slides, accompanied by the release of methane gas into the water column.

1.5.3 Effect of Methane hydrate on Global Climate.

Methane is a very important trace component of the atmosphere, having a current global concentration of $6.9 \times 10^{12} \text{ m}^3$, about one-half of the minimum amount of methane estimated by the Potential Gas Committee to occur in gas hydrate of Arctic permafrost regions [Potential Gas Committee, 1981]. The concentration of methane in the atmosphere is increasing at the rate of 1% per year [Watson et al, 1990]. Methane is radiatively active and therefore it is a “greenhouse” gas that has a global warming potential 20 times larger than an equivalent weight of carbon dioxide when integrated over a 100 year span of time [Shine et al, 1990].

The earth’s atmosphere has a wide variety of source sinks for methane, including gas hydrate, which exists in equilibrium with its environment and is affected by changes in pressure and temperature. The amount of methane trapped in gas hydrate is 3000 times that in the atmosphere and its disassociation can produce a significant impact on the atmosphere composition.

1.6 Geographic and Regional Plate Tectonics Setting of the Study Area

The study area is located on the northern Cascadia accretionary margin, which is dominated by the relative motions of three main lithospheric plates: the large Pacific and North America Plates and the intervening Juan de Fuca Plate (figure 1.5). Immediately northeast of the survey region are ODP Sites 889/890 and the adjacent single channel seismic region for the survey carried out in 1993 (figure 1.6).

Offshore northern Vancouver Island, the newly formed Explorer plate moves at a rate of $10\text{-}25 \text{ mm a}^{-1}$ towards the North America plate [Hyndman et al., 1979;

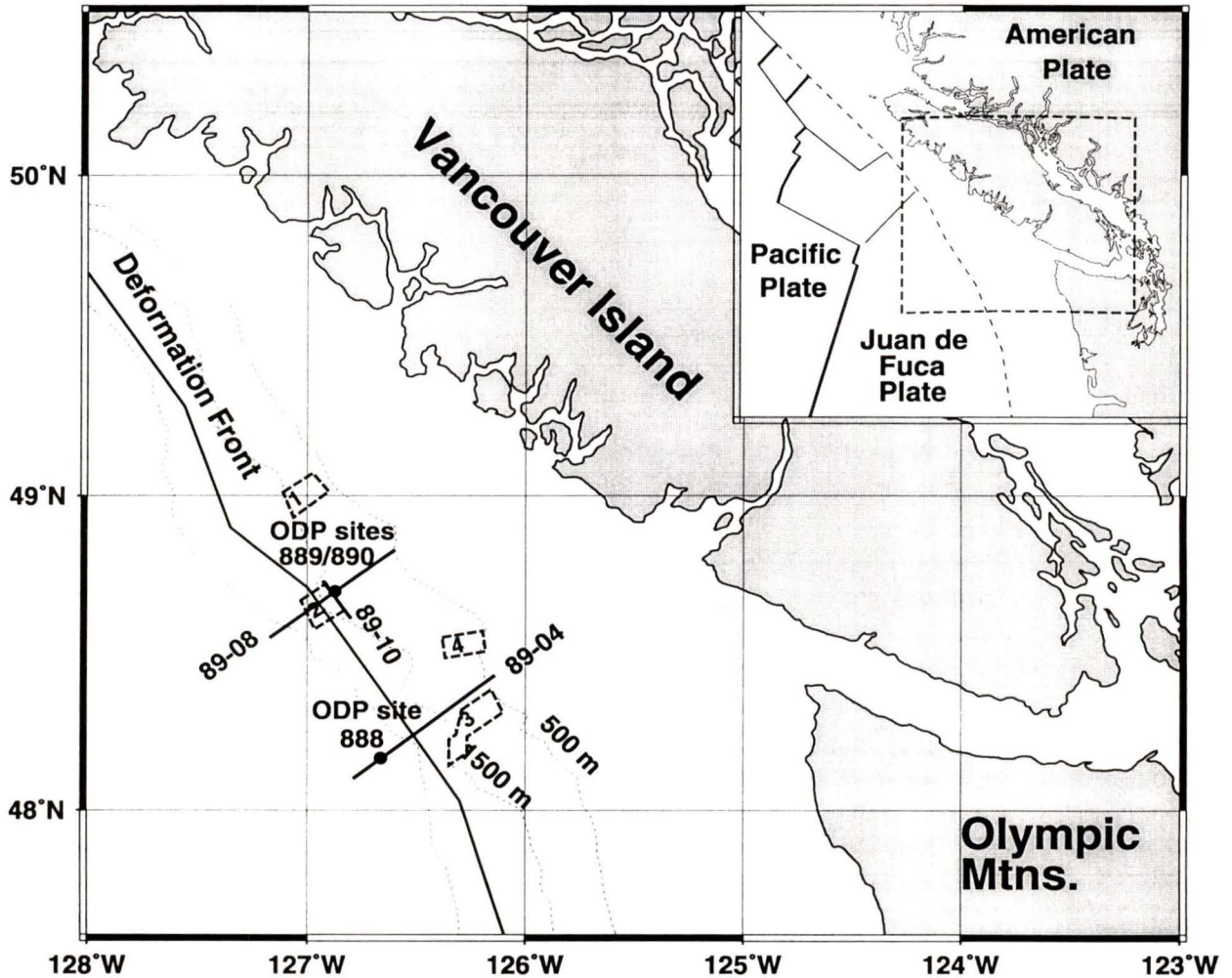


Figure 1.5 Geographic and regional tectonics regime of the northern Cascadia subduction zone. Solid thick lines are large offset multichannel seismic lines. The 4 subareas of Survey PGC96004 are labeled as 1,2,3 and 4. Area 2 is the study area of this thesis.

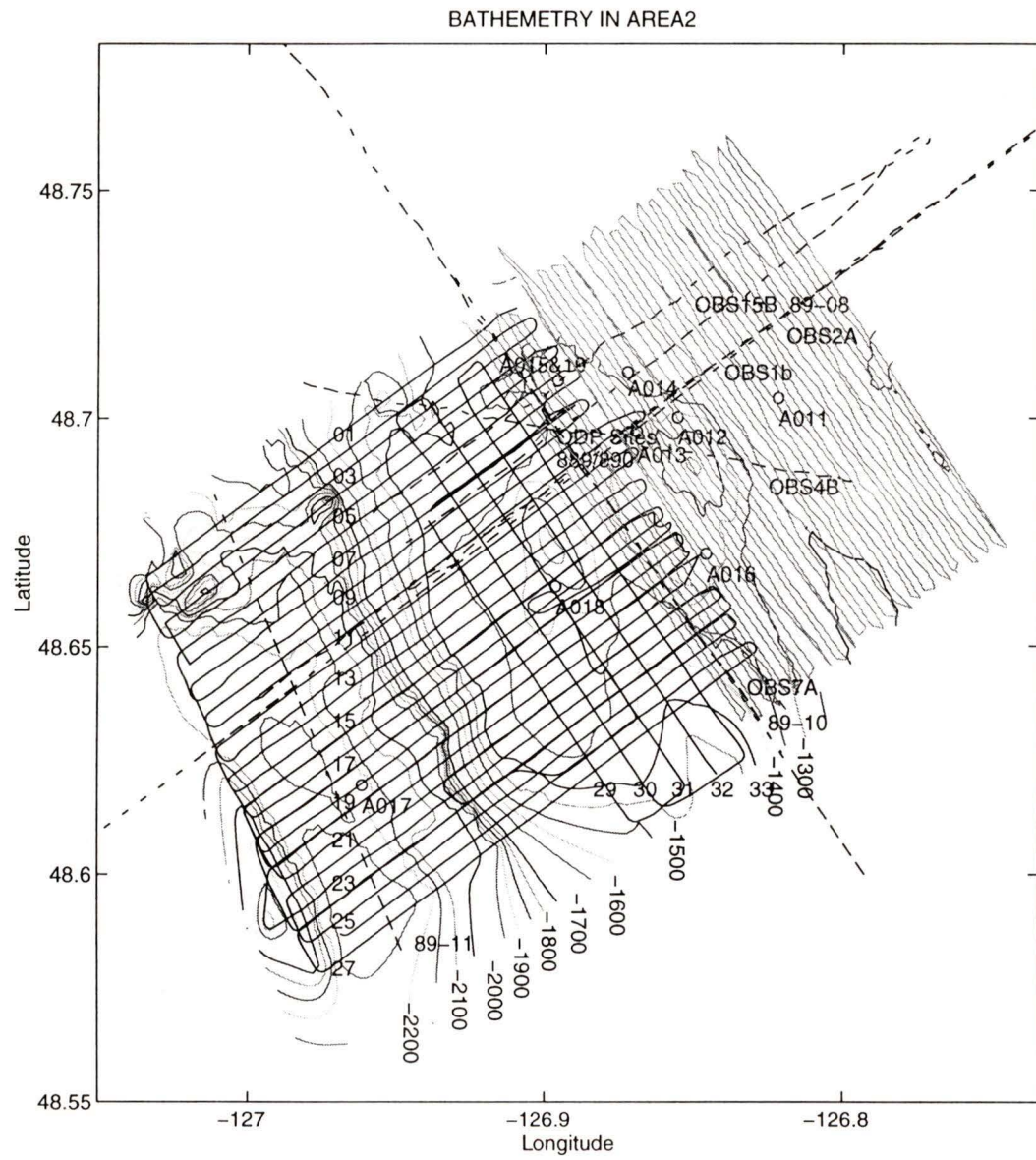


Figure 1.6 Bathymetry and seismic survey track lines in Area 2 and the adjacent single channel survey area. Black and gray lines are MCS and SCS track lines.

Davis and Riddihough, 1982; Riddihough, 1984]. The Juan de Fuca plate, which lies south of the Nootka transform boundary, is subducted orthogonal to the southern Vancouver Island margin at a rate of 45 mm a^{-1} [Riddihough,1984]. The geometric balance between the subducting Explorer and Juan de Fuca plates is maintained by the Nootka transform boundary [Hyndman et al., 1979; Davis and Hyndman,1989]. According to the offshore magnetic anomalies, the age of the oceanic crust at the deformation front near the study area is about 6 Ma [Riddihough, 1984]. The subduction angle of the Juan de Fuca plate beneath the North America plates is about $3^{\circ}\sim 4^{\circ}$ at the deformation front but steepens to 11° beneath the continental shelf. Sediment scraped off the Juan de Fuca plate and young terrigenous sediment has formed a 60 km wide accretionary prism (figure 1.3) over the past 43 Ma [Davis and Hyndman,1989; Hyndman et al., 1990].

1.7 Previous Seismic Studies of Cascadia Margin BSR

Near ODP Sites 889/890 on the lower slope of the Northern Cascadia margin, offshore Vancouver Island, Hyndman and Spence [1992] concluded that the BSR was produced mainly by a high-velocity zone, with a transitional top and a sharp base interface. They also concluded that 20-30% of the pore space was filled with high velocity hydrate if the BSR contrast was the sole result of high velocities of gas hydrate. AVO analyses could not confirm whether a free gas layer is present below the BSR, but a thin layer was allowed in the forward modeling.

In ODP Leg 146, a strong BSR was penetrated at three different locations and no gas kick or other hazardous event occurred during the drilling process. This result

proved that even a strong BSR is not necessarily associated with a high-pressure gas reservoir. However, a low pressure gas layer that does not cause any gas kick may be present [Ginsburg and Soloviev, 1996].

The coarse-clastic accretionary wedge on the northern Cascadia margin and the widespread BSR within the accretionary wedge beneath the continental slope were well imaged by the 1989 multichannel reflection data [Spence et al, 1991a, 1991b; Hyndman et al., 1994]. BSR and finer scale recent sediment strata are also well defined by a later multichannel seismic survey (PGC96004).

BSR reflection coefficients have been used to calculate the gas hydrate saturation above the BSR [Fink and Spence, 1998]. The model mostly applied for such analysis is the “time-average” model, which is appropriate for the gas hydrate saturated sediments.

1.8 Introduction to the Survey Region

In September 1996, a collaborative survey (PGC96004) sponsored by the School of Earth and Ocean Sciences (SEOS), University of Victoria and the Pacific Geoscience Centre (PGC), Geological Survey of Canada, was carried out along the continental slope of the northern Cascadia subduction zone. The project was aimed at the study of natural gas hydrates offshore Vancouver Island. The survey was carried out in four areas (figure 1.5). Area 2 is the primary focus of this thesis. In Area 2, water depth ranges from 1250 m to 2200 m (figure 1.6) The central part is a slope region with maximum seafloor slopes of about 15°. The western part of this area is a deep sedimentary basin, where recent sediment strata provide well-defined reflections

on seismic data. The shallow water region is mainly composed of accreted sediments which are often completely seismically transparent due to intense deformation [Davis and Hyndman, 1989], so that there is generally a lack of seismic reflectivity above and below the BSR. The bottom simulating reflector (BSR) is clearly visible in the shallow water region. It is generally obscured, however, by reflections from stratigraphic horizons in the deep sedimentary basin and in the local small basins in the shallow water region.

A total of about 300 km of 24-channel seismic data and 8 piston cores were collected in Area 2. The four piston cores collected from Area 1 and five from Area 3 were also analyzed for this thesis. Detailed description of experimental parameters for coring are addressed in the beginning of Chapter 2, while seismic data acquisition is described at the beginning of Chapter 3.

In the area immediately east of Area 2 (figure 1.6), single channel seismic (SCS) data were collected in 1993 in a direction parallel to the continent margin [Fink, 1995; Spence et al, 1995; Fink & Spence, 1998]. Line 89-08, 89-10, 89-11 are multichannel reflection lines shot in 1989 as part of the site survey for ODP Leg 146 on the northern Cascadia convergent margin [Spence et al, 1991a, 1991b; Yuan, 1994]. Line 89-08 coincides with Line 12 in Area 2 and Line 89-10 runs in a cross-line direction over the topographic high.

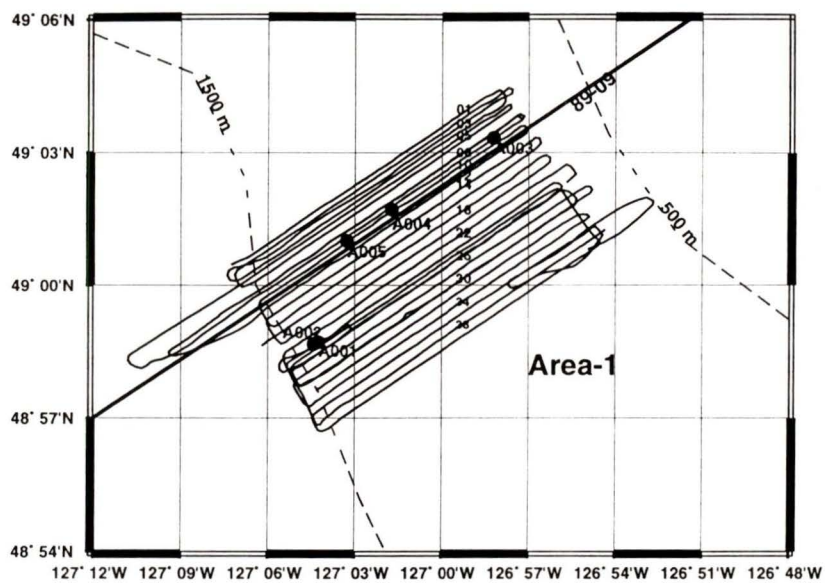
Chapter 2. Physical Properties of Seafloor Sediments

Introduction

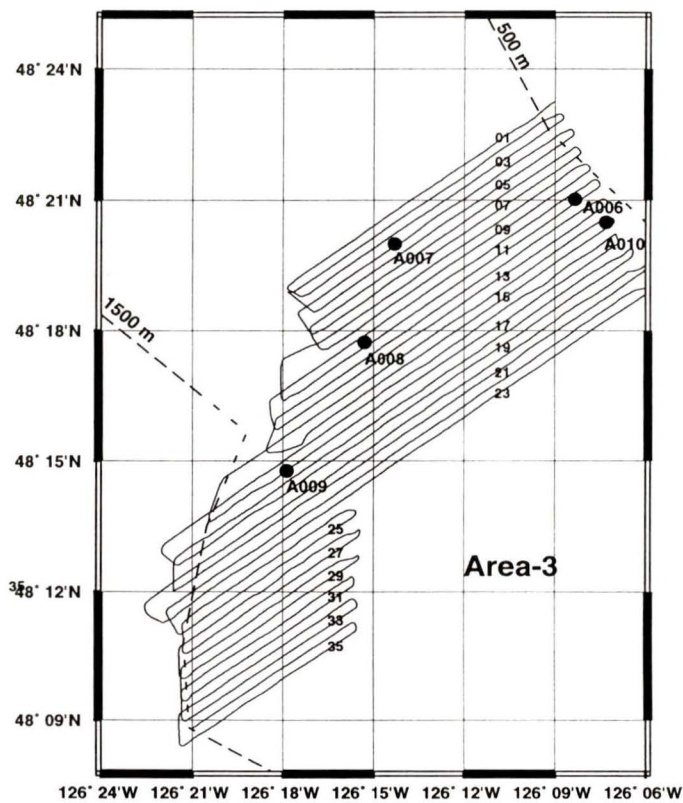
In Cruise PGC96004, coring was carried out in an effort to determine the seafloor sediment properties. The measurement of seafloor density and seismic velocity derived from the cores allowed us to calibrate the seismically derived seafloor RC, which then provided a reliable means of calculating the BSR RC. A secondary goal was to search for evidence of seafloor carbonate cementation. Previous evidence of carbonate cementation, based on high seafloor RC derived from SCS data in the adjacent region to the east, was discussed by Fink [1995]

A total of 18 piston cores were recovered in the four survey areas in water depths ranging from 500 m to 2200 m. Several gravity cores, sampled by a trigger corer attached to the main coring complex, were also collected. There were 8 cores recovered from Area 2 (figure 1.6), 5 cores from Area 1 (figure 2.1a) and 5 cores from Area 3 (figure 2.1b).

Recovered piston cores, with lengths from about 5 m to 8 m, were cut into sections of 1 m in length for storage convenience. Most of the core sections were well preserved, except that some of the thick sand layers (20~30 cm) in several sections were liquified due to transportation and vibration during core splitting. Sand layers in several sections were severely dewatered due to drainage and damage to the liners at the time of coring. Physical properties from these layers were not used in subsequent analyses.



(a)



(b)

Figure 2.1 MSC track lines and coring sites in Area 1 and Area 3, Survey PGC 96004.

Physical property measurements were carried out in the sediment lab at the Pacific Geoscience Centre (PGC) of the Geological Survey of Canada (GSC). The work was partitioned into two stages. The first part, from October to November 1996, focused on cores 4, 5, 8, 12, 14, 16 and 18 which had high recovery quality. The second part, from late June to late July 1997, completed the analysis of the rest of the cores. Measured and derived physical properties were resistivity (voltage readings, then converted to resistivity and formation factor), compressional wave velocity, bulk density, grain density, water content and porosity. For the convenience of data analyses, data from the earlier and later stage are referred as data set I and data set II in this thesis.

2.1 Core Physical Property Measurement

2.1.1 Resistivity Measurement

Resistivity measurements were carried out at an interval of 10 cm on each core section. Liquified sand layers and seriously disturbed sediment samples gave unstable values. The data from these layers were not used in further data analyses.

The resistivity measuring equipment consisted of three components: an electrical probe, a constant current supply and a high precision voltmeter. The resistivity gear used in this measurement was built at PGC based on a design by Dave Heffler (Atlantic Geoscience Centre, 1992).

The probe contained four pins made from standard gold plated electrical connector strips separated by 0.1 inch (0.254 cm). The pins could be inserted into the sediment to a depth of 3 mm. A 163.84 Hz \pm 5V AC square wave generator was

connected to the outer two pins through two 4.99K(1%) current limiting resistors. The electronic components were only accurate to about 10% so that system calibration was required if long term accurate readings are required. The inner two pins were cabled to a Fluke model 45 digital voltmeter. The voltmeter readings were logged manually. Equipment calibration was carried out with 5-ohm and 1-ohm calibrating resistors. Because neither the voltage nor resistance of these two calibrating resistors varied sufficiently to give errors comparable with other error sources, no equipment static shift correction was applied.

Sediment resistivity was normally converted to formation factor for further analyses. The formation factor is defined as:

$$FF = \frac{R_{sample}}{R_{seawater}}, \quad (2.1)$$

where R_{sample} and $R_{seawater}$ are sediment and seawater resistivity, respectively.

Two methods were used to convert the sample voltage readings to formation factors, as discussed below.

Method I: Calculating resistivity directly from raw voltage reading.

Sample resistivity R_{sample} was calculated with:

$$R_{sample} = \frac{m Volt_{sample}}{C}, \quad (2.2)$$

where the conversion factor $C=0.417 \times 51.5=20.5$ is an equipment-dependent constant.

Seawater resistivity was calculated with:

$$R_w = \frac{l}{a(b + cT + dT^2 + eT^3)}, \quad (2.3)$$

where $a=4.2914$, $b=0.6766097$, $c=0.0200564$, $d=0.0000001104259$ and $e=0.00000069698$ and T is temperature in Celsius. Sediment formation factor was then calculated from equation 2.1.

The resistivity of standard seawater, with salinity of 34.999‰, was measured as the samples warmed up from 7°C to 20°C (figure 2.2). The measured values were compared with the theoretical values from equation 2.3. The measured resistivity values were very close to the theoretical values for temperature less than 14°C, but at greater temperatures the measured values were larger, deviating from the theoretical values by 4% at 20°C (figure 2.2). Due to the difference between theoretical and real values at temperatures higher than 14°C, as well as the uncertainty in conversion factor selection, we employed the second method defined below.

Method 2: Calculating Formation Factor directly from voltage readings:

Rather than convert the voltage readings to resistivity and then to formation factor, voltage readings of standard seawater were used directly to calculate formation factor with the following formula:

$$FF = \frac{m \text{ Volt}_{\text{sample}}}{m \text{ Volt}_{\text{seawater}}}. \quad (2.4)$$

The resistivity (voltage reading) of standard seawater was measured with exactly the same equipment. The shape of the container simulated the liner containing

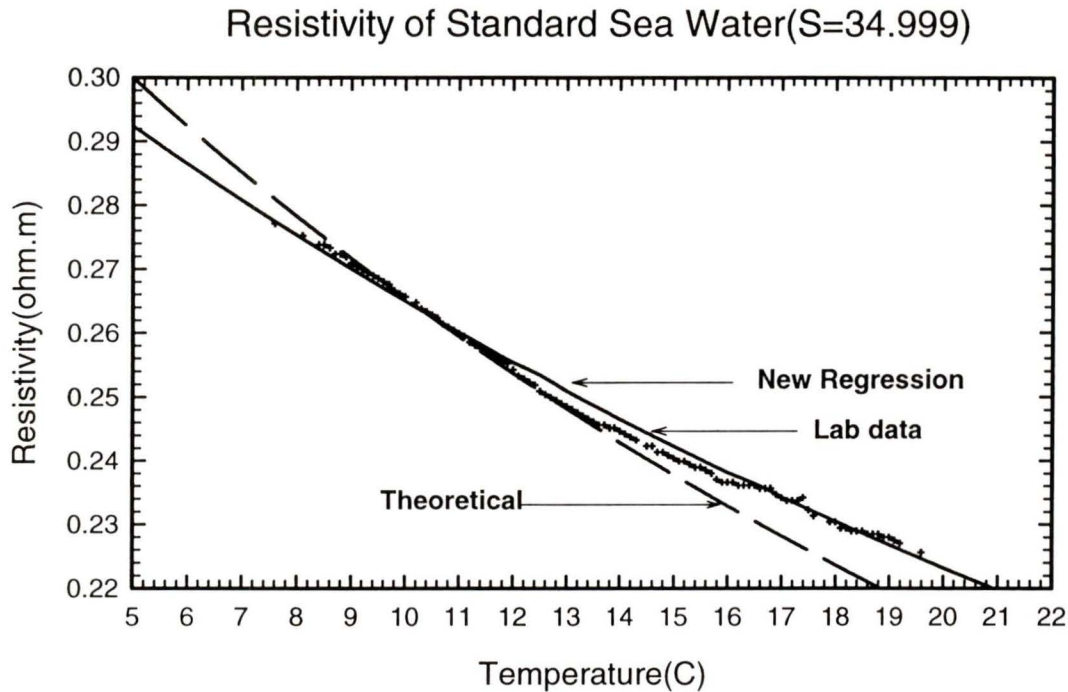


Figure 2.2 Standard seawater (S=34.999) resistivity measurement. Resistivities were converted from mVolt readings using equation 2.2. Theoretical seawater resistivity from equation 2.3 varied by up to 4% from the measured values. The empirical relationship was used to interpolate seawater resistivity values beyond 19.5°.

the sediments. The initial temperature was set to 5°C, roughly the storage temperature. The seawater was heated up naturally to the room temperature, approximately 22°C. The water sample was covered by plastic film to reduce evaporation. However, at temperatures greater than 19.5°, the rate of warming was significantly reduced and evaporation may have been a very important error source due to longer exposure to the air. No seawater resistivity data were collected for temperatures greater than 19.5°. To cover the entire temperature range of sediment resistivity measurement, which was from 6°C to 23°C, an empirical formula was interpolated from the seawater resistivity measurements:

$$mV_{olt}_{std_seawater} = \frac{6.83383 - 0.96865T + 0.03368T^2}{1 - 0.11872T + 0.00167T^2 + 0.000117T^3}, \quad (2.5)$$

where $mVolt_{std_seawater}$ is the voltage readings of 34.999‰ standard seawater at temperature T . Figure 2.2 shows the resistivity converted from this equation, using a conversion factor of 20.5. This regression equation was only used for temperatures greater than 19.5°.

Unfortunately, temperatures were not recorded for resistivity measurement in data set I, although it was recorded about 15 minutes later during the velocity measurement. The seawater warm-up process was recorded to obtain the temperature 15 minutes before the sediment velocity measurements. This procedure assumed that the seawater sample and the sediment followed the same warm-up process, although that of sediment should be slower due to its lower thermal conductivity.

The recorded seawater warming-up process is shown in figure 2.3. From 8°C to 14°C, which corresponds to the data set I temperature range, the seawater warmed up at the rate of 2°C per 15 mins. Thus 2 degrees was subtracted from the velocity temperatures to give the temperature of the resistivity measurement.

Temperatures of the seawater resistivity measurements were measured with a Radioshack thermometer, which was also used in measurements on the sediment samples. A more accurate digital Beckman thermometer was also used in the seawater measurements. Temperatures from the Radioshack thermal meter were generally 0.5°C lower. This error caused less than 1% errors in calculating of sediment formation factors, well within the measurement error range.

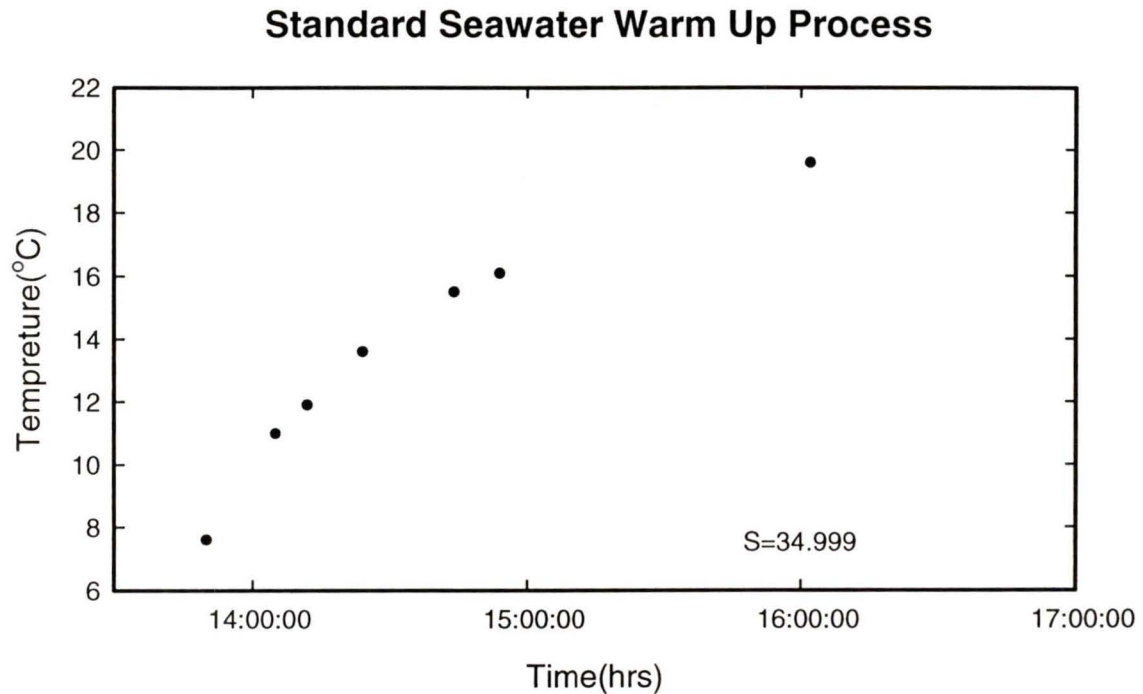


Figure 2.3 Standard seawater warming up process. Temperature difference between resistivity and velocity measurement in data set I was 2°C, corresponding to a time difference of 15 minutes between them.

2.1.2 Compressional Velocity Measurement

Compressional velocity measurements were made on each core at an interval of 10 cm, offset from the location of the resistivity measurements by 3.75 cm. The probe consisted of a transmitter arm and a receiver arm separated by 7.5 cm. The transmitter arm was connected to a 10 Hz square wave generator and the receiver arm was connected to channel 2 of an oscilloscope. The square wave generator also sent signals into channel 1 of the oscilloscope to display a reference zero time. The time difference between the reference zero time on channel 1 and the first break on channel 2 provided the one-way travel time between the probes and was picked manually to calculate the compressional wave velocity. This method was discussed by Courtney et al [1993].

Before measurement on each section, the travel time in double-distilled water was measured to calibrate the distance between the two probes. This compensated for the variation of sediment velocity with temperature, and also for possible variation in probe distance with temperature. The compressional velocity of the sediment samples was calculated with:

$$V_{p_{sample}} = \frac{t_{water}}{t_{sample}} \times V_{p_{water}}, \quad (2.6)$$

where $V_{psample}$ and V_{pwater} are the compressional velocity of sample and double distilled water respectively. The pure water velocity values used in conversion from sample travel time to velocity followed the measurements done by Clark [1966], as shown in Figure 2.4.

In practice, some of the cores were seriously cracked. These cracks did not affect the bulk density measurement because most of the density samples could be taken between cracks, but they significantly reduced the sample velocity and scattered the acoustic energy. When the first break was too weak to pick due to cracks, a very small amount of free water was added to fill up the cracks to improve signal transmission. The effect of adding water to cracks has small effect on the sample velocity for the similarity of their velocity.

2.1.3 Bulk Density, Grain Density, Porosity and Water Content Measurement

The volume samples were taken with a 9.718 cm³ volume sampler at an interval of 10 cm on each core. The volume samples were dried with a Fisher IsoTEMP Oven 338 running at 96°C for 24 hours. The mass of both wet and dried

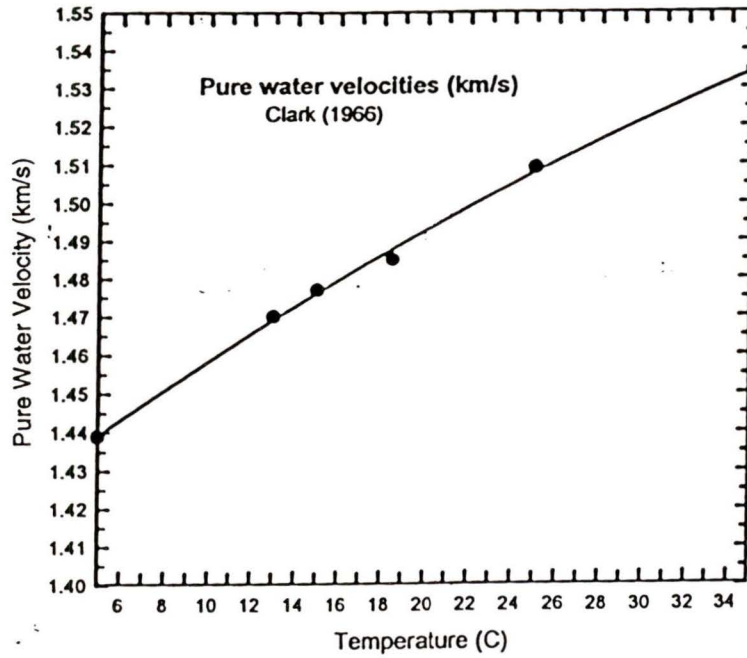


Figure 2.4 Pure water compressional wave velocity [Clark 1966]. Black dots and solid line are measured pure water velocities and theoretical curve.

samples were measured with a Mettler AE 163 balance. The related formulae used in calculating the bulk density, grain density, porosity and water content are listed below (Westbrook et al, 1994):

$$\rho_{w_sample} = \frac{M_{w_sample}}{V_{sampler}}, \quad (2.7)$$

$$M_{pore_fluid} = M_{w_sample} - M_{grain}, \quad (2.8)$$

$$V_{pore_fluid} = \frac{M_{pore_water}}{\rho_{pore_fluid}}, \quad (2.9)$$

$$W_{dry} = \frac{M_{w_sample} - M_{grain}}{M_{grain}}, \quad (2.10)$$

$$V_{grain} = V_{sampler} - V_{pore_fluid}, \quad (2.11)$$

$$W_{wet} = \frac{M_{w_sample} - M_{grain}}{M_{w_sample}}, \quad (2.12)$$

$$\phi = \frac{V_{pore_fluid}}{V_{sampler}}, \quad (2.13)$$

$$\rho_{grain} = \frac{M_{grain}}{V_{grain}}. \quad (2.14)$$

The meaning of the symbols used in these formulas is listed in table 2.1:

Symbols	Parameter
ρ_{pore_water}	Pore fluid density, about 1024 kg/m ³ .
ρ_{w_sample}	Density of wet sample.
ρ_{grain}	Density of mineral grain.
M_{pore_fluid}	Mass of pore fluid.
M_{w_sample}	Mass of wet sample.
M_{grain}	Mass of dried sample.
V_{pore_fluid}	Volume of pore fluid.
$V_{sampler}$	Volume of sampler, 9.718cm ³ .
V_{grain}	Volume of mineral grains.
W_{wet}	Water content by percent of wet mass.
W_{dry}	Water content by percent of dry mass.
ϕ	Porosity

Table 2.1 Symbols used in formula 2.7 to 2.14.

2.2 Source of measurement errors and data editing.

Dewatering was the major source of the systematic error in the results. Pore fluid leakage from some core sections, mostly those sections with thick sand layers, was observed. Evaporation was also suspected to be the another important way of losing pore fluid. Fluid migration within a core section (for example: core 3) tends to expel pore fluid upward so that the sediments in the top of a core section had a higher porosity.

2.2.1 Porosity and Density Errors

The error in porosity measurement caused by the dewatering can be estimated from the difference in the water content (percent of dry mass) between data sets I and II (figure 2.5 i-j). The values of water content (percent of dry mass) in data sets I and II were roughly centred at 59% and 52% of dry mass from 2 mbsf to 5.5 mbsf, respectively. The percentage of lost water (of total water mass) can be roughly calculated with:

$$W_{d1} = \frac{M_1}{D_1 - M_1},$$

$$W_{d2} = \frac{M_1(1 - x/100)}{D_1 - M_1}, \quad (2.15)$$

where W_{d1} and W_{d2} are average water contents in data set I and II, D_1 and M_1 are the mass of wet samples and mass of pore fluid before dewatering, x is the percentage of lost water. It turned out from the calculation that about 11.8% of pore water was lost through leakage and evaporation.

Dewatering also led to increased bulk density values. For typical glacial clay with original porosity of 65%, bulk density increased from 1630 kg/m³ to 1760 kg/m³,

while porosity was reduced to 59% if 11.8% of pore fluid reduction was assumed. This was estimated by comparing samples with different porosity but the same lithology (silty clay).

2.2.2 Resistivity Errors

The increase in pore water equivalent salinity, resulting from dewatering, led to the fairly large systematic error in resistivity measurements. The ratio between the resistivity of non-dewatered and dewatered sediment can be written as:

$$\frac{\rho_1}{\rho_2} = \frac{L_2}{L_1}, \quad (2.16)$$

where ρ_1 and ρ_2 , L_1 and L_2 are resistivity and conductivity of normal and dewatered sediments, respectively [Atkins, 1990]. Conductivity can be calculated from equivalent conductivity, which is directly related to the equivalent salinity of pore fluid:

$$L = \lambda \cdot C / 10^{-3}, \quad (2.17)$$

where λ and C are equivalent conductivity and equivalent concentration. The unit of λ is $\text{ohm}^{-1}\text{m}^2$. The relationship between λ and C is:

$$\lambda = \lambda_0(1 - \beta\sqrt{C}), \quad (2.18)$$

where λ_0 is the limit equivalent conductivity and β is a factor which is a constant for a given pair of solvent and solute. For a NaCl solution, β and λ_0 are 2.68 and 0.013245, respectively. Equivalent concentration C of pore fluid can be approximately calculated with the assumption that the solute is NaCl only. The C values for non-dewatered and dewatered pore fluids are 0.6126 and 0.6968, respectively.

Putting the formulas above together, the ratio ρ_1/ρ_2 can be written as [Atkins, 1990]:

$$\frac{\rho_1}{\rho_2} = \frac{1 - \beta\sqrt{C_2}}{1 - \beta\sqrt{C_1}}, \quad (2.19)$$

The result shows that the resistivity values decreased at least 12.3%.

The formula used in calculating the equivalent conductivity is for extremely dilute NaCl solutions (<0.05 Mol/L), in which the relationship between λ and C is nearly linear. As C increases, λ_0 increases faster so that for NaCl solution such as the pore fluid, a larger decrease in resistivity values should be expected.

2.2.3 Velocity Errors

The velocity measurement gear was not able to pick the first breaks automatically with a single threshold amplitude. First arrivals were picked manually and by different operators in the two measurement stages.

The velocity values for data sets I and II showed a systematic difference in dominant values of ~3%. This may be partially due to operator difference, but the increase in velocity for data set II most likely arises from the increase in bulk density due to dewatering. Velocities for data set I were less than water velocity at the seafloor. This result may be due to a number of factors such as changes of elastic parameters due to decompaction after bringing the sediment samples up from depth and short-term resetting of sediments in the cores due to gravity and vibration from handling. To determine reliable velocities of the seafloor in this area, we suspect that measurement should be done on-board ship within a few hours of core recovery.

Without such measurements, we consider that the 3% systematic difference between data sets I and II is probably a reasonable estimate of the absolute errors in velocity measurements.

2.3 Physical Property Analyses.

Before proceeding to physical property analyses, the following issues should be kept in mind:

1: Data set I generally was of high quality and was measured within 1-2 months of sediment collection. Data set II was measured about 6 months later than data set I. Data set II was subjected to long-term dewatering and hence the empirical relationships between these physical properties interpolated from data set II may be subject to error, though they were still quite consistent if only relative values in data set II were examined.

2: Values from seriously cracked clayey silt and silty clay or values from extremely liquified thick fine sand layers were not used in the analyses.

2.3.1 Index Physical Property Variation with Depth

Index properties include bulk density, porosity, water content (as percentage of dry and total mass), grain density, and dry density. Their variation with depth was compared with the topmost part of core data at ODP Site 889/890.

Figure 2.5 and 2.6 show the index property variations with depth from data set I, II and ODP Sites 889/890. ODP Site 889/890 was about 1 km east of Area 2, surrounded by the PGC96004 coring sites 11, 12, 13, 14, 15&19 (figure 1.6). Core 13 was very close to ODP Site 889A and core 12 was located 1.2 km east of the site.

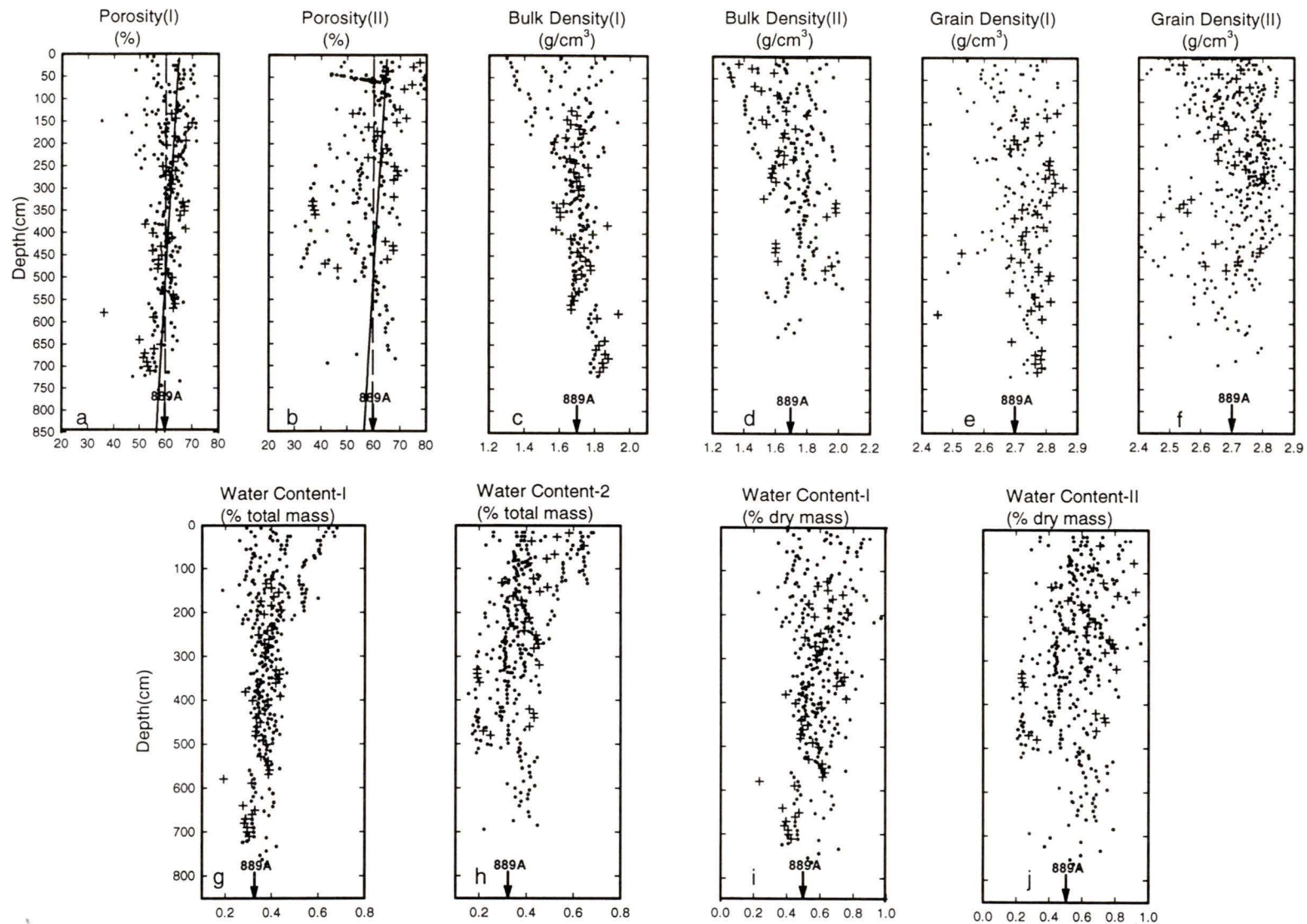


Figure 2.5 Index physical properties variation with depth in data sets I and II. Solid lines in (a) and (b) are least-square optimum Athy's Law for the topmost seafloor sediments and dashed lines are for deeper accretionary wedge sediments. Physical properties for core 12 and 13, which were the closest cores to ODP Site 889/890, are indicated by "+" symbols.

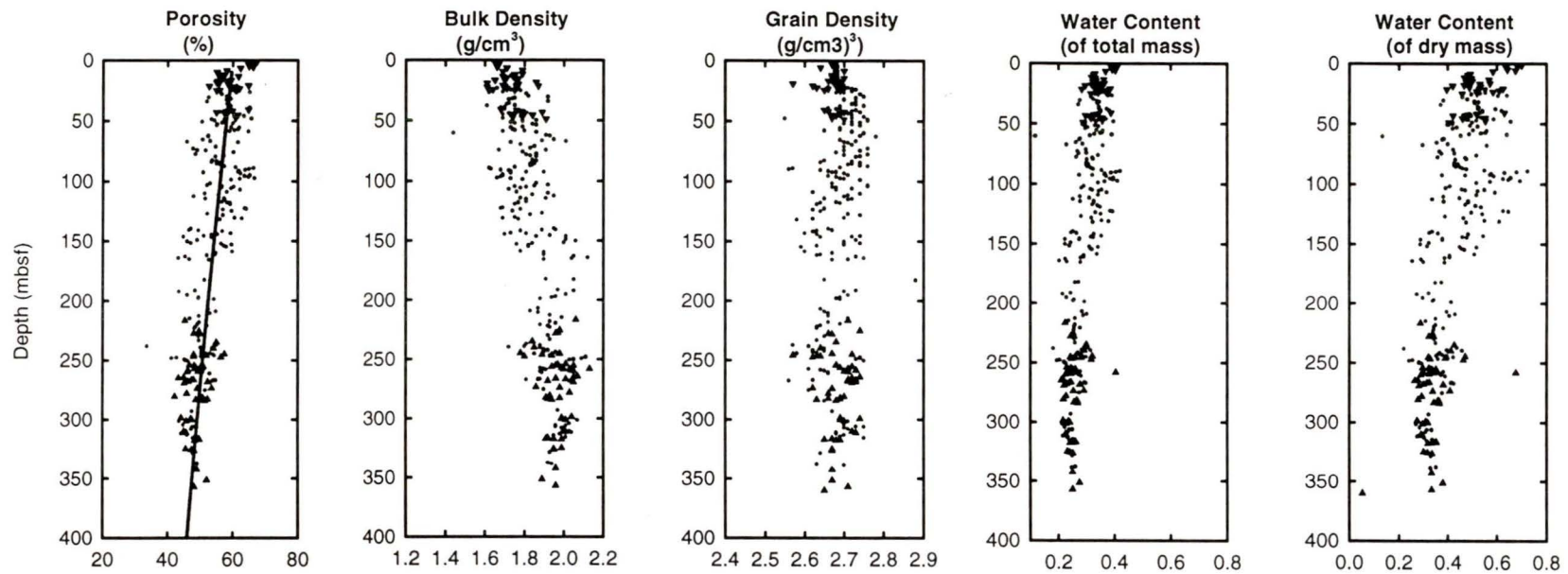


Figure 2.6 Index physical properties at Site 889/890. Black dots, triangle up and triangle down are Hole 889a, 889b and 890b, respectively. Solid line in (a) is the Athy's Law for deep accretionary wedge sediments with a surface porosity of 60% and an exponential decay constant of 1.5 km [Davis, et al, 1990].

Cores from hole 889A, hole 889B and hole 890B were recovered over the interval from 20.0 mbsf to 346 mbsf, 206.4 mbsf to 386.5 mbsf and seafloor to 47.8 mbsf, respectively. Index properties of cores 12 and 13 were directly comparable with core 1H of hole 890B, which spanned the interval from 0.0 mbsf to 7.3 mbsf. However, core 1H at Hole 890B was not perfectly recovered and index properties were measured at an interval of more than 1 m. The measurement spacing on cores from survey PGC96004 was generally 10 cm and sediment samples were seldom missing so that the results, especially those from cores 12 and 13, provided higher resolution information relative to ODP Sites 889/890. In figure 2.5, physical properties for cores 12 and 13 are indicated by a separate symbol.

I. Porosity, Bulk Density and Grain Density.

In a gas-free sediment sample, the volume of voids occupied by pore fluid is expressed as porosity (void volume/sample volume). The porosity of unconsolidated silty clay on continental shelves and slopes normally varies from 38% to 73% [Hamilton et al., 1982]. The porosity values in data set I (figure 2.5a) ranged from 35% to 72%, which is very consistent with the data set compiled by Hamilton. Porosity in data set II varied over a larger range from 30% to 84% with lower porosity in the deeper part of a section and higher porosity in the shallower part, relative to the earlier measurement. Since individual core sections were stored vertically, upward pore fluid migration resulted in a dry lower part and a wet upper part. Hence the values from the early measurement run were considered more reliable than the later run in terms of variation of absolute values versus depth. However, provided that the salinity of pore fluid remains constant in the core sections, the two sets of

measurement were treated equally when empirical relations between the physical properties were examined.

The variation of porosity P versus depth Z follows an approximate exponential function, known as Athy's Law:

$$\phi = \phi_0 e^{-Z/L}, \quad (2.20)$$

where ϕ_0 is the surface sediment porosity and L is the characteristic decay length.

Seismic velocity and thermal conductivity data are also consistent with this law since both primarily depend on porosity. In the Cascadia Basin, the regional trend for the upper 2.7 kilometers of sediments corresponds to a surface porosity of 60% and exponential decay constant of 1.5 km [Davis et al., 1990]. At Site 889, there are three sets of parameters used in fitting the porosity profile for the upper 400 m of sediments, as listed in table 2.2 [Westbrook et al., 1994].

Unit	Range(mbsf)	ϕ_0 (%)	L(km)
Unit I	0.0~128.0	58.7	4.0
Unit II	128.0~300.0	57.0	1.785
Unit III	>300.0	25.1	5.0

Table 2.2 Three sets of parameters used in fitting the porosity-depth function at Site 889/890.

Neither the parameter used for the regional deeper sediment or those from ODP Sites 889/890 satisfactorily fit the topmost sediment data in the same region or the same location so that a new value for the surface porosity and decay constant were employed. A surface porosity of 65% and a decay constant of 60 m were used to fit the porosity variation in data set I (figure 2.5a). Because the surface sediment porosity used for the deeper trend is 60%, the measured near-surface porosity values are greater than the inferred regional values for the upper 5.5 m of the sediments,

corresponding to the intersection of the shallow trend and the deeper trend. This leads to the conclusion that shallow seafloor sediments are subjected to a different more rapid compaction process than the deeper sediment.

Bulk density varied significantly in the topmost 2 m of sediment, ranging from 1300 kg/m^3 for soft mud (silty clay) to 1800 kg/m^3 for fine and very fine sand (figure 2.5 c,d) . In data set I, the bulk density converged to 1650 kg/m^3 below a depth of 2 m, where clayey silt and silty-clay were the dominant lithology. This result is quite consistent with that from ODP site 889A (figure 2.6 b) in which the surface bulk densities were 1670 kg/m^3 to 1750 kg/m^3 .

Grain density for both data sets I and II varied over the range from 2600 kg/m^3 to 2800 kg/m^3 (figure 2.5 e-f). Typical values were 2700 kg/m^3 , which is consistent with the average value at Sites 889/890.

II. Water Content

Water content (as percentage of either dry mass or total mass) of data set I (figure 2.5g, i) was also consistent with that of ODP site 889 data (figure 2.6d, e). Below 2 mbsf, water content in terms of total mass and dry mass in data set I converged to 35% and 55%, respectively. Water content in data set II showed a more dispersed pattern due to non-uniform dewatering process.

2.3.2 Velocity

The velocity of the topmost sediments is important when studying reflection and refraction of sound waves incident on the sea floor. In the deep sedimentary basin where seafloor is mainly covered by soft mud, velocities can be equal to or slightly lower than that of seawater [Hamilton, 1982]. On continental shelves and slopes,

seafloor velocities are generally slightly higher than that of seawater except for a soft mud layer at the very surface that has a lower velocity.

The measured sediment velocities averaged 1450m/s and 1500m/s for data set I and II, respectively (figure 2.7). It is clear that seafloor sediment velocities are very close to the seawater velocity, and that reflection coefficients at the seafloor must be mainly dependent on contrasts in bulk density.

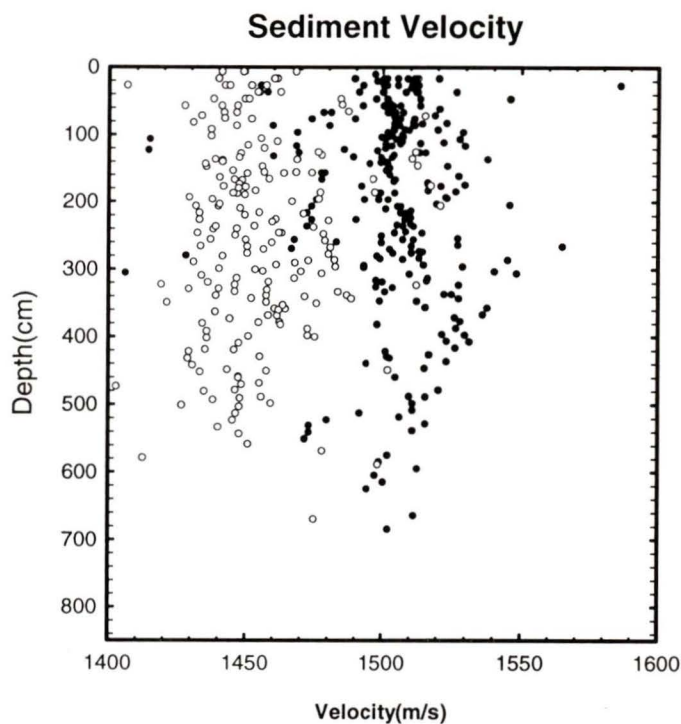


Figure 2.7 Sediment compressional wave velocity versus depth. Open circles and black dots are velocities from data set I and data set II, respectively.

2.3.3 Prediction of Porosity from Resistivity

Archie's Law gives the empirical relationship between sediment resistivity (or formation factor) and porosity. It can be written as:

$$R_{sample} = R_{porefluid} \alpha \phi^{-m}, \quad (2.21)$$

or:

$$FF = \alpha \phi^{-m}, \quad (2.22)$$

where α and m are tortuosity and cementation coefficients. For ODP Site 889/890 data, porosity spanned a large range from 40% to 72%, and the best-fit parameters were $\alpha=2.07$, $m=1.76$, with a correlation coefficient of 0.7 [Westbrook, 1994]. However, after correction to the pore fluid salinity, the Archie's Law parameters for Site 889/890 were very close to those derived for ODP Site 888, namely $\alpha=1.41$ and $m=1.76$ (figure 2.8).

Archie's Law parameters for data sets I and II were derived in a least-square sense. The best fit parameters were determined by performing a linear correlation of $\text{Log}FF$ vs. ϕ . The correlation factors were 0.78 for data set I and 0.85 for data set II. The optimum Archie's Law parameter was $\alpha=1.40$, $m=1.84$ for data set I and $\alpha=1.10$, $m=1.84$ for data set II (figure 2.8). The systematic difference between data sets I and II was mainly caused by the loss of about 11.8% pore fluid in data set II. For absolute measurement of resistivity or formation factor, we thus consider data set I to be more representative of the true values.

Given the optimum parameters for Archie's Law, porosity may be predicted from measurements of resistivity alone. The measured and predicted porosity from both the earlier and later measurements demonstrates excellent correlation (figure 2.9). Correlation factors of 0.90 or greater were achieved for 9 of the 18 cores.

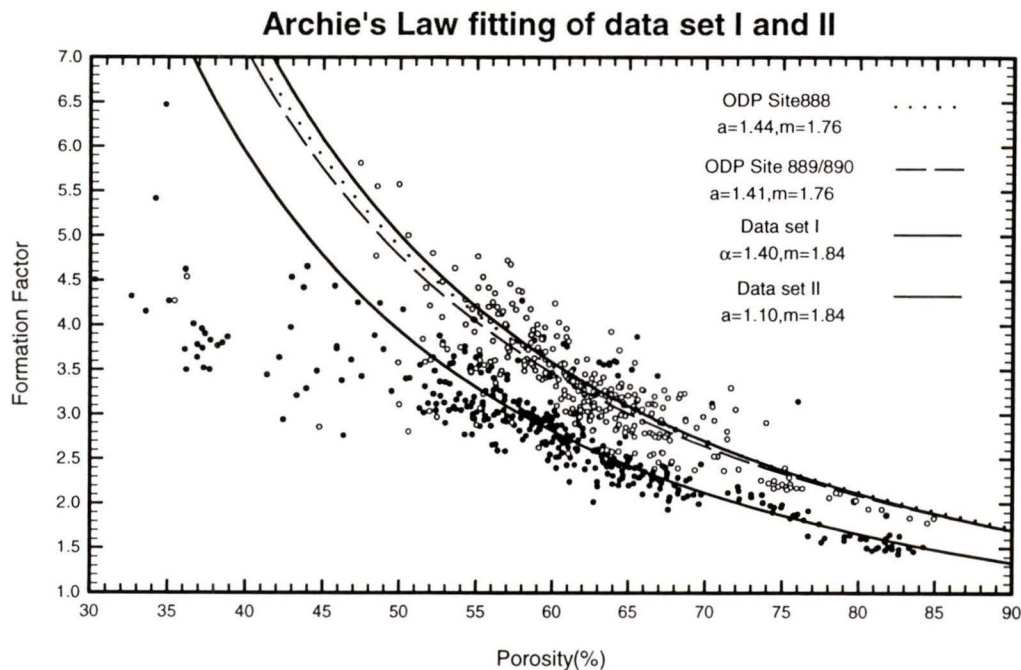


Figure 2.8 Formation factor vs. sediment porosity for data set I and II. Open circles and black dots are data set I and II, respectively. Temperature correction was applied. Data set II is consistent with Archie's Law for ODP Sites 888, Sites 889/890.

2.4 Suggestions for improvement in Methodology of Physical Property Measurement

Based on the error analyses of physical property measurements, the following recommendations are made for possible improvements in future lab work.

1: Measurements should be done as soon as possible. If possible, on-board work should be done at least to a subset of the cores to provide reasonable constraints on data from laboratory measurement. Though data set I was measured about one month after coring, some dewatering may have occurred, but much less severe than that for data set II.

2: Core cracking was one of the major sources of error in velocity measurement and a minor one in other property measurements. Vibration during core splitting operation caused part of the cracks. Better core splitting tools are required.

3: Automatic first-break picking equipment is highly recommended if more than one person is involved in the measurement.

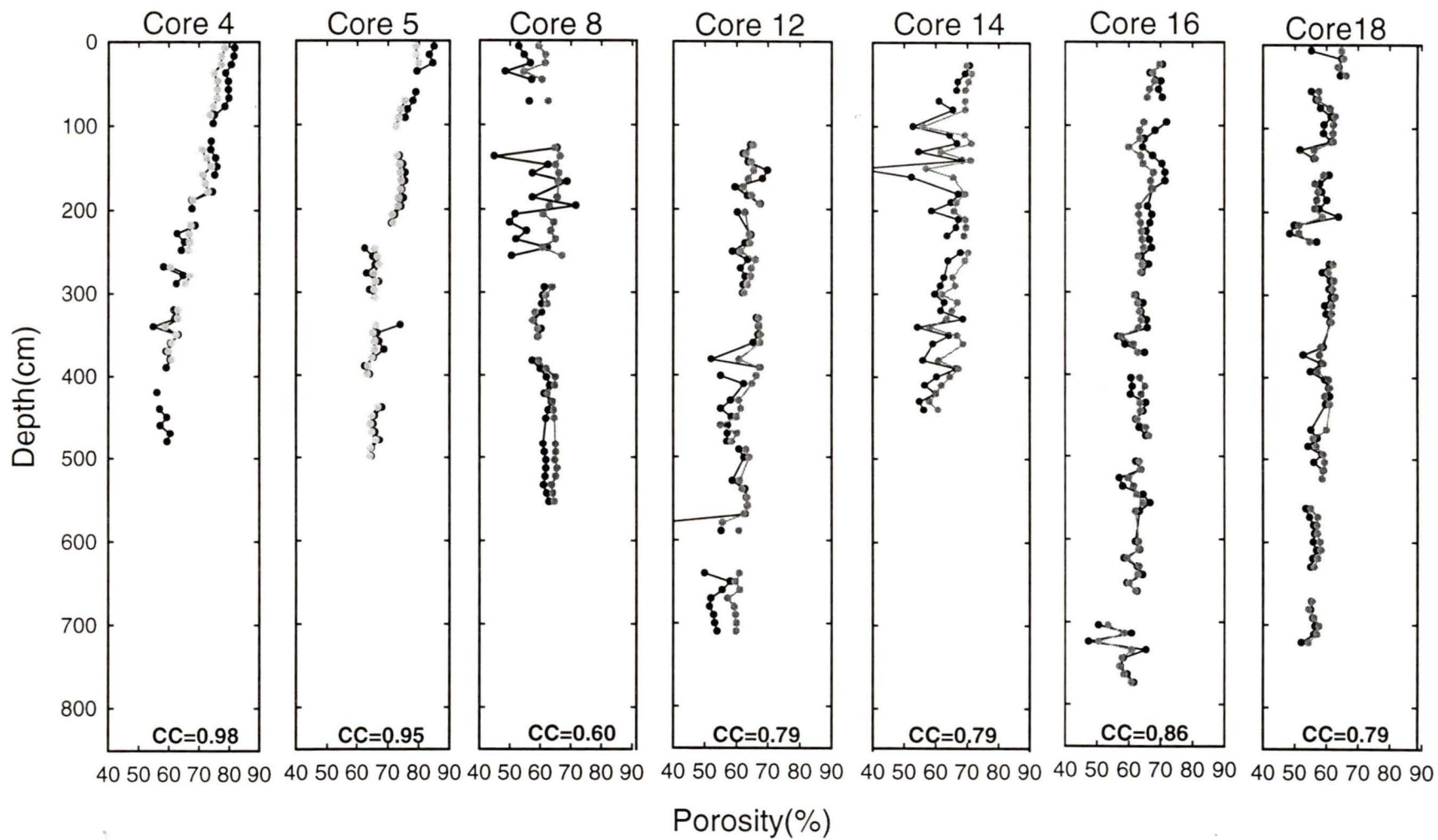


Figure 2.9 a Porosity prediction from Archie's Law (data set I). Black and gray dots are measured and predicted porosity. Same symbols are used in figure 2.9 b and c. 14

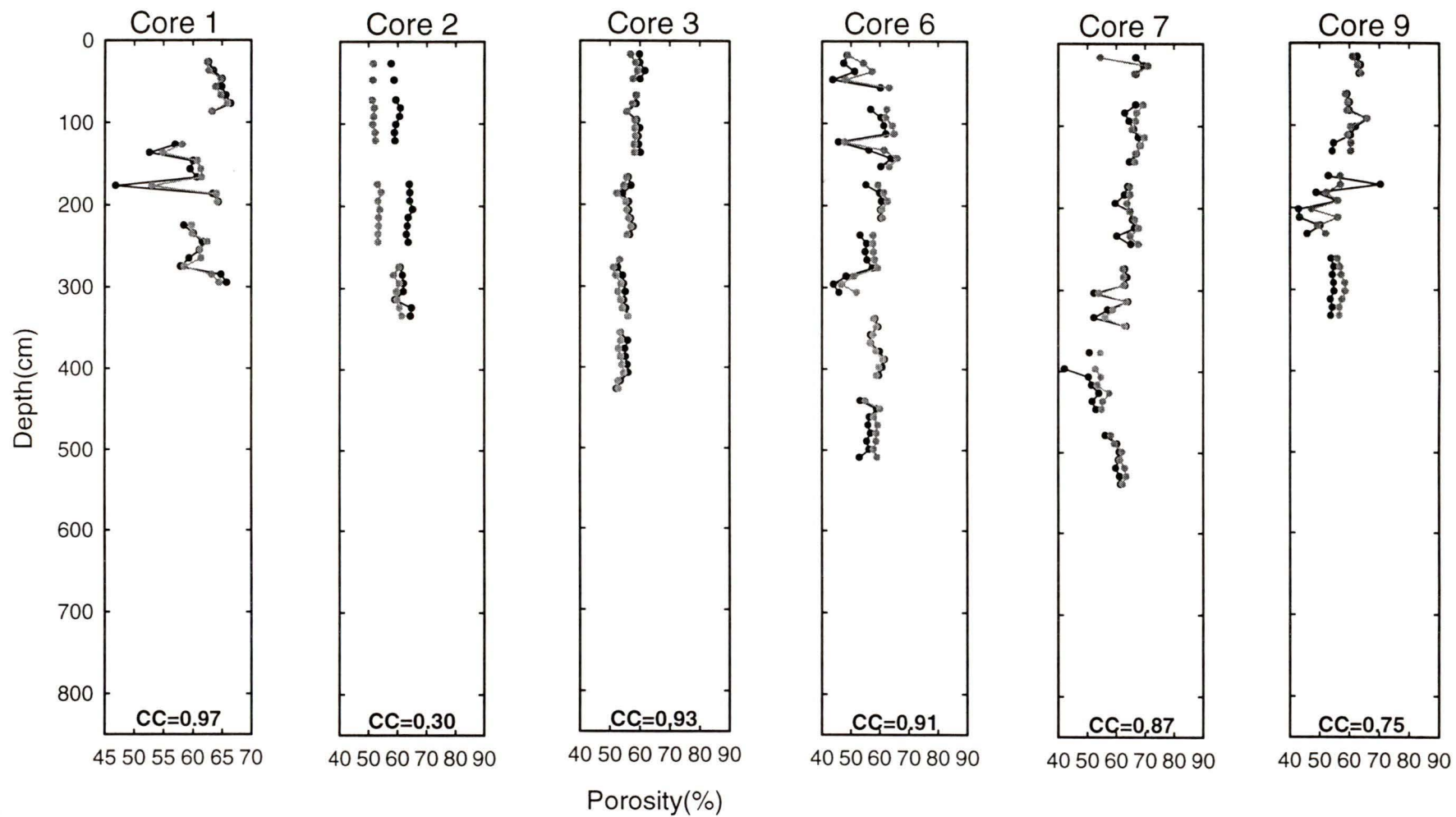


Figure 2.9 b Porosity prediction from Archie's Law (data set II).

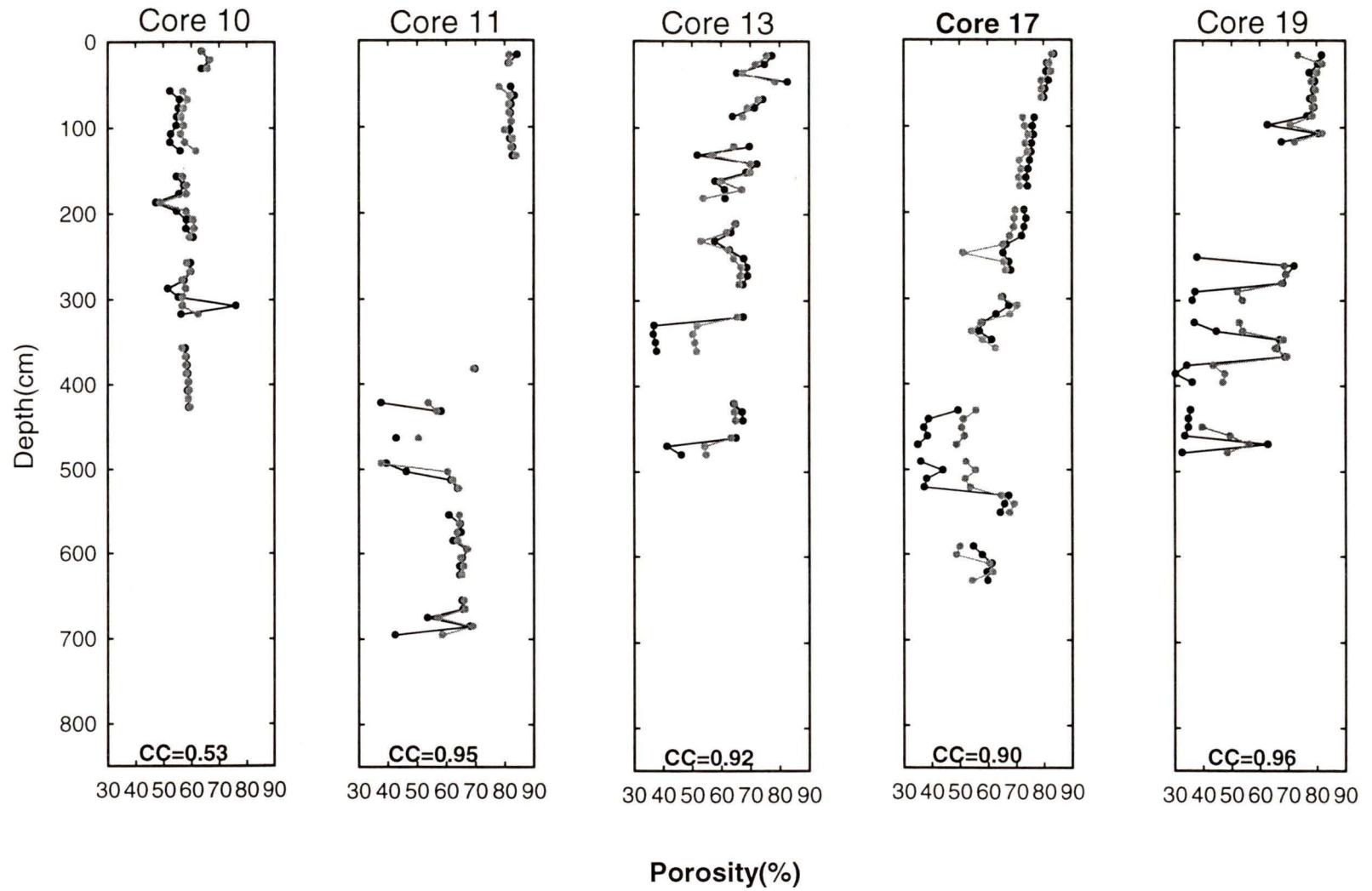


Figure 2.9 c Porosity prediction from Archie's Law(data set II).

Chapter 3. Seafloor and BSR Reflection Coefficient Study

3.1 Data Acquisition

In Survey PGC96004, the seismic source used was a 120 cubic inch (2.0 L) Bolt 1500C airgun. Compressed air, at a normal pressure of 1800 PSI, was supplied from a large capacity Sulzer compressor (120 cu.ft. per minute) provided by the Pacific Geoscience Centre. The airgun was triggered by the navigation system which maintained a constant shot interval of 24 m. This corresponded to a firing rate of approximately 6 shots per minute, assuming a ship's speed of 4.8 knots. The airgun was at an estimated depth of 4 m and the estimated gun position was about 10 m behind the ship.

The receiver array was a 24-channel ITC streamer, with a group interval of 8 m and offsets from 106 m to 290 m. Each group of receivers consisted of three hydrophones separated by 1 m. Data were acquired through a Geometrics Strataview 24-channel digital system. The sample rate was 2 ms and the record length was 4096 ms with a deep-water delay of 500 ms.

The on board differential GPS (DGPS) output was utilized by the navigation system. The estimated absolute precision of DGPS was about 5 m. Bathymetry data were picked automatically at an interval of 5 s from a 12 kHz transceiver, using the sea water velocity depth profile in this survey region. Both time and location in longitude/latitude were recorded.

3.2 Seismic Data Processing.

3.2.1 Data Processing Flow.

Data processing was carried out using ITA511 seismic data processing package of LANDMARK Graphics. The major steps in the processing flow are shown in table 3.1.

Steps	Description
1. Data Format Conversion.	SEG2 to SEGY.
2. Data Format Conversion.	SEGY to ITA.
3.Header Manipulation.	Geometry related header words manipulation.
4.CMP Sorting.	Four-fold CMP gathers.
5.Super CMP Sorting.	Six adjacent CMP gather were grouped and traces were sorted according to offsets, 24 traces per gather.
6.Bandpass Filtering.	10 – 25 – 90 – 110 Hz
7.Predictive Deconvolution.	Operator length: 256ms, Predictive distance: 16ms.
8.Spherical divergence correction.	Proportional to travel time.
9.Velocity Analyses.	At each 20 super CMP gathers.
10.NMO corrections.	Velocity from velocity analyses were used.
11.Stacking.	Super CDP stacking.
12. Kirchhoff migration.	Velocity grid was used.

Table 3.1 Seismic data processing flow.

The raw survey data in SEG2 format were converted to SEGY format before importing to ITA. The survey geometry only resulted in a 4-fold CMP gather. To enhance the accuracy of velocity analyses, six adjacent CMP gathers were grouped to give a 24-channel super CMP gather. The bin width for a super CMP gather was 24 m. In regions where the seafloor has a very steep slope (15 degrees), the near and far offset travel times varied over a rather large range. For a constant water depth of 1300 m, the normal moveout difference between the near offset of 106 m to the far offset of 290 m was 11 ms. The difference increased to about 40 ms for downdip shooting and

–24 ms for updip shooting. As a result, the reflection of seafloor as well as other reflectors below the seafloor was not well defined in these slope areas on either stacked sections or migrated sections.

The predictive deconvolution was aimed at removing the bubble pulse which reverberated at a period of 100 ms for the 120 cu. in airgun. Peg leg multiples were also attenuated. A spherical divergence correction, which was proportional to travel time, was applied for amplitude recovery. Velocity analyses were used only for stacking purposes and could not be used for actual velocity estimations because of the small shot-receiver offsets. Kirchhoff migration generated rather good subsurface images over the flat portions of the lines.

Several typical seismic lines in Area 2 are displayed in figure 3.1. A portion of Line89-08 overlapping line 12 is also shown for comparison. Note that the BSR generally was not present in the small slope basins over the shallow water region where sediment layers were well defined. The BSR in the deep sedimentary basin was rather clear, but its amplitude was clearly contaminated by diffractions. The zone below the BSR was normally blank because of severe deformation in the accretionary wedge sediments.

3.2.2. Offset Dependent Receiver Ghost

Destructive interference between the ghost signal reflected from the sea surface and the direct wave can cause notches in certain band of the signal spectrum. The maximum destruction band (notch in amplitude spectrum) can be estimated with:

$$f = \frac{V_w}{2D_s}, \quad (3.1)$$

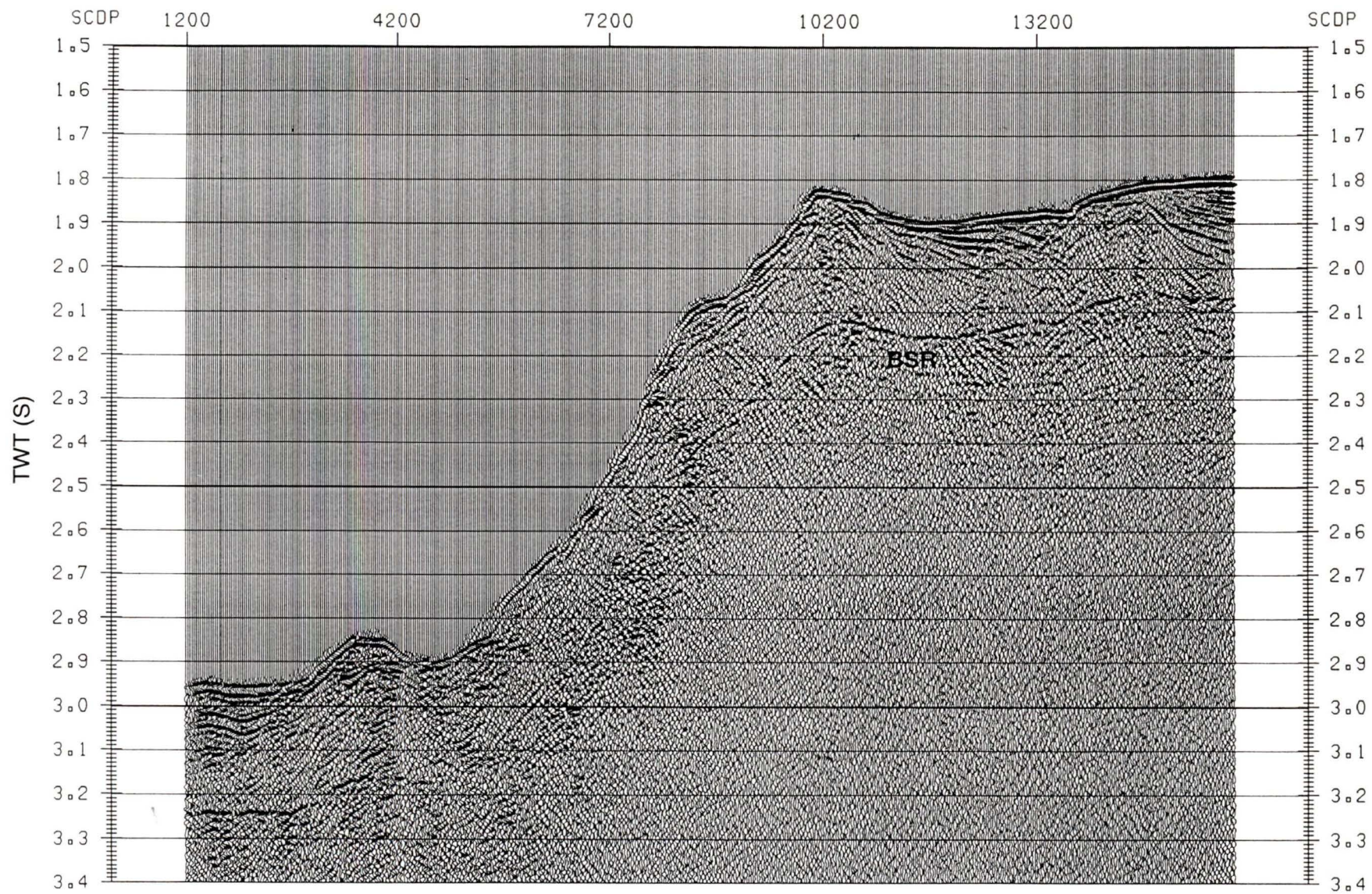


Figure 3.1 (a) Line 7 migration. Every one hundred traces (3000 SCDPs) is 2.4 km.

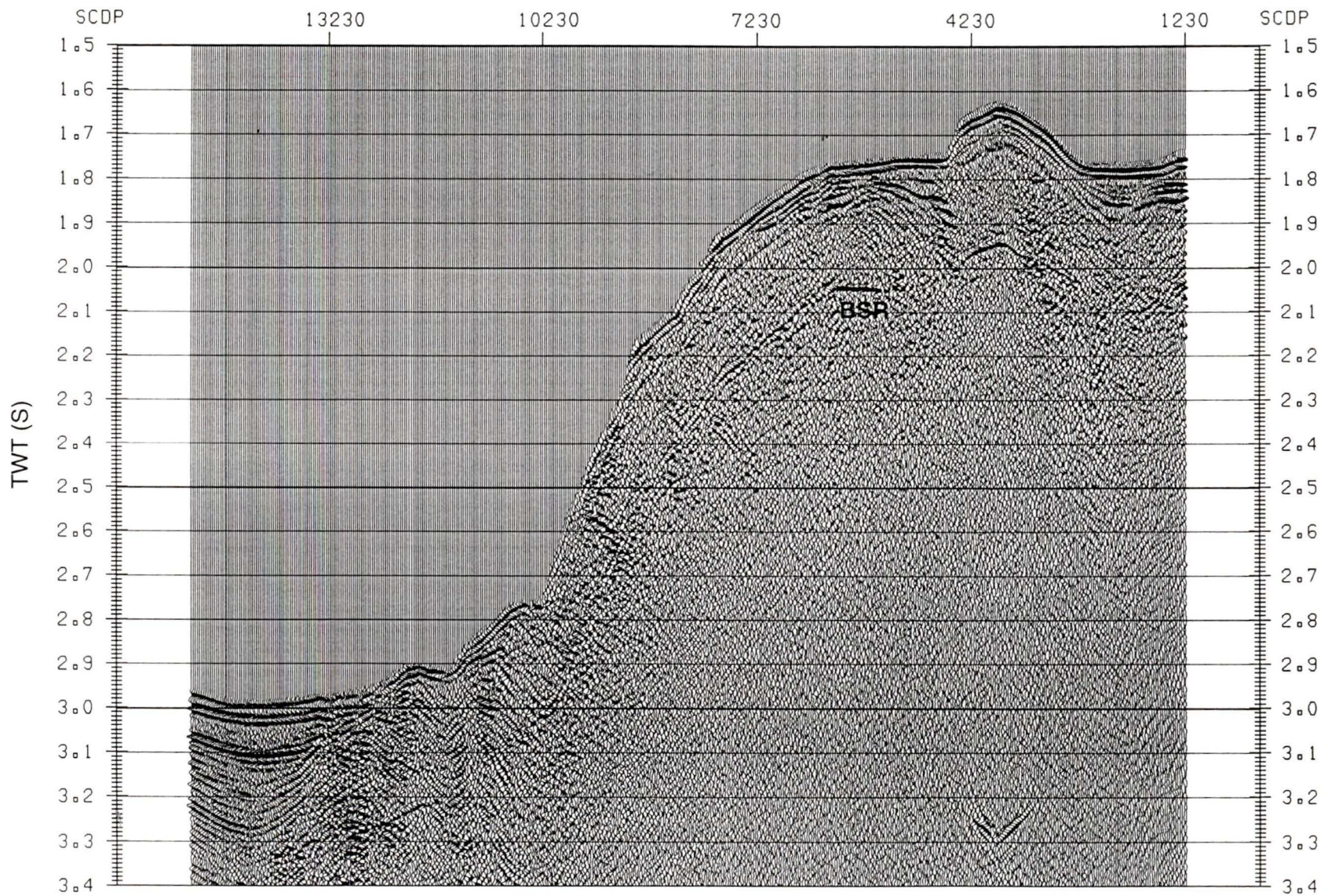


Figure 3.1 (b) Line 12 migration. Every one hundred traces (3000 SCDPs) is 2.4 km.

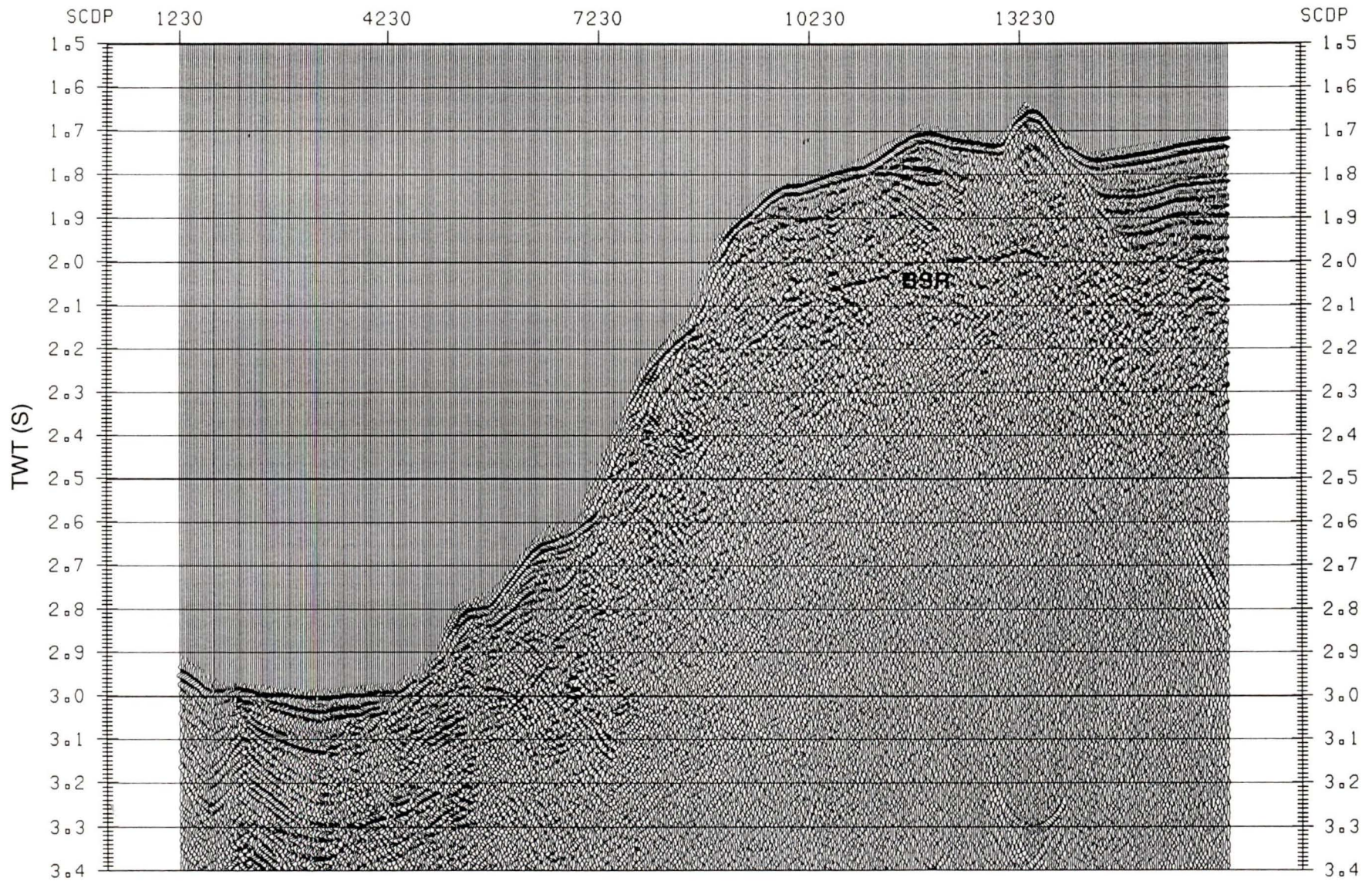


Figure 3.1 (c) Line 17 migration. Every one hundred traces (3000 SCDPs) is 2.4 km.

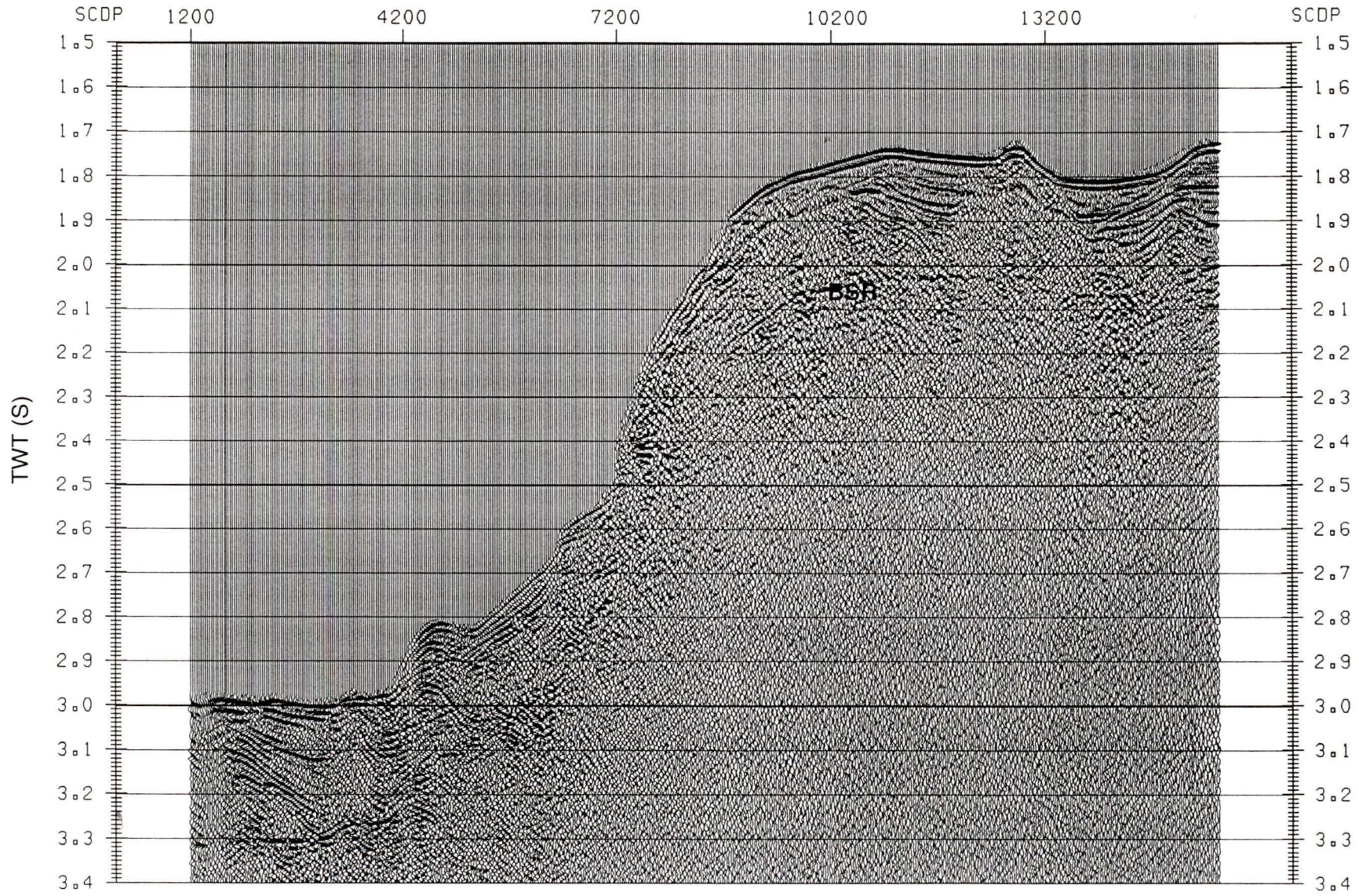


Figure 3.1 (d) Line 19 migration. Every one hundred traces (3000 SCDPs) is 2.4 km.

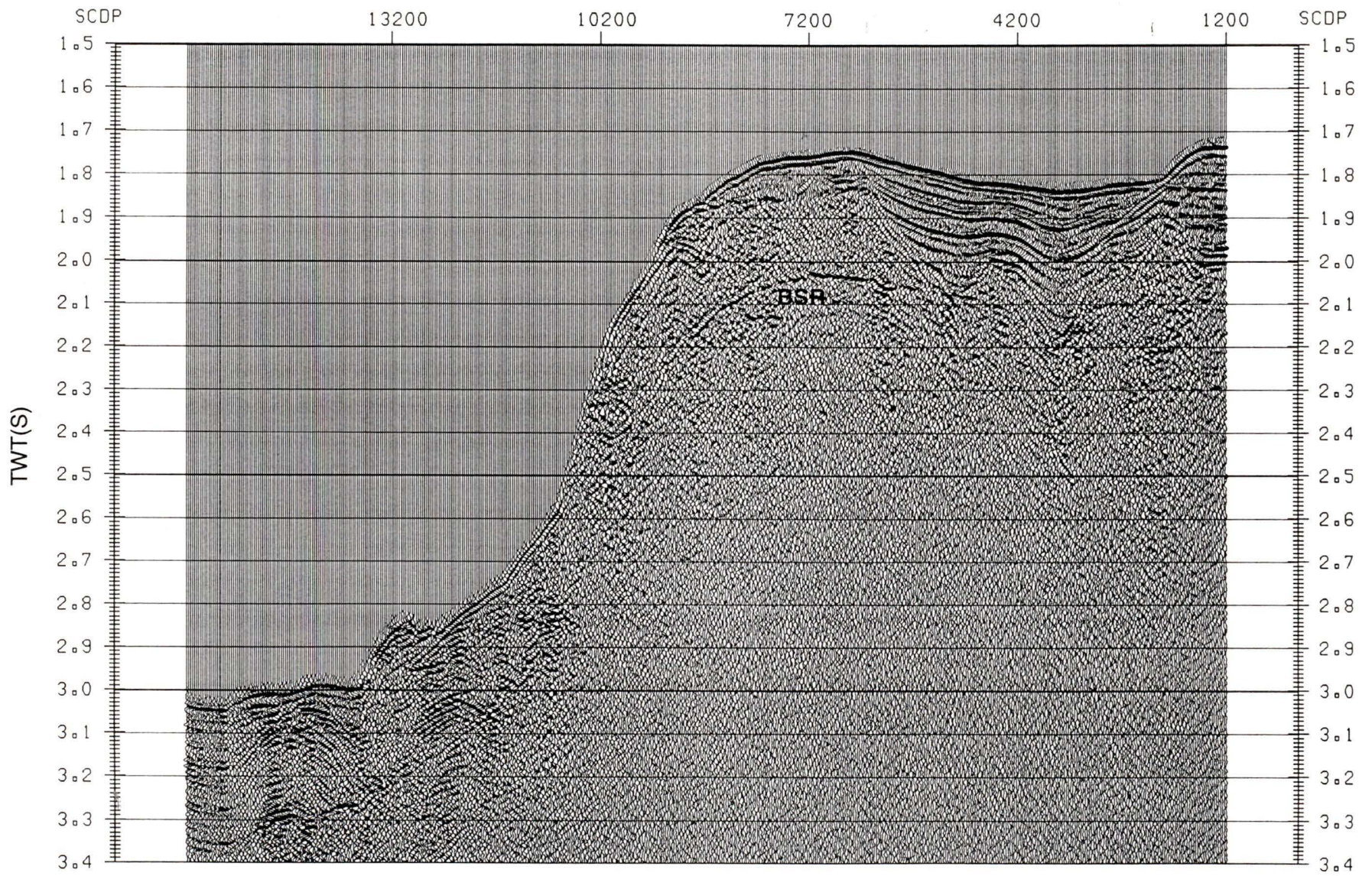


Figure 3.1 (e) Line 22 migration. Every one hundred traces (3000 SCDPs) is 2.4 km.

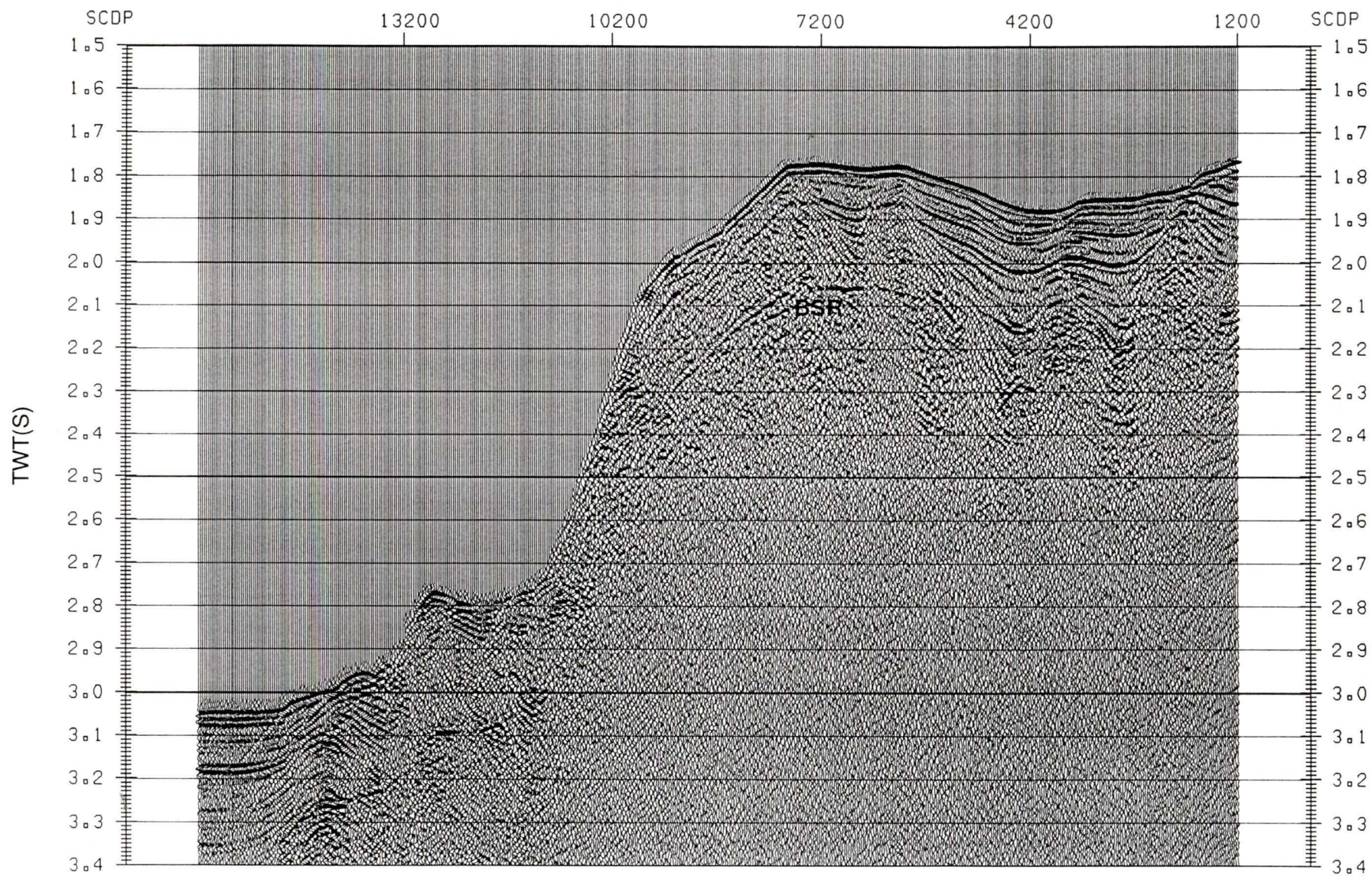


Figure 3.1 (f) Line 24 migration. Every one hundred traces (3000 SCDPs) is 2.4 km.

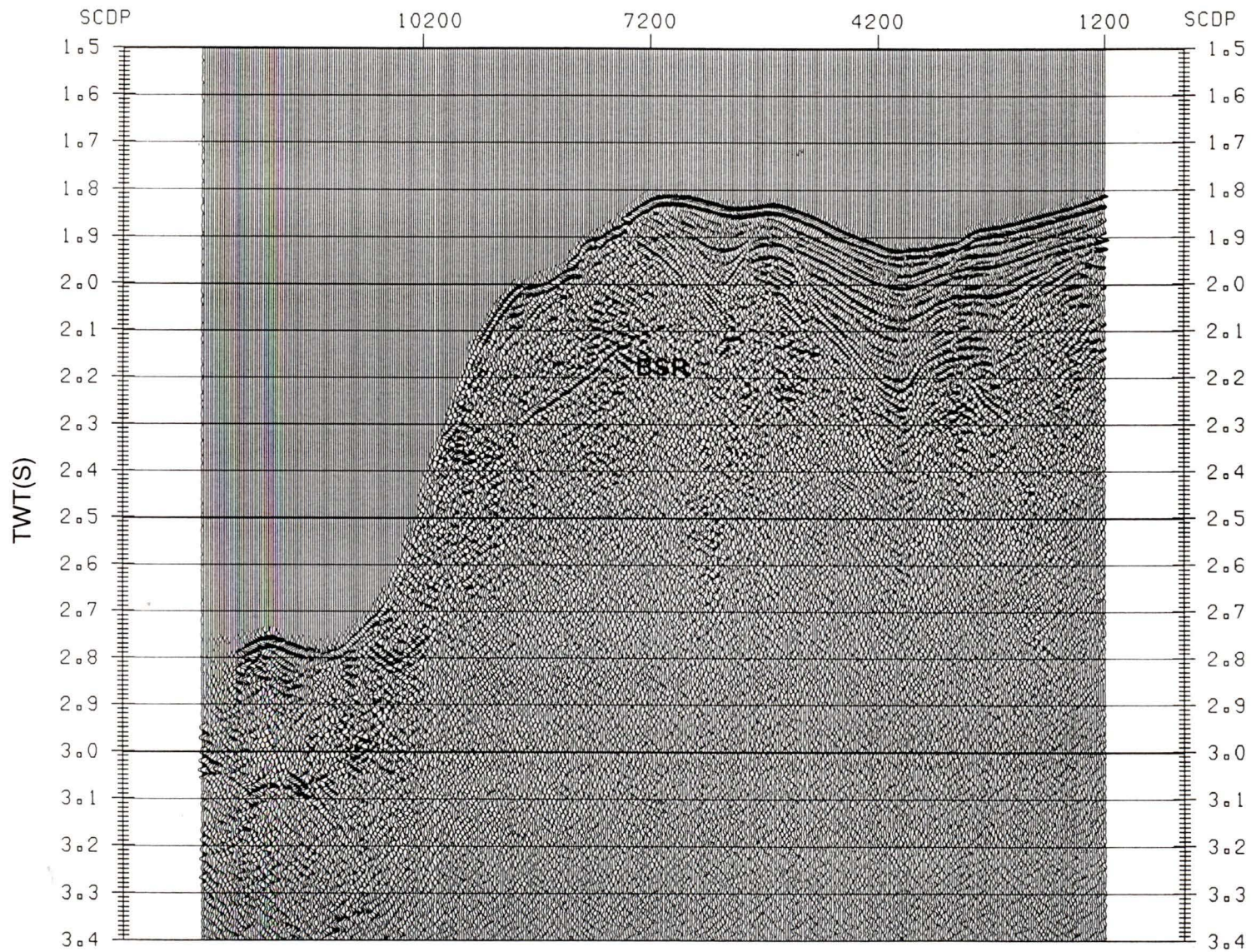


Figure 3.1 (g) Line 26 migration. Every one hundred traces (3000 SCDPs) is 2.4 km.

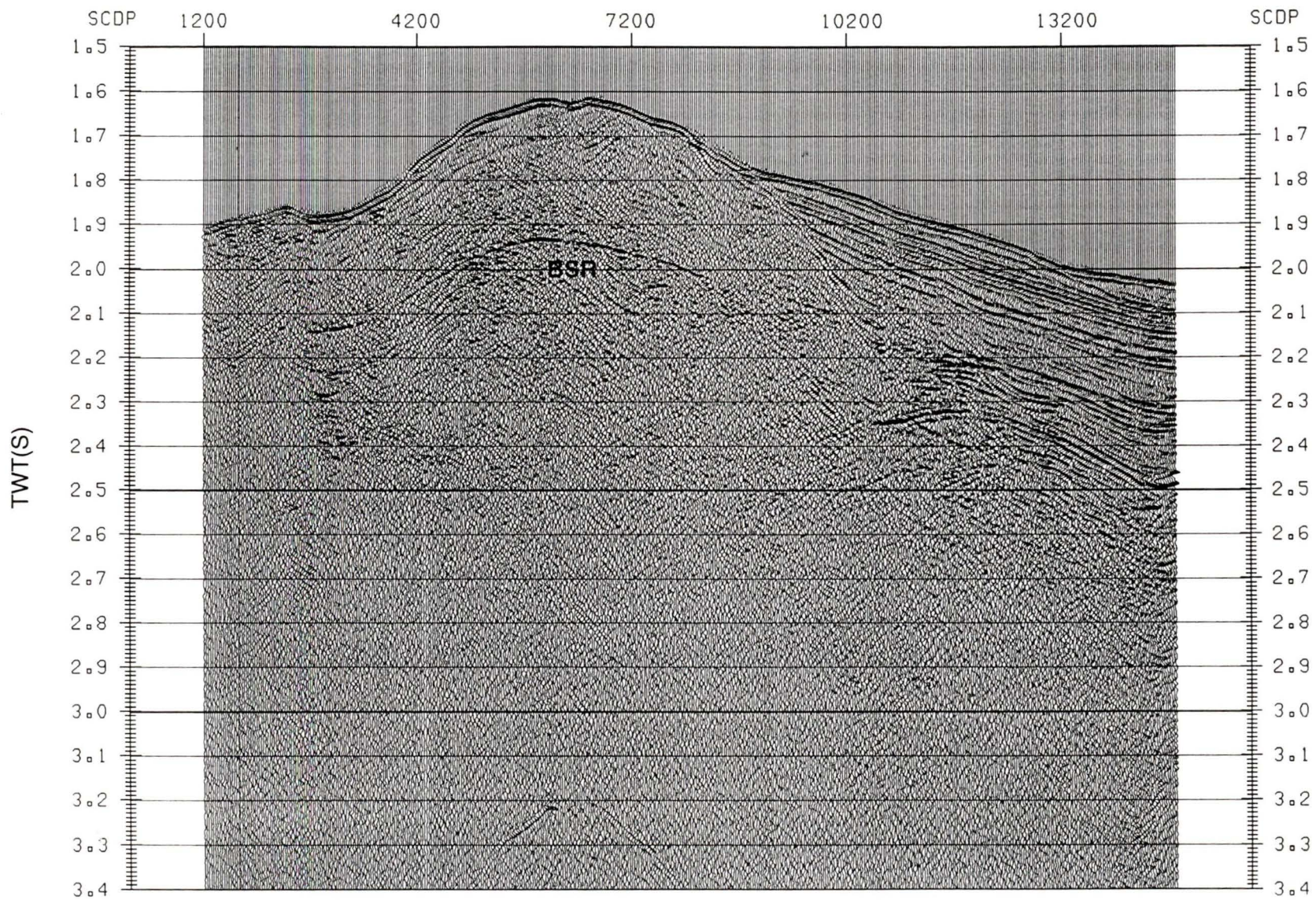


Figure 3.1 (h) Line 32 migration. Every one hundred traces (3000 SCDPs) is 2.4 km.

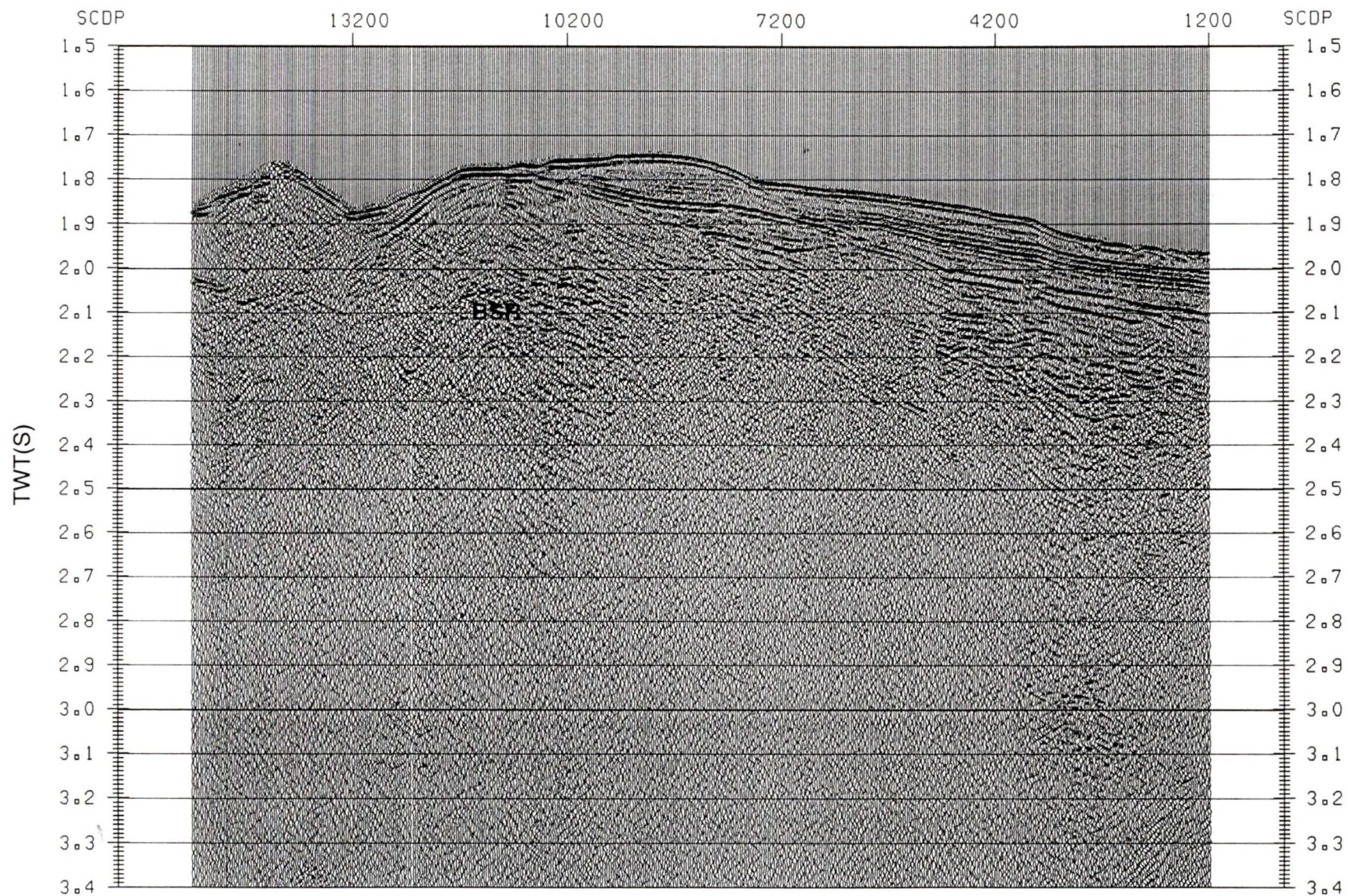


Figure 3.1 (i) Line 33 migration. Every one hundred traces (3000 SCDPs) is 2.4 km.

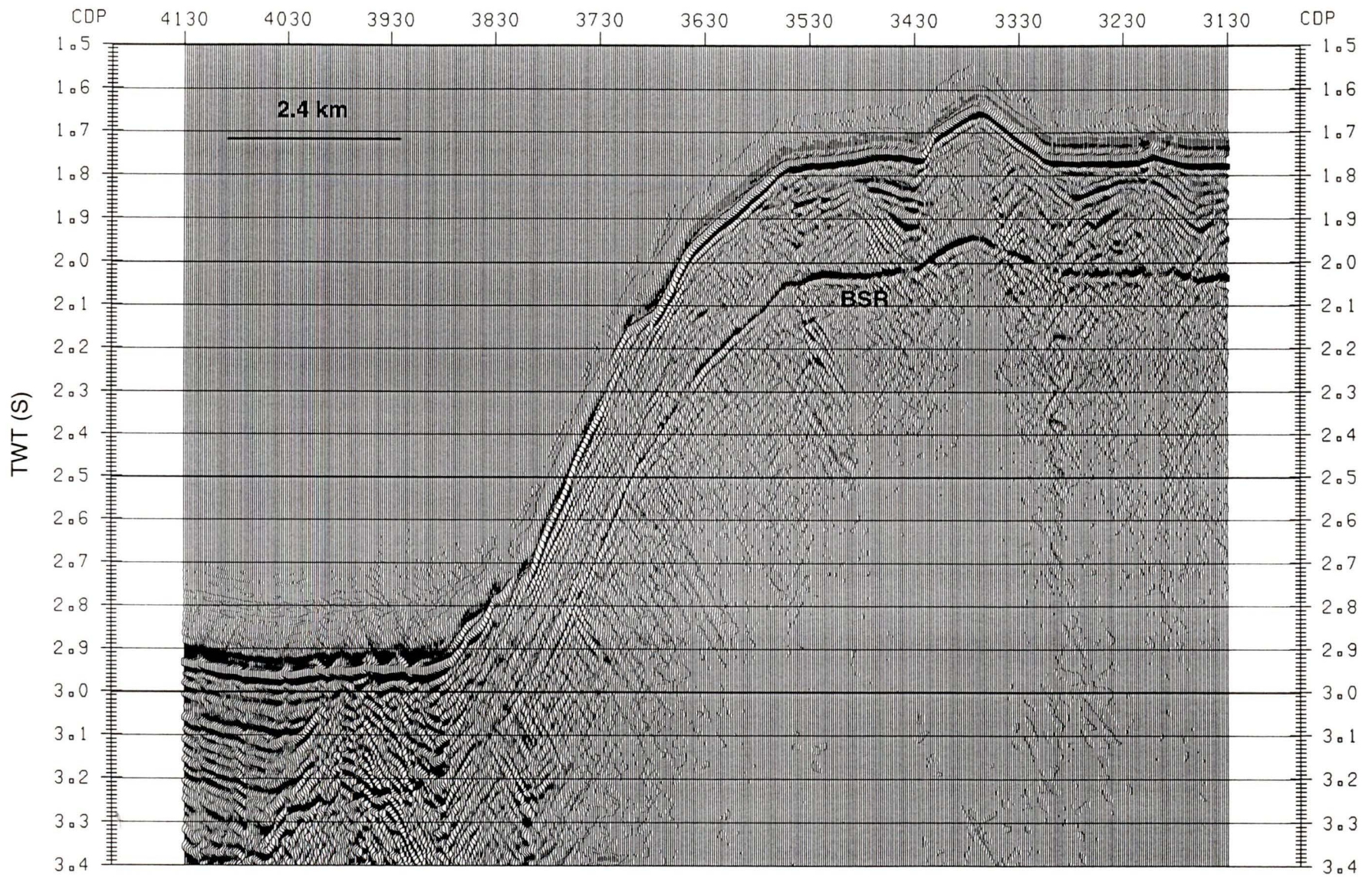


Figure 3.1 (j) A portion of the migrated section for Line 8908, overlapping Line 12 in Area2 (modified from Yuan, 1996).

where D_s is the depth of receivers and V_w is the sea water velocity.

Due to the variation of receiver depth, the notch frequency varied from 100 Hz to 75 Hz from near offset to far offset (figure 3.2 b). This result indicated an increasing receiver depth from about 7.5 m at near offset to 10 m at the far offset. By comparison, the estimated shot depth of 4 m corresponded to a notch frequency of more than 175 Hz. The predictive deconvolution was very successful in removing the ghost and flattening the amplitude spectrum. A prediction distance of 16 ms would not affect the near offset but might affect the far offset ghost (figure 3.2 a). The stacking process tended to enhance the primary reflection and to smear the ghost reflection, thus reducing its relative amplitude. However, this also had the effect of reducing the bandwidth of the stack section to less than 75 Hz (figure 3.2 b).

3.3 Seafloor and BSR Amplitude Picking

Event horizons for the seafloor, BSR and seafloor water bottom multiple (WBM) were picked interactively from the stack sections. The WBM was only recorded for water depth less than 1500 m or 2.0 s two-way-time (TWT). Amplitude picking was done by selecting the maximum positive amplitude for the seafloor and the maximum negative amplitude for BSR and seafloor WBM over time windows of 60 ms and 30 ms, respectively. The time windows were centred at the time of the picked horizons. The seafloor reflection had good quality and amplitude picking was done for nearly all of the sections (figure 3.3 a), except for part of the slope region. BSR amplitude picking was difficult in regions where strong sediment reflections were present, mostly in the deep sedimentary basin and the local small basins over the

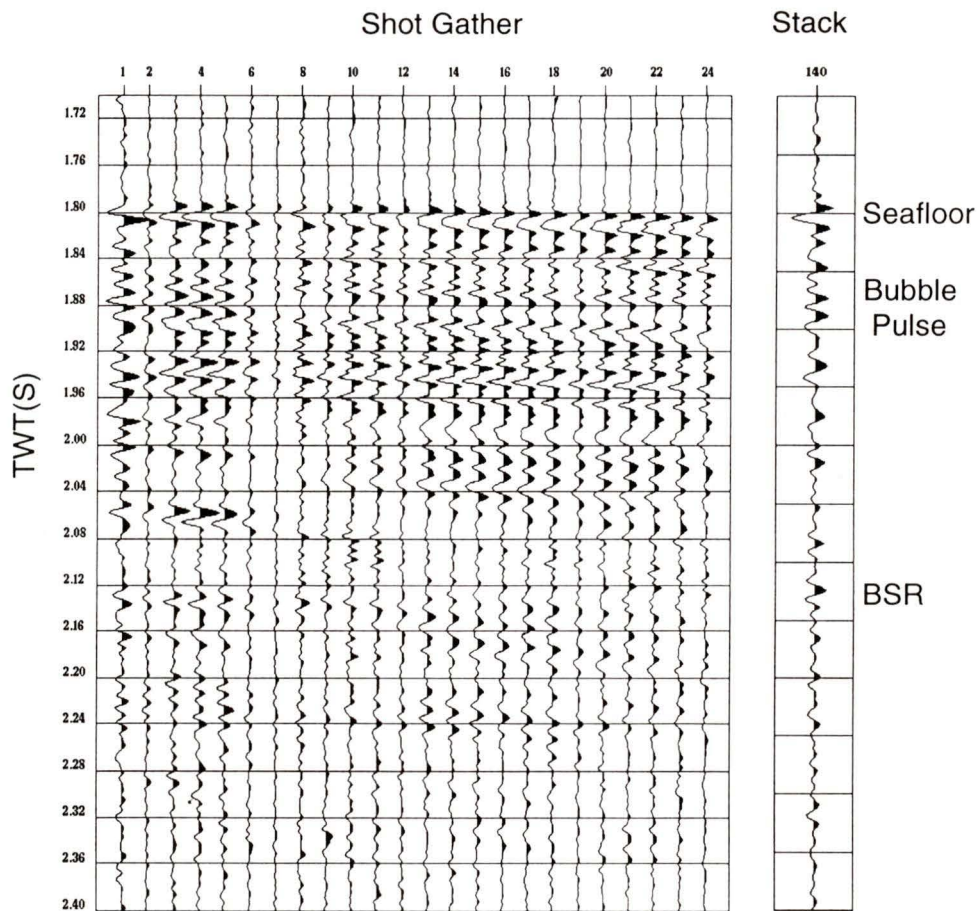


Figure 3.2 (a) A shot gather and its stack trace from Line 22 in Area 2, with bandpass filter 5-15-130-150 applied. Ghostwave caused serious destruction effect, as clearly seen at the seafloor reflection.

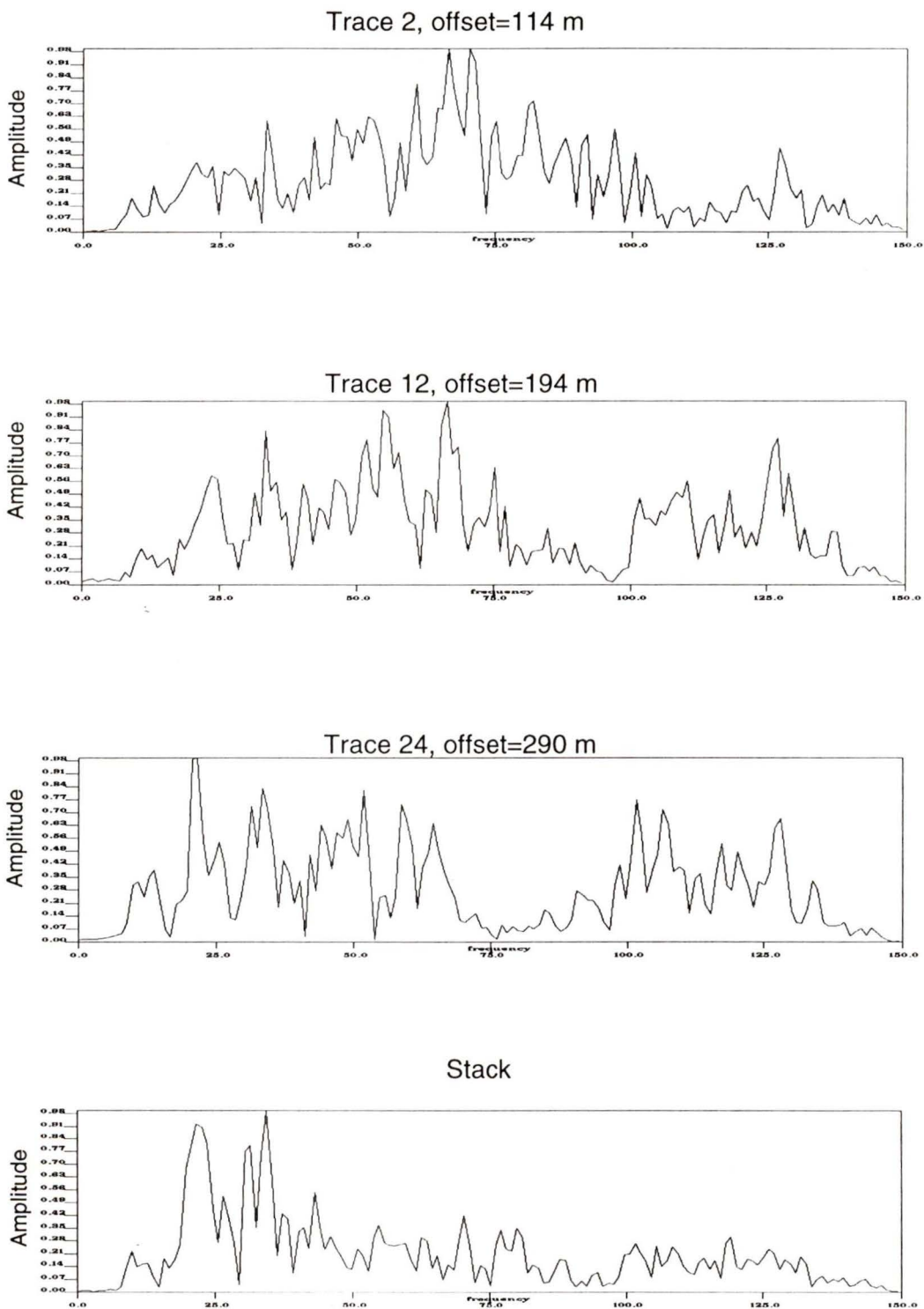


Figure 3.2 (b) Frequency spectrum for 3 traces from the shot gather in figure 3.2 (a), calculated within a time window from 1.70 s to 2.40 s. Maximum destruction band caused by the ghost wave shifts from over 100 Hz at the near offset to about 75 Hz at the far offset. After stacking, the amplitude of the band greater than 75 Hz is much weaker compared with that of lower band.

shallower water region of the survey area. At locations where very localized faults occurred, the BSR was well defined, but the amplitude was clearly contaminated by interference with diffractions. BSR amplitude picking was done only for those traces where BSR continuity was well defined and the amplitude was not contaminated (figure 3.3 b).

3.4 Calculation of Reflection Coefficients

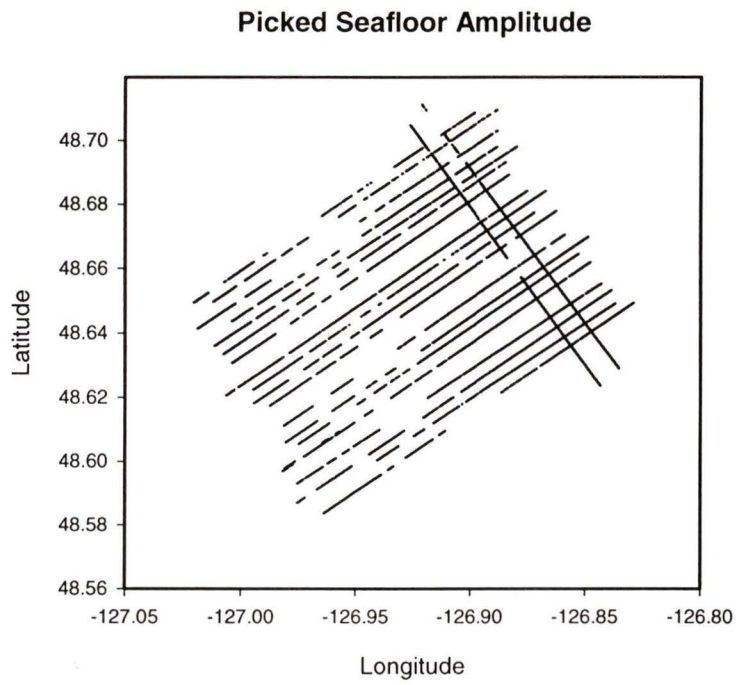
3.4.1 By Multiple/Primary Amplitude Ratio.

The seafloor reflection coefficient can be calculated with [Warner, 1990; White, 1977]:

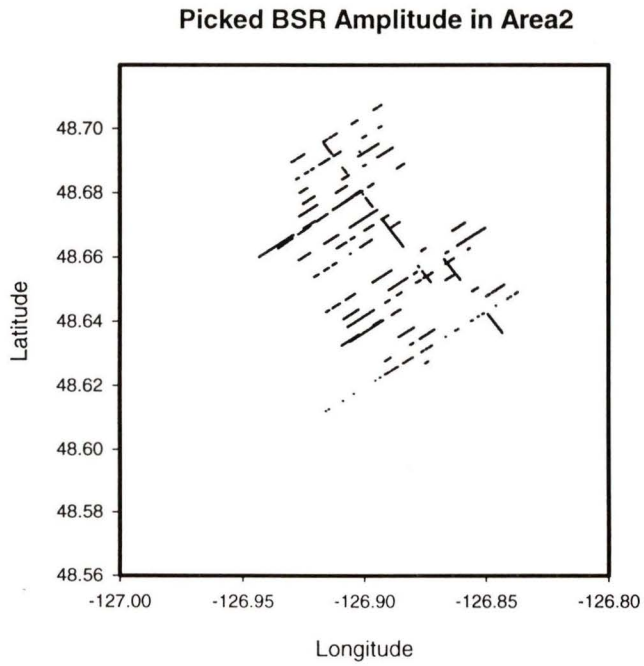
$$RC_{sf} = \frac{C_1 \cdot A_{sf_multiple}}{A_{sf_primary}}, \quad (3.2)$$

where $A_{sf_multiple}$ is the amplitude of seafloor water bottom multiple, $A_{primary}$ is the amplitude of the seafloor primary reflection and C_1 is a spherical divergence correction factor (figure 3.4). If a spherical divergence correction has already been applied in data processing, the C_1 equals 1.0.

The reflection coefficient of the BSR is calculated from seafloor reflection coefficient, simply by taking the ratio of the BSR and seafloor amplitude. In addition, transmission loss at the seafloor must be considered. For a unit incident wave amplitude, the amplitude of downward-going transmitted wave at the seafloor is $1 - RC_{sf}$. The amplitude of the upward-going transmitted wave at the seafloor can be written as $1 + RC_{sf}$ because the reflection coefficient becomes negative when the



(a) Picked seafloor amplitude in Area 2.



(b) Picked BSR amplitude in Area 2.

Figure 3.3 Picked seafloor and BSR amplitude in Area 2.

propagation direction is reversed. The amplitude ratio between the seafloor primary and BSR primary can be written as:

$$\frac{A_{sf}}{A_{bsr}} = \frac{RC_{sf}}{(1 - RC_{sf})RC_{bsr}(1 + RC_{sf})}, \quad (3.3)$$

so that:

$$RC_{bsr} = \frac{A_{bsr}}{A_{sf}} \cdot \frac{RC_{sf}}{(1 - RC_{sf}^2)}, \quad (3.4)$$

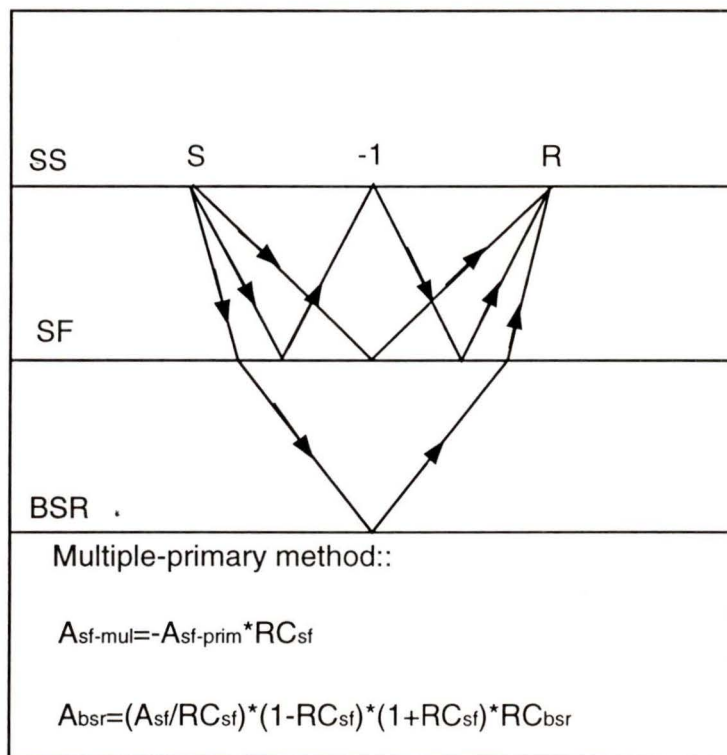


Figure 3.4 Seafloor and BSR RC calculation using multiple/primary method.

According to Warner (1990), there are three premises in this method of reflection coefficient calculation:

1. Receiver offset is small compared to water depth so that wave propagation is nearly vertical. In this sense, the calculated reflection coefficient is the vertical reflection coefficient.

2. Seafloor is a simple interface between liquids and elastic solid half space such that no energy is lost due to non-elastic processes.

3. Seafloor is flat and smooth so that there is no need to consider defocusing and scattering due to topographic variations.

After NMO correction, the stack section is zero-offset so that the first condition is satisfied.

The second premise is not strictly satisfied. From physical property measurements of sediment cores collected in this region, the seafloor is generally covered by a layer of soft mud with a maximum thickness of 2.5 m over the deep sedimentary basin and a density as low as 1300 kg/m^3 . Below this layer is normal denser glacial clay with a bulk density of about $1600\text{-}1650 \text{ kg/m}^3$. The transition from the seafloor to the denser layer is normally a uniform gradient.

Topographic effects on amplitude cannot be ignored on the slope region. The slope of the seafloor is about 15° so that less energy was received within the receiving aperture when shooting updip than when shooting downdip. Scattering due to small-scale topographic variations ($\ll \lambda$) should be considered as a very important source of energy loss, too. It is difficult, however, to determine this part of the loss quantitatively because of the unknown seafloor roughness. Topographic effects will be discussed in detail later.

3.4.2 By Amplitude Scaling

A conversion factor between seafloor amplitude and reflection coefficient is needed for the entire area. This factor can be obtained by scaling the seafloor amplitude using the reflection coefficients calculated by the multiple/primary method in a region where the effects of defocusing and scattering effect are minimized.

This method assumes that the source amplitude remains constant over the entire survey and there is no gain control applied to the seismic data. This assumption is valid because the gun pressure was maintained at a constant level of 1800 PSI during most of the survey except airgun pressure was extremely low (600 PSI) due to air leakage over the east part of line 11, near the cross point of L89-10 and L89-08.

Selection of seismic lines used to calculate the conversion factor is crucial for this method. The assumptions mentioned above are also used as the selection criteria for seismic lines used in the conversion factor calculation. Figure 3.5 shows the seafloor raw amplitude and reflection coefficient using multiple/primary ratios on a trace-by-trace basis for line 17 (figure 3.1 d) and for line 24 (figure 3.1 g). In the shaded region, where both seafloor and WBM amplitude are nearly constant, the seafloor is smooth. The average seafloor amplitude was 740 for line 17 and 640 for line 24, while the WBM amplitude was 156 for line 17 and 118 for line 24. A conversion factor of 0.000286 was finally obtained.

Reflection coefficients calculated from the bulk density data provide additional constraints on this method. The seafloor raw amplitude near core 18 located on the flat portion of line 17, which was one of the lines selected for the conversion factor calculation, was about 820, giving a reflection coefficient of 0.234.

It is consistent with the value calculated from bulk density of core 18, where a value of 0.25 was obtained corresponding to an average seafloor density of 1720 kg/m^3 . The difference of only 6% indicates that we can safely calculate the seafloor reflection coefficient by amplitude scaling.

The BSR reflection coefficient RC_{bsr} is calculated from the BSR amplitude using the following formula:

$$RC_{bsr} = A_{bsr} \frac{C}{(1 - A_{sf}^2 \cdot C^2)}, \quad (3.5)$$

where C is the seafloor amplitude conversion factor 0.000286 as determined from the primary-multiple analyses of seafloor amplitude. Transmission loss correction is applied.

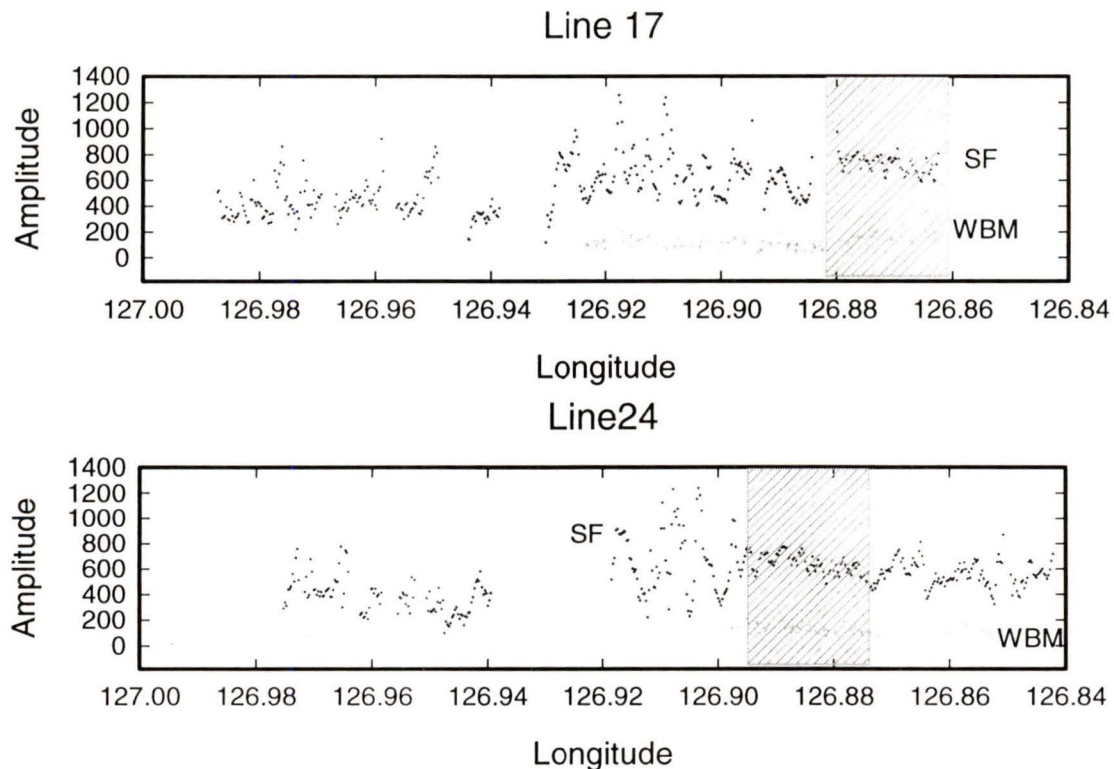


Figure 3.5 Seafloor amplitude conversion factor calculation. Flat seafloor with rather constant seafloor and WBM amplitude is chosen. A factor of 0.000286 is obtained.

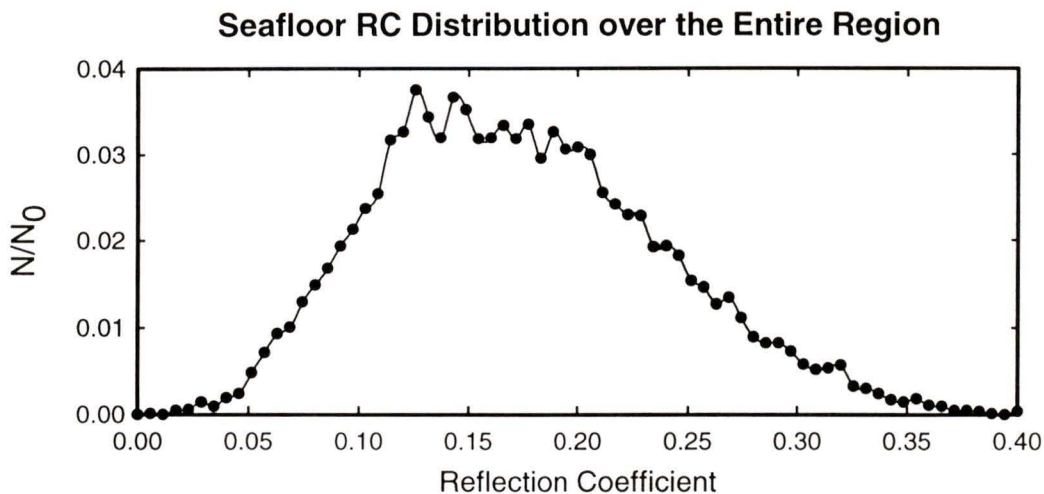
3.5 Distribution of Reflection Coefficients

The seafloor reflection coefficients derived from amplitude scaling span a large range from 0.07 to 0.4 (figure 3.6 a). A total of 8262 reflection coefficients were determined and approximately 50% of these values were uniformly distributed from 0.11 to 0.20, while only less than 1.5 % were greater than 0.34.

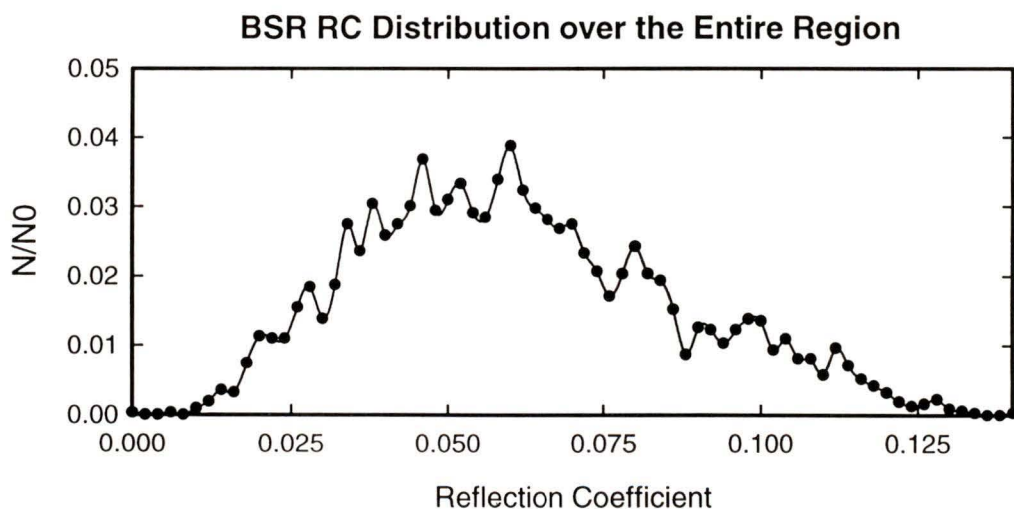
For BSR reflection coefficients, a total of 3095 values were derived from amplitude scaling, corrected for transmission loss. BSR reflection coefficients span a range from 0.01 to 0.14, with more than 50% from 0.03 to 0.08 and less than 1% greater than 0.13 (figure 3.6 b).

The spatial distribution of seafloor reflection coefficients derived from amplitude scaling is shown in figure 3.7a. High reflection coefficients mainly appear in the region where water depths are less than 1400 m, especially on the west flank of the local topographic high located at (126°53.7'W, 48°40.2'N). A region of low reflection coefficients appears to be correlated with this topographic high. The inline direction amplitude/reflection coefficient trough near the intersection of L89-10 and L89-08, at the easternmost part of line 11, is located where the air gun pressure was only 600 PSI due to air leakage. The low amplitude region centred at (126°52', 48°39') is bounded by the east part of line 20 and line 25. This corresponds to a small slope basin (e.g., see figure 3.1e, line 22, SCMP 2200-6200). In the deep sedimentary basin, where the bulk density is the lowest (core 17), the seismic reflection coefficient is normally lower than 0.17.

Seafloor reflection coefficients derived from a trace-by-trace WBM method (figure 3.7 b) also show a low reflection coefficient region over the local topographic



(a) Distribution of seafloor RC from amplitude scaling. N_0 is the number of calculated seafloor RC (8262). RC higher than 0.34 and lower than 0.05 has been ruled out with the same data editing method applied on WBM RC. Dominant RC has a larger range from 0.12 to 0.22, compared with that derived from WBTM. This is due to the addition of the RC in the deep sedimentary basin.



(b) Distribution of BSR RC from amplitude scaling and transmission loss correction. N_0 is the number of total calculated BSR RC (3095). RC higher than 0.12 has been ruled out with the same data editing method applied on WBM RC.

Figure 3.6 Seafloor and BSR reflection coefficient distribution.

Seafloor Amplitude and RC(by Amplitude Scaling)

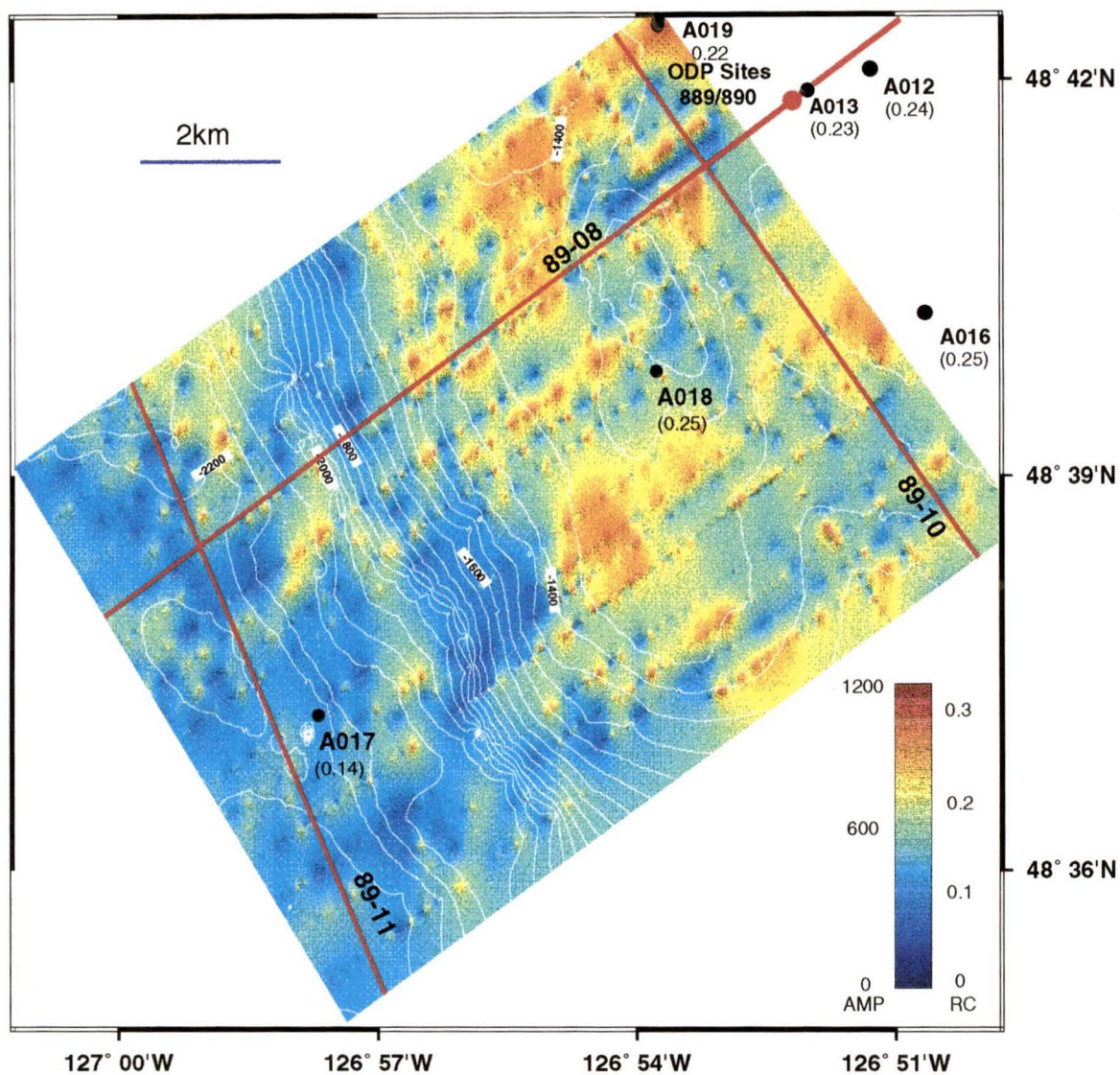


Figure 3.7 (a) Seafloor raw amplitude and seismic RC (by amplitude scaling) distribution over entire survey area. Numbers in parenthesis under core numbers are RC calculated from core bulk density.

Seafloor RC (Using WBM)

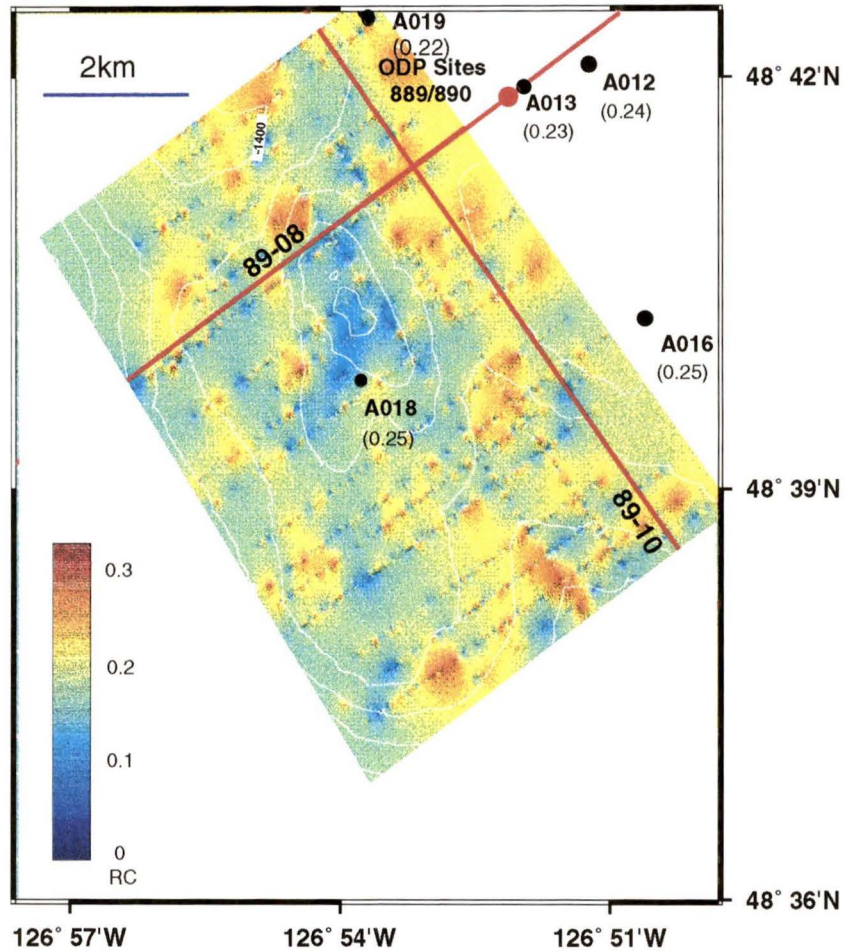


Figure 3.7 (b) Seafloor seismic RC(using multiple/primary method on a trace-by-trace basis) distribution over the local topographic high. White lines are bathymetry contours, red lines are low frequency multichannel seismic lines, solid circles are coring locations, the red solid circle is ODP Sites 889/890. Numbers in parenthesis below core numbers are bulk density RC.

high. The slope basin bounded by line 20 and line 25 shows higher values than that derived from amplitude scaling. This result is unlikely to be reliable because the bulk density of surface sediments in this basin should be less than that in the rest part of the shallow water region. A comparable difference in the reflection coefficient calculation by the two different methods was also noted by Fink (1995) and Fink & Spence (1998).

The overall pattern of BSR reflection coefficients by amplitude scaling and transmission correction (figure 3.8) is similar to that of raw amplitude (figure 3.9). It is rather uniform over the entire shallow water part and has some correlation with topography. Some localized high values appear between 1300 m and 1400 m bathymetry contours and over the local topographic high. The correlation, however, is not as strong as that in the adjacent 1993 survey region to the northeast [Fink & Spence, 1998].

3.6 Topography and Roughness Effects on Reflection Coefficient Calculation

Dipping seafloor causes increased and decreased seafloor amplitude when shooting downdip and updip, respectively. However, this effect seems to be small. Assuming a water depth of 1300 m, the aperture angles in which energy can be received by the receiver array are 4.11° for a flat region, 3.78° for downdip shooting and 4.30° for updip shooting. The total received energy for downdip shooting is 8% less than over the flat region, while it is 5% more for updip shooting. This leads to the same amount of reflection coefficient variation. Defocusing and focusing effects over

BSR RC (by Amplitude Scaling)

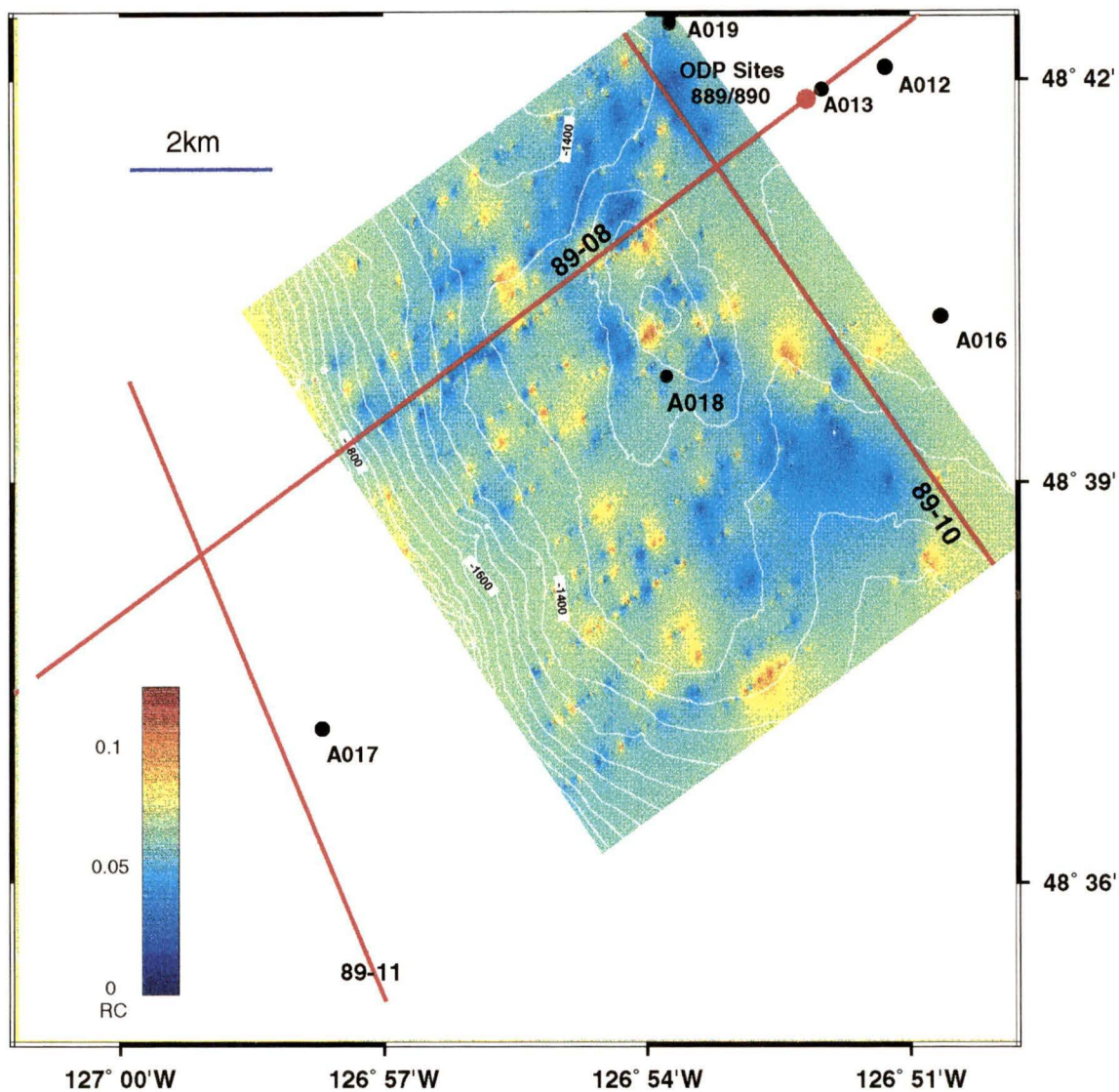


Figure 3.8 BSR RC (by amplitude scaling and transmission correction) distribution over the shallow water region. RCs higher than 0.13 are removed for lack of continuity.

BSR Raw Amplitude

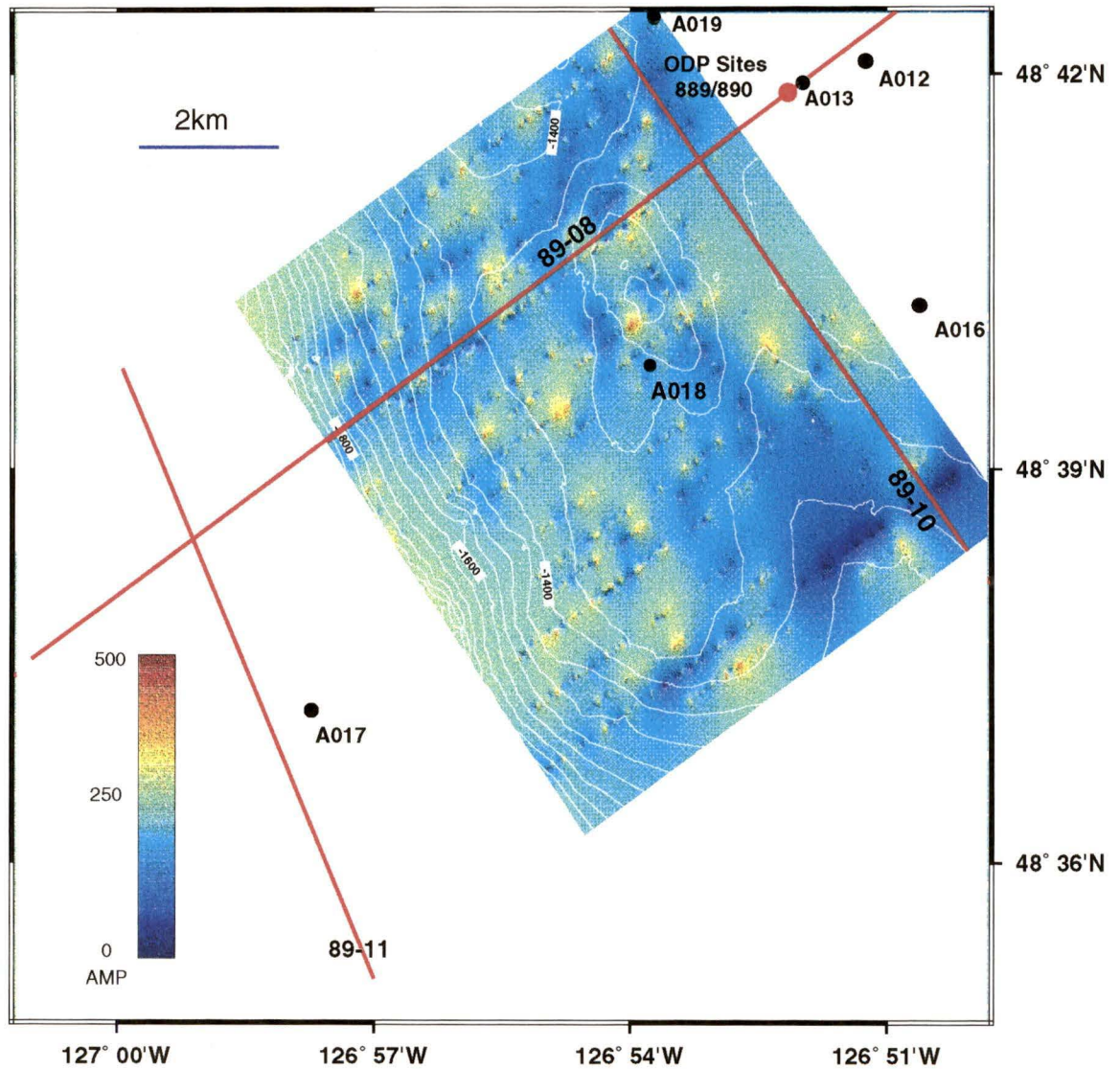


Figure 3.9 BSR raw amplitude distribution over the local topographic high. High amplitude appears on the west flank of the local topographic high in the shallow water region.

the shallow region can be ignored since the major part of this region is flat except for the small hill with a height of about 100 m and an in-line length of about 1200m.

Scattering due to small-scale topographic variation ($\ll \lambda$) should be considered as another source of energy loss. The reflection coefficient derived from the multiple-primary method is a coherent energy reflection coefficient rather than a real seafloor reflection coefficient. If we consider the reflection coefficient calculated from sediment bulk density as “real” and those derived from seismic method as “coherent”, the roughness of seafloor can be estimated using:

$$\frac{RC_c}{RC_b} = \exp(-2k^2\sigma^2 \cos^2 \theta), \quad (3.6)$$

where RC_c and RC_b are coherent and real reflection coefficients, respectively, k is the dominant wave number, σ is root-mean-square (RMS) roughness of seafloor and θ is the incident angle of coherent energy [Clay & Medwin, 1977].

RC_c is the seismic reflection coefficient and RC_b can be derived from bulk density measurement. The dominant seafloor reflection coefficient over the shallow water region is about 0.20. The real reflection coefficient RC_b can be estimated by averaging the bulk density reflection coefficient at cores 12, 13, 14, 16, 18 and 19 over the shallow water region. A value of 0.239 is obtained. For the case of vertical incidence, θ is 0° . The incident wave number is $2\pi/\lambda$, where λ is the wavelength (20m for 75 Hz in seawater). The calculated RMS seafloor roughness over the topographic high is 0.95 m.

Extremely high reflection coefficient values (>0.4) appear sparsely over the shallow water region, especially on the west flank of the local topographic high, where the reflection coefficients are generally higher than the rest of the region. This feature is very similar to that observed by Fink & Spence (1998). These high values were interpreted as indications of seafloor carbonate pavement with velocity and bulk density as high as 3000 m/s and 2290 kg/m^3 , much higher than normal seafloor sediment. The reflection coefficient generated by such a layer, if no tuning effect is considered, could be as high as 0.63. The formation of carbonate pavement could be enhanced by bottomward migrating fluid flow, which carries more methane to the water column [Fink, 1995]. However, there is only weak evidence of subsurface carbonates from the core observations in this region. The piston core barrels were severely bent at two locations (cores 15 and 17), and some carbonate nodules were collected at core 11. (although detailed chemical analyses of the nodules have not been carried out yet).

3.7 Correlation of Seafloor Seismic and Seafloor Density

Core 17 was located in the deep water sedimentary basin with water depth of 2200 m, similar to that at ODP Site 888 (2500 m). The average upper 4 m of core 17 has a similar bulk density and lithology (soft mud) as that at ODP Site 888.

Affected by the generally present soft mud, surface bulk density measurements of sediments in the shallow water region varies from 1330 kg/m^3 to about 1500 kg/m^3 , with higher values over the small hill. Over the small hill, the soft mud layer covering the seafloor was generally less than 5 cm in thickness because it was not seen at all in

the cores. Over the deeper water region, this layer was thick enough to survive the pore fluid sampling at the top of each core sections.

Seafloor reflected amplitude variation with the thickness of this soft mud layer can be simply calculated. Assume the incoming wave has a simplified form of:

$$A = A_0 \cos \omega t, \quad (3.7)$$

The general reflected wave on a surface covered by an intermediate density layer can be written as:

$$A_g = RC_1 A_0 \cos \omega t + RC_2 A_0 (1 - RC_1)(1 + RC_1) \bullet \cos(\omega t + \varphi), \quad (3.8)$$

where RC_1 and RC_2 are the reflection coefficients at the two boundaries as shown in figure 3.10, A_g is the comprehensive reflected amplitude function at the seafloor, A_0 is the absolute amplitude of incident wave. φ is the phase lag of the wave reflected from the bottom of this soft mud layer which is defined as:

$$\varphi = \frac{2Dm}{\lambda} \bullet 2\pi, \quad (3.9)$$

where Dm is the thickness of the soft mud layer.

Assuming the incoming amplitude is 1, it then can be simplified to:

$$RC_g = [RC_1 + RC_2 A_0 (1 - RC_1^2) \cos \varphi] \cos \omega t - [RC_2 (1 - RC_1^2) \sin \varphi] \sin \omega t, \quad (3.10)$$

where RC_g is the seafloor reflection coefficient function at time t . If we assume that the densities of the soft mud layer and the sediment below are 1300 kg/m^3 and 1600 kg/m^3 , respectively, both RC_1 and RC_2 are approximately 0.12, the formula above can be further simplified as:

$$RC_g = (0.12 + 0.119 \cos \varphi) \cos \omega t - 0.119 \sin \varphi \sin \omega t, \quad (3.11)$$

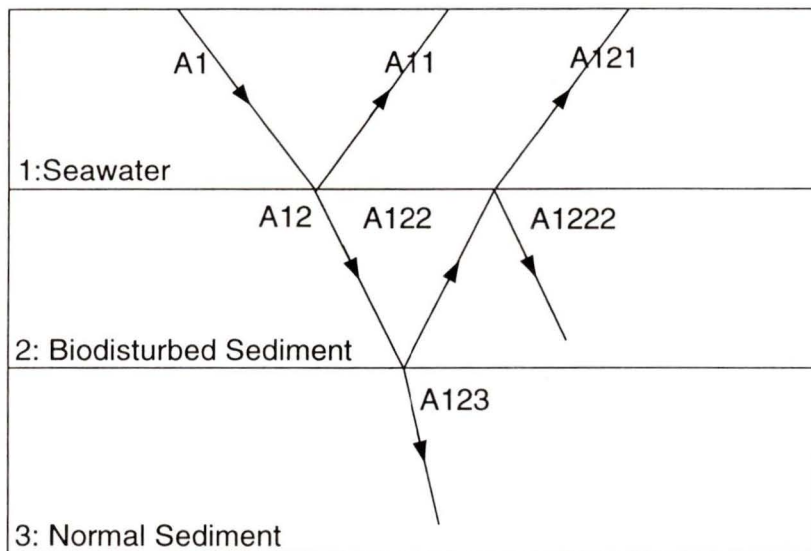
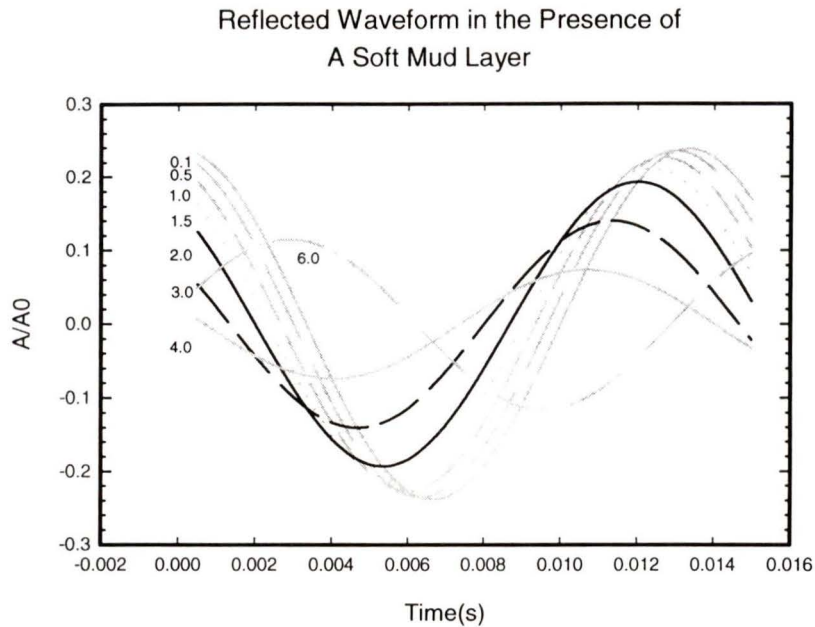


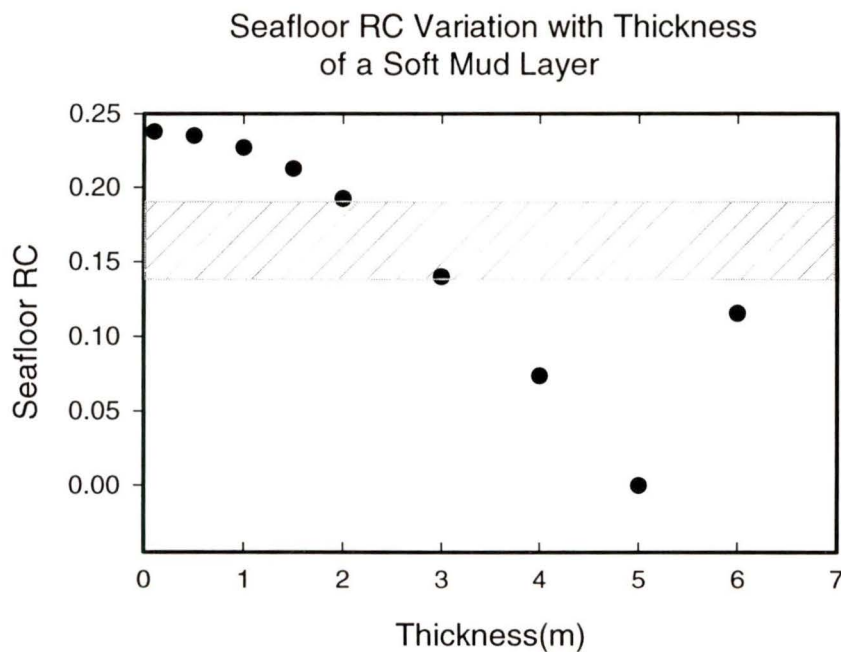
Figure 3.10 Calculation of reflected amplitude with the presence of soft mud layer, assuming incident amplitude is unit. Incident angle is exaggerated for clarity. Reflected amplitude is the result of interference of A11 and A121.

The values for the amplitude terms for $\cos\omega t$ and $\sin\omega t$ for different thicknesses are listed in table 3.2. The reflected waveforms are shown in figure 3.11a, assuming the frequency of the incident wave is 75Hz with a wavelength of 20 m. The maximum waveform amplitudes for the different thickness are shown in figure 3.11b. The maximum reflection coefficient value was set to 0.24, representing the mean value of reflection coefficients from cores in the shallow water portion of the survey area.

Very thin layers less than 1.0 m do not reduce the reflection coefficient dramatically. The minimum value occurs at $\frac{1}{4}$ wavelength (5 m), for which the reflected wave from the bottom of this soft mud layer is 180° out of phase with the seafloor reflection. Similar seafloor reflection coefficients as in the deep water sedimentary basin occur between the 2 m and 3 m curves. This calculated thickness is



(a) Seafloor waveform and amplitude variation with the thickness of the soft mud layer. Incident wave is 75Hz simple sinusoidal wave with amplitude of 1.



(b) Seafloor amplitude (incident amplitude is 1) variation with the thickness of the soft mud layer. Very thin layers less than 1.0 m do not reduce the amplitude dramatically. Shaded area is the dominant seafloor reflection coefficient observed in the deep sedimentary basin. This range indicates the thickness of the soft mud layer is from 2m to 3m, which is consistent with that measured in core 17.

Figure 3.11 Seafloor reflected waveform and reflection coefficient in the presence of a soft mud layer.

very consistent with that measured from core 17 (2.5 m). This result can explain why the reflection coefficient is generally higher on the topographic high region than in the deep water sedimentary basin. Figure 3.12 shows the seismograms for the different thickness of this layer, using a more realistic input wavelet determined by averaging seafloor waveforms from 100 stacked traces. Seismogram was calculated using Hampson Russell AVO package.

Thickness(m)	Phase Lag	$0.12+0.119 \cos\phi$	$0.119 \sin\phi$	Amplitude
0.1	0.0628	0.2386	0.007	0.2387
0.5	0.314	0.2329	0.0367	0.2358
1.0	0.6283	0.216	0.0698	0.2270
1.5	0.9427	0.1905	0.0961	0.2133
2.0	1.2566	0.1567	0.1129	0.1931
3.0	1.8849	0.0832	0.113	0.1403
4.0	2.5133	0.0238	0.0698	0.0737
6.0	3.7699	0.0238	-0.0698	0.0737
8.0	5.0265	0.1567	-0.1129	0.1931

Table 3.2 Amplitude of reflected wave at different thickness of soft mud layer.

3.8 BSR Depth Variation in Area 2

The BSR has been used to infer heat flow in continental margin settings [Yamanoto et al., 1992] because its depth below seafloor is controlled by the geothermal gradient. BSR depth generally increases with water depth because the increasing pressure allows gas hydrate formation at higher temperature.

The BSR time-depth variation in Area 2 is shown in figure 3.13. On the shallow part, BSR depth is normally 250-270 ms below seafloor, while in the deep

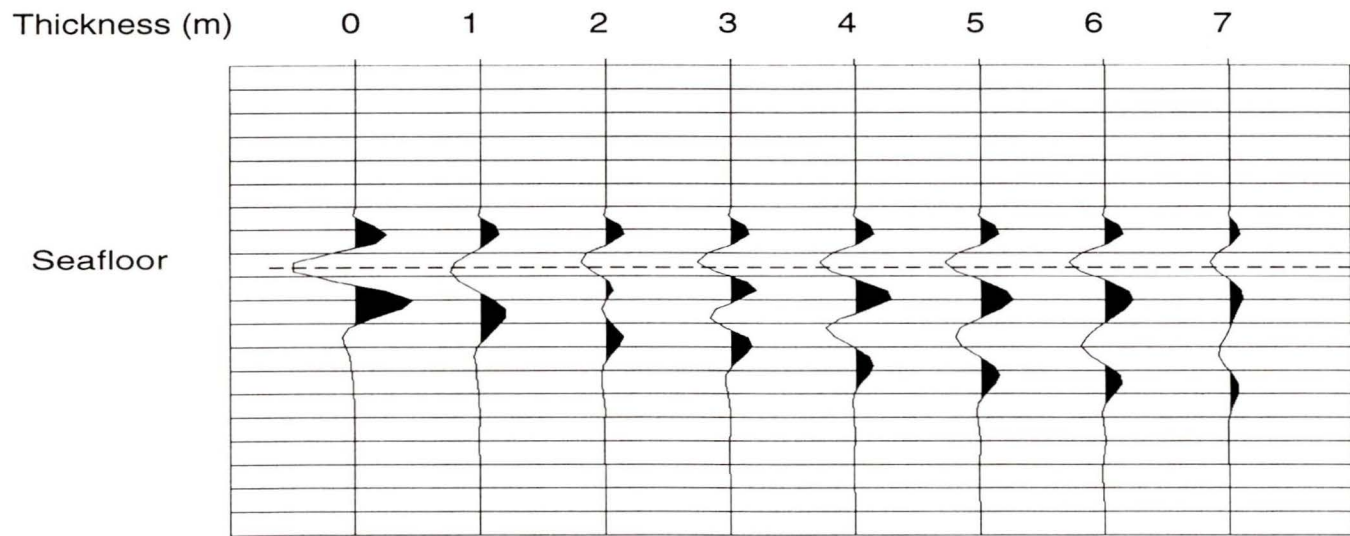
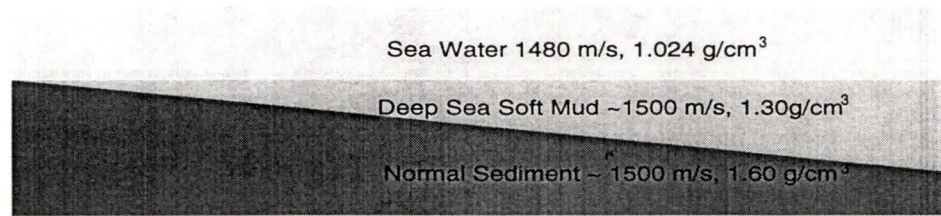


Figure 3.12 Seafloor reflected amplitude with the presence of soft mud layer. Seafloor signature is used as incident wave.

BSR Time Depth

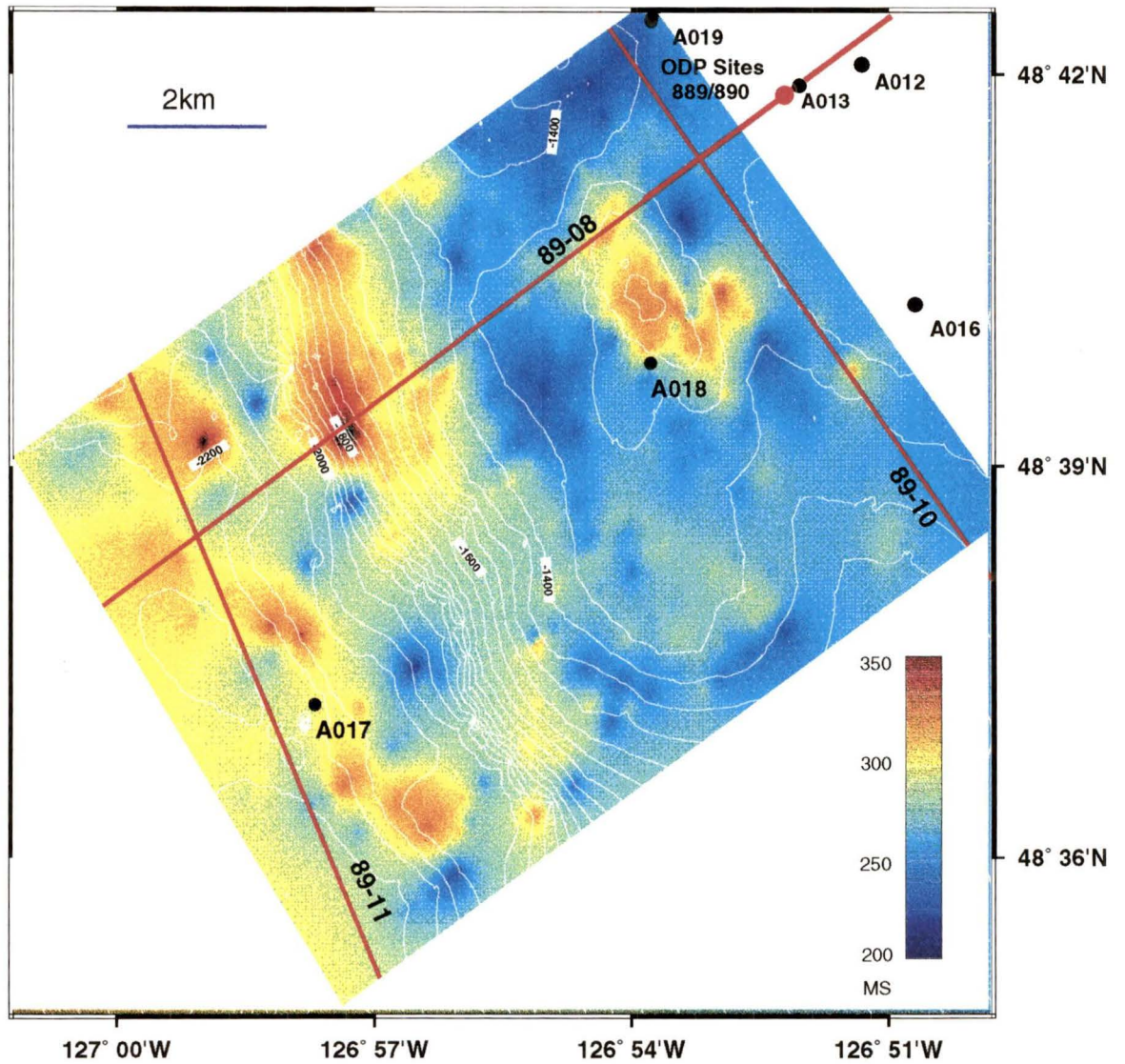


Figure 3.13 BSR time depth in Area 2. The BSR normally gets shallower when water depth decrease. However, there is a region over the local topography high in the shallow water region.

sedimentary basin the depth is typically 300 ms. A 300 ms-anomaly region is clearly seen over the local topographic high. This increased BSR depth indicates a localized region of low heat flow (Ganguly et al, 1998). The low heat flow may be partially due to topographic disturbance of thermal gradients, but may also reflect the underthrusting of colder sediments beneath the topographic high (Davis et al, 1990; Ganguly et al, 1998).

3.9 Tying Seismic Reflection Coefficient from MCS and SCS Data

In figure 3.14, seafloor reflection coefficients (by amplitude scaling) over the track of MCS Line 89-10 were projected from the interpreted reflection coefficient grid of the thesis survey (figure 3.7) and from the SCS reflection grid of Fink (1995). Reflection coefficients from Lines 32 and 33, which were run parallel to Line 89-10, were also plotted. The consistency between the interpolated values and those from Line 32 and Line 33 indicates the reliability of the interpolation program. Some differences exist but are expected because the values projected from the interpolated grid involve averaging in directions both parallel and perpendicular to Line 89-10. Interpolation in the direction parallel to Line 89-10 is about 400 m, compared to a shot spacing of 24 m on Line 32 and Line 33. MCS and SCS reflection coefficients show some rough correlation north of latitude 48.68° . On the rest of the line, SCS reflection coefficients increase southward while the MCS reflection coefficients keep rather constant except for the low value at 48.655° and 48.645° . These very high RC values were present only on a single line in the 1993 survey. Perhaps there were line location or airgun pressure problems in the 1993 SCS survey.

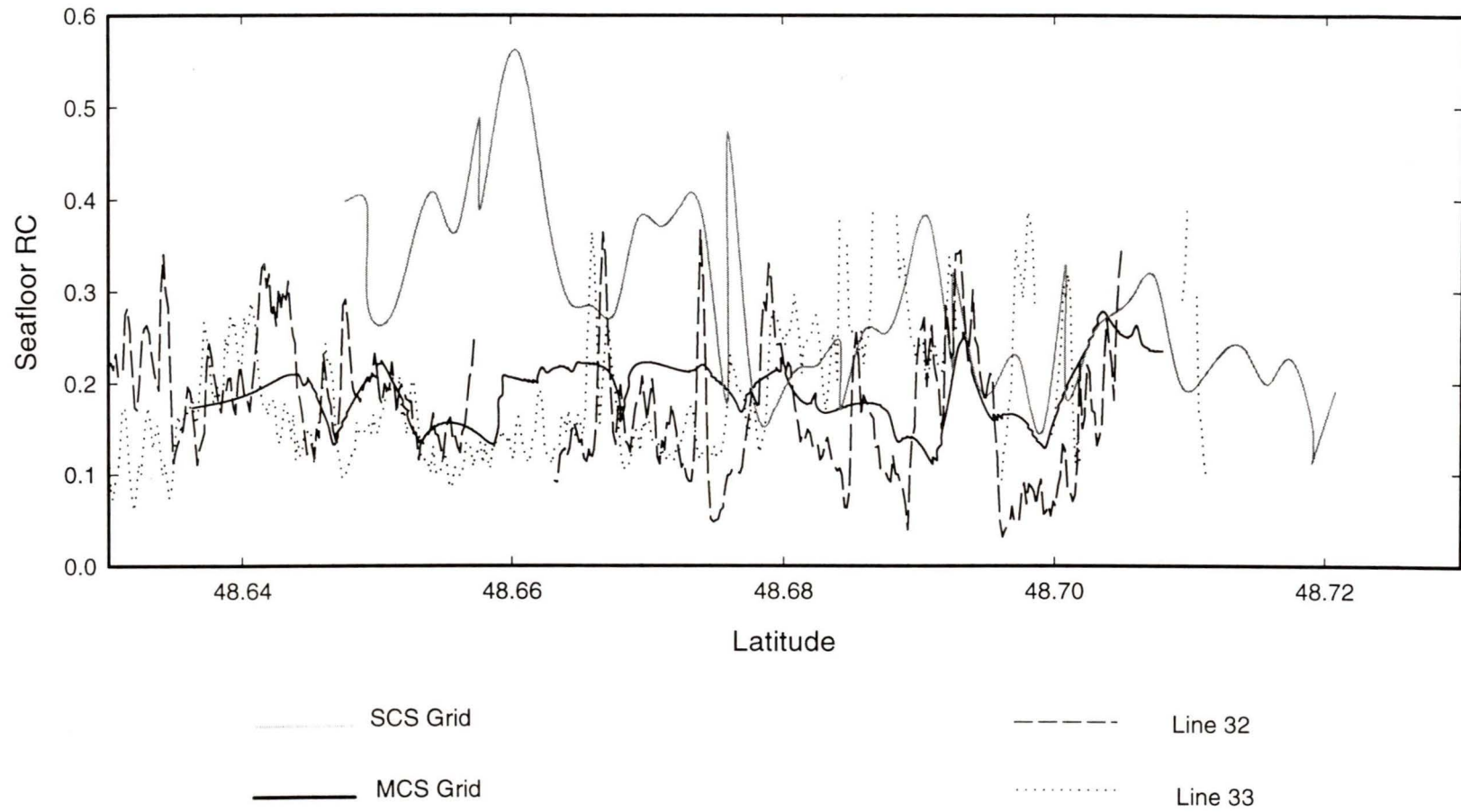


Figure 3.14 Correlation of seafloor RC from MCS and SCS data over the eastern part of Area2, where MCS and SCS survey overlaped. RC from MCS and SCS grids were projected from interpolated RC grids. Line 32 and 33 are parallell lines 800 m and 400 m west of Line 89-10.

3.10 Possibility of Seafloor Carbonate Pavement

There was no direct visual evidence of seafloor carbonate from the cores collected in the regions where its presence was suggested based on earlier studies. The highest seismic reflection coefficient values in Area 2 were about 0.4. These values were sparsely distributed and show little spatial continuity. However, we still can not totally rule out the possibility of localized occurrences of high velocity carbonate pavement. The bending of coring barrel at core 15 might be evidence in the favor of its existence. Also, high frequency seismic data, collected in May 1997 in the same region using a deep towed acquisition system, clearly showed a strong reflector about 10 mbsf [Walia et al, Cruise Report, 1998]. A possible explanation is that the earlier formed carbonate pavement is covered by recent seafloor sediment and the cores were not long enough to reach its depth.

Chapter 4. Gas Hydrate and Free Gas Zone Characterization

Introduction

A generally accepted massive gas hydrate velocity is about 3730m/s [Pearson et al., 1983; Sloan, 1990, Whalley, 1980], so that hydrated sediments usually have higher P-wave velocity than that of normal sediment. In this chapter, the amount of gas hydrate will be estimated from the P-wave velocity enhancement, which can be derived from the BSR reflection coefficient.

The free gas saturation below the BSR is difficult to estimate because a small quantity of free gas (e.g. 1-2% of the pore space) can reduce sediment velocities significantly, while a further increase in gas saturation has a much smaller effect [Domenico, 1976]. However, an upper limit of free gas saturation is available from the lowest velocity of free gas charged sediments.

The western flank of the shallow water region in Area 2 has a similar deposition environment as that at Site 889/890. Accreted Neogene and Pliocene sediment is overlain by undeformed Quaternary slope sediments which thin westward. In the vicinity of a local fault zone in this region, a reflector about 16 – 30 ms below the BSR was observed. In this chapter, the results of forward modeling based on waveform fitting are presented. Two possible velocity and density configurations near the BSR were obtained, suggesting the presence of either an overconsolidated sediment layer just below the BSR or a second free gas layer separated from the first one by an impermeable sediment layer.

4.1 Free Gas Saturation Estimation.

For porous media, Geertsma [1961] obtained the P-wave velocity as a function of frequency of the propagation of the elastic wave field, as well as for the limiting case of zero and infinite frequencies. The P-wave velocity and S-wave velocity for partially gas-saturated oceanic sediment at infinite frequency can be used to estimate velocity from gas saturation or vice versa.

Figure 4.1 shows the variation of computed velocities and Poisson's ratio in marine sediment (50% porosity) at ~200 mbsf with methane gas saturation in percentage of pore space [Yuan et al, 1996]. The hatched area indicates the most likely methane gas saturation of 0-5%, according to the velocity measurement from VSP and velocity analyses on multichannel seismic data. The dramatic decrease of V_p with only a few percent free gas makes estimation of free gas saturation difficult. We can safely conclude, however, that the gas saturation should be less than 5% of pore space.

4.2 Gas Hydrate concentration Estimation

The concentration of gas hydrate above the BSR was estimated using a simple time-average approach, following Yuan et al (1996). The velocity of fully hydrate-saturated sediment can be obtained for the combination of pure gas hydrate and sediment matrix. This velocity is then combined with the velocity of water-saturated sediment (zero hydrate saturation) to determine the overall velocity [Lee et al, 1993; Wood et al., 1994].

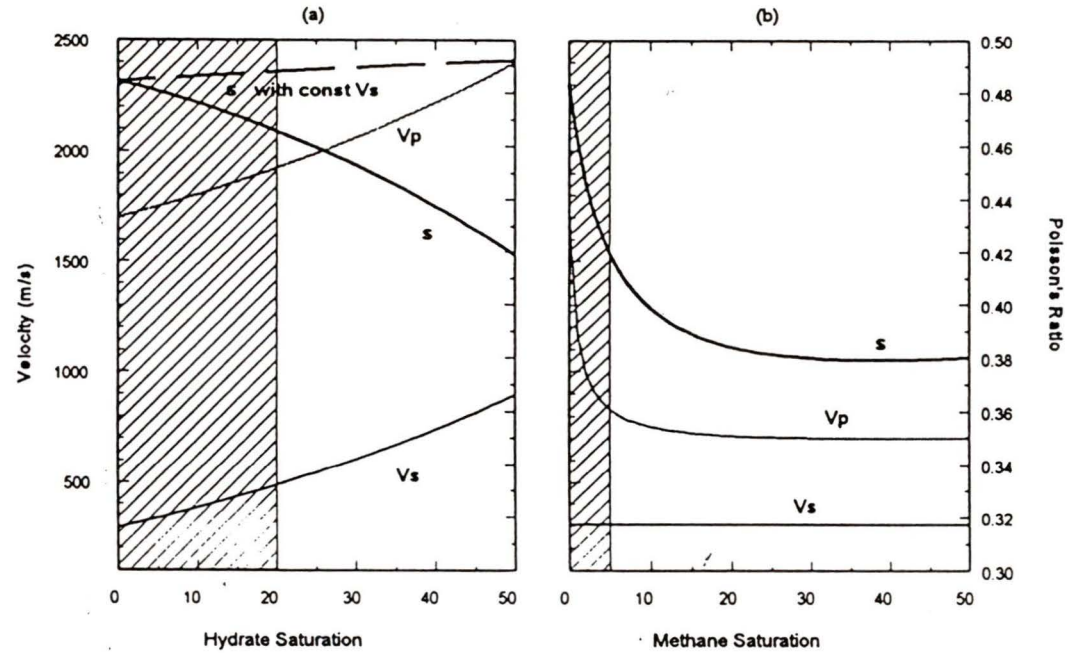


Figure 4.1 Variations of computed velocities and Poisson's ratio in marine sediment at 200m sub-bottom with hydrate saturation (a) and methane gas saturation (b) in percentage of pore space. Hatched areas indicate the most likely hydrate saturation of 0~20% and methane saturation of 0~10% (from Yuan et al, 1996)

The fully hydrate-saturated sediment velocity, V_{hyse} , can be written as:

$$\frac{1}{V_{hyse}} = \frac{\phi}{V_{hydrate}} + \frac{1-\phi}{V_{matrix}}, \quad (4.1)$$

where $V_{hydrate}$ is the P wave velocity for pure gas hydrate and is taken to be 3730m/s [Pearson et al., 1983; Sloan, 1990], V_{matrix} is the P wave velocity of the sediment matrix, taken to be 4500 m/s [Davis and Villinger, 1992] and ϕ is the sediment porosity. According to porosity measurements at ODP Site 889/890, the typical porosity ranges from 45% to 55% at the depth of the BSR and the calculated V_{hyse} are 4120 m/s and 4040 m/s, respectively. The velocity of partially hydrate-saturated sediment, V_p , can be written as:

$$\frac{1}{V_p} = \frac{S}{V_{hyse}} + \frac{1-S}{V_{sed}}, \quad (4.2)$$

where V_{sed} is the water saturated sediment velocity and S is the volume of hydrated sediment.

The sediment velocity above the BSR can be estimated from the BSR reflection coefficient by assuming a reasonable velocity for gas-saturated sediment below the BSR. Assuming no density contrast across the BSR, the reflection coefficient is:

$$RC = \frac{v_2 - v_1}{v_2 + v_1}, \quad (4.3)$$

where v_1 and v_2 are velocities above and below the BSR. This equation can be rearranged to give:

$$V_p = V_{gsed} \cdot \frac{1 - RC_{bsr}}{1 + RC_{bsr}}, \quad (4.4)$$

where V_{gsed} is the velocity of gas-charged sediment. Its velocity was taken as 1515 m/s based on the average value for the three VSP data points below the BSR. The gas hydrate saturation is then written as:

$$S = \left(\frac{1}{V_{gsed}} \cdot \frac{1 + RC_{bsr}}{1 - RC_{bsr}} - \frac{1}{V_{sed}} \right) \cdot \frac{V_{hysed} V_{sed}}{V_{sed} - V_{hysed}}, \quad (4.5)$$

The calculation of S depends very much on the value of V_{sed} , which represents the background velocity for water-saturated sediment with neither hydrate nor free gas. The selection of this velocity is mainly based on the velocities determined from MCS velocity analysis of Yuan (1996) in which the velocity ranges from 1600m/s to 1670m/s.

Background velocity selection gives a lower limit of the BSR reflection coefficient. At this velocity lower bound, it is assumed that there is no free gas in the sediment pore space. Background velocities of 1600 m/s and 1640 m/s gave BSR reflection coefficient lower bounds of 0.025 and 0.04, respectively. Because 0.04 is the typical BSR reflection coefficient values derived from low frequency MCS data on L89-08, the background velocity should be around 1640m/s. Small changes in background velocity only slightly change the hydrate saturation. For a typical BSR reflection coefficient of 0.06, 1600m/s gives a saturation of 10% while 1640m/s gives 6.6%. The variation of saturation with reflection coefficient based on the two background velocities is shown in figure 4.2.

The hydrate saturation immediately above the BSR in Area 2 was calculated with a background velocity of 1600m/s, V_{gsed} of 1515m/s and V_{hysed} of 4120m/s (figure 4.3). Based on this parameter selection, gas hydrate saturation typically ranges

from 5% to 15% of pore space. A reflection coefficient of 0.025 corresponds to zero hydrate saturation. The distribution pattern has some correlation with topography, with high values (>12.5%) concentrated over the local topographic high and its western flank. But this correlation is much weaker than that appeared in the adjacent region to the east surveyed in 1993 [Fink & Spence, 1998], where high saturation was very much concentrated over a local topographic high.

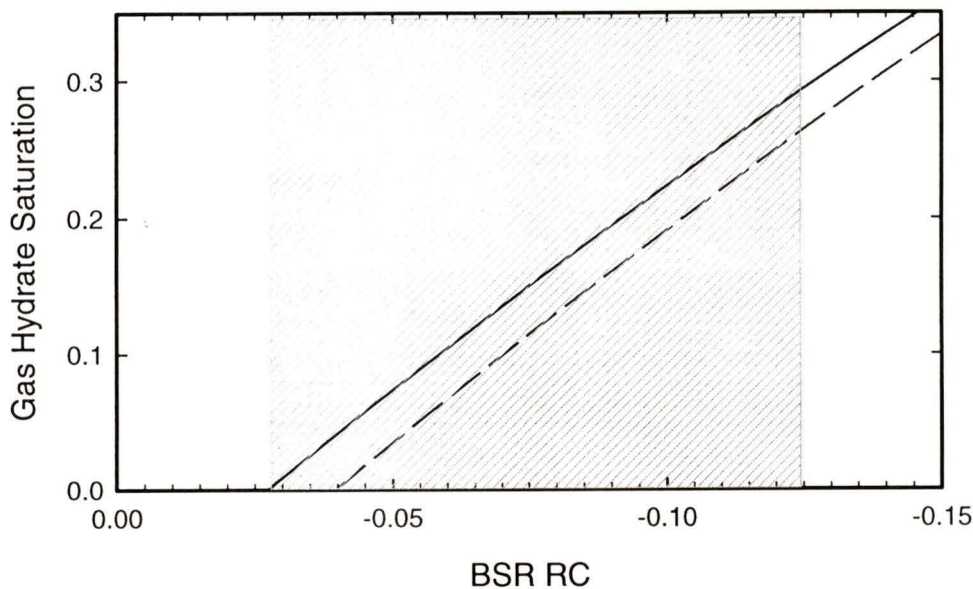


Figure 4.2 Gas hydrate saturation variation with BSR reflection coefficient, assuming a velocity of 1515 m/s below the BSR. Solid and dashed lines are saturation functions based on background velocities of 1600 m/s and 1640 m/s, respectively. Shaded region is the BSR reflection coefficient variation range in Area 2 (figure 3.6b). Gas hydrate saturation should be roughly no more than 30%. Saturation using 1600 m/s background velocity is about 3% higher than using 1640 m/s background velocity.

4.3 Forwarding Modeling of Gas Hydrate and Free Gas Distribution Across BSR

The typical BSR reflection coefficient in Area 2 ranges from 0.04-0.10, which requires a decrease in seismic impedance of 10-20%. Hyndman and Spence (1992) pointed out that the acoustic impedance contrast could be matched by a number of models with and without a gas layer below the BSR. For example, a BSR reflection

Hydrate Saturation Immediately Above the BSR

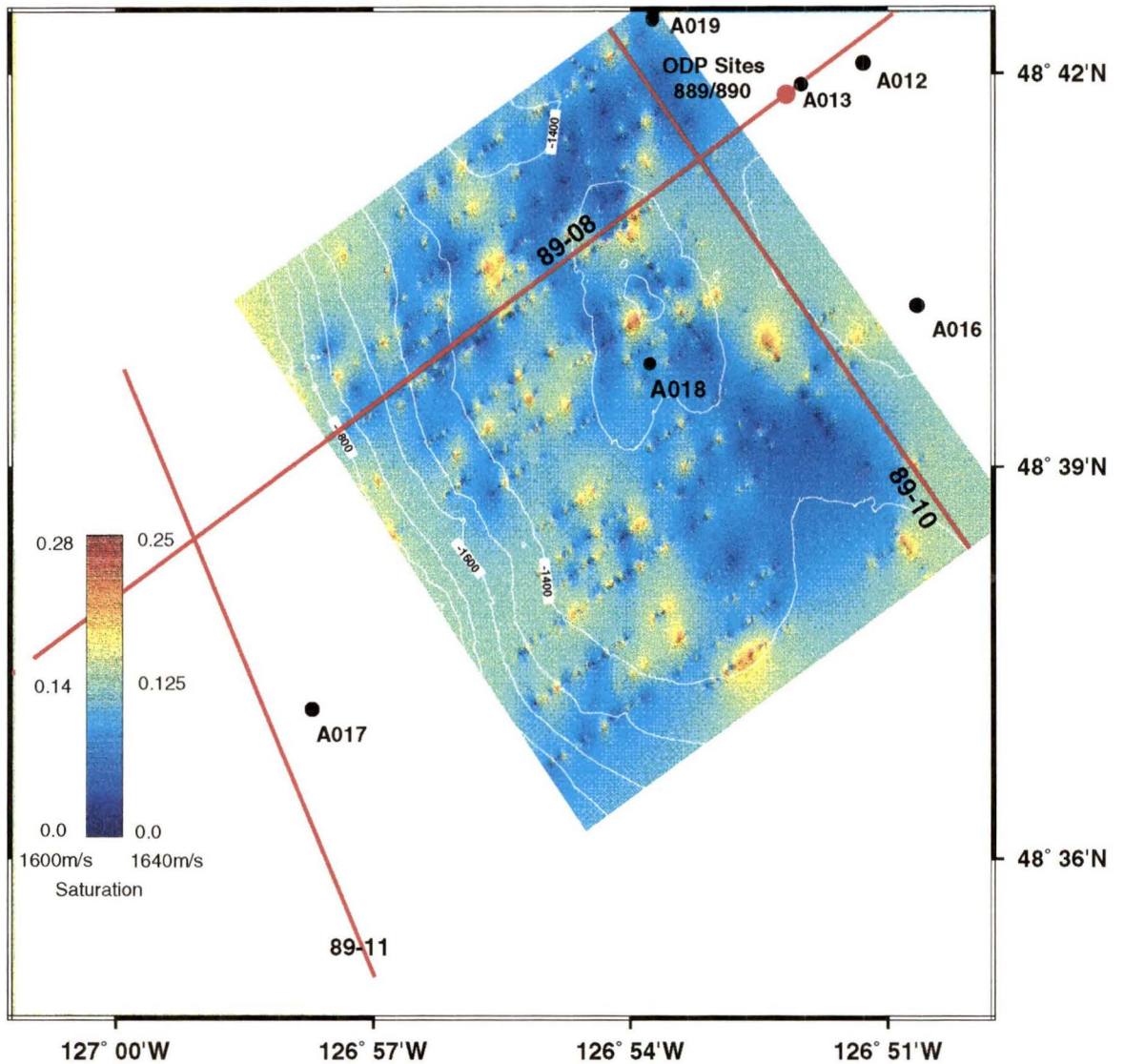


Figure 4.3 Gas hydrate saturation immediately above the BSR, assuming a velocity of 1515 m/s just below the BSR and background velocities of 1600 m/s and 1640 m/s.

coefficient of 0.10 offshore Peru was obtained by modeling a hydrate layer with 10% pore space occupied by gas hydrate and sufficient free gas beneath to reduce the velocity to as low as 1394 m/s [Miller et al., 1991].

Forward modeling of three gas hydrate and free gas configurations across the BSR were done by Hyndman and Spence in 1992. They are (1) a gas hydrate layer with a sharp base and a gradient top; (2) a layer with partially gas-charged porosity and only a small amount of overlying hydrate, and (3) a hydrate layer with a sharp base and a sharp top. Only the gradational hydrate layer model with a half thickness of greater than 15 m gives a reasonable fit in vertical incident waveform, reflection coefficient, velocity structure and amplitude-versus-offset (AVO) characteristics.

4.4 Observation and Modeling of Secondary BSR below Primary BSR

The typical BSR reflection is a single symmetrical wavelet with a reversed polarity relative to the seafloor reflection, indicating a sharp and negative acoustic impedance contrast across the BSR. Figure 4.4 shows a portion of Line 10 in Area 2 where a typical BSR reflection was observed.

On the western flank of the small hill on the local topographic high in Area 2, a reflector which has the same polarity as the BSR is well resolved from CDP10710 to 11520 about 30 ms below BSR (figure 4.5). This reflector is rather flat on the migrated section. The maximum thickness of 30 m occurs around CDP 10860, where seafloor and BSR penetrating faults are probably present, and reduces to zero around CDP11520. The length is about 550m. This reflector is unlikely to be a lithologic

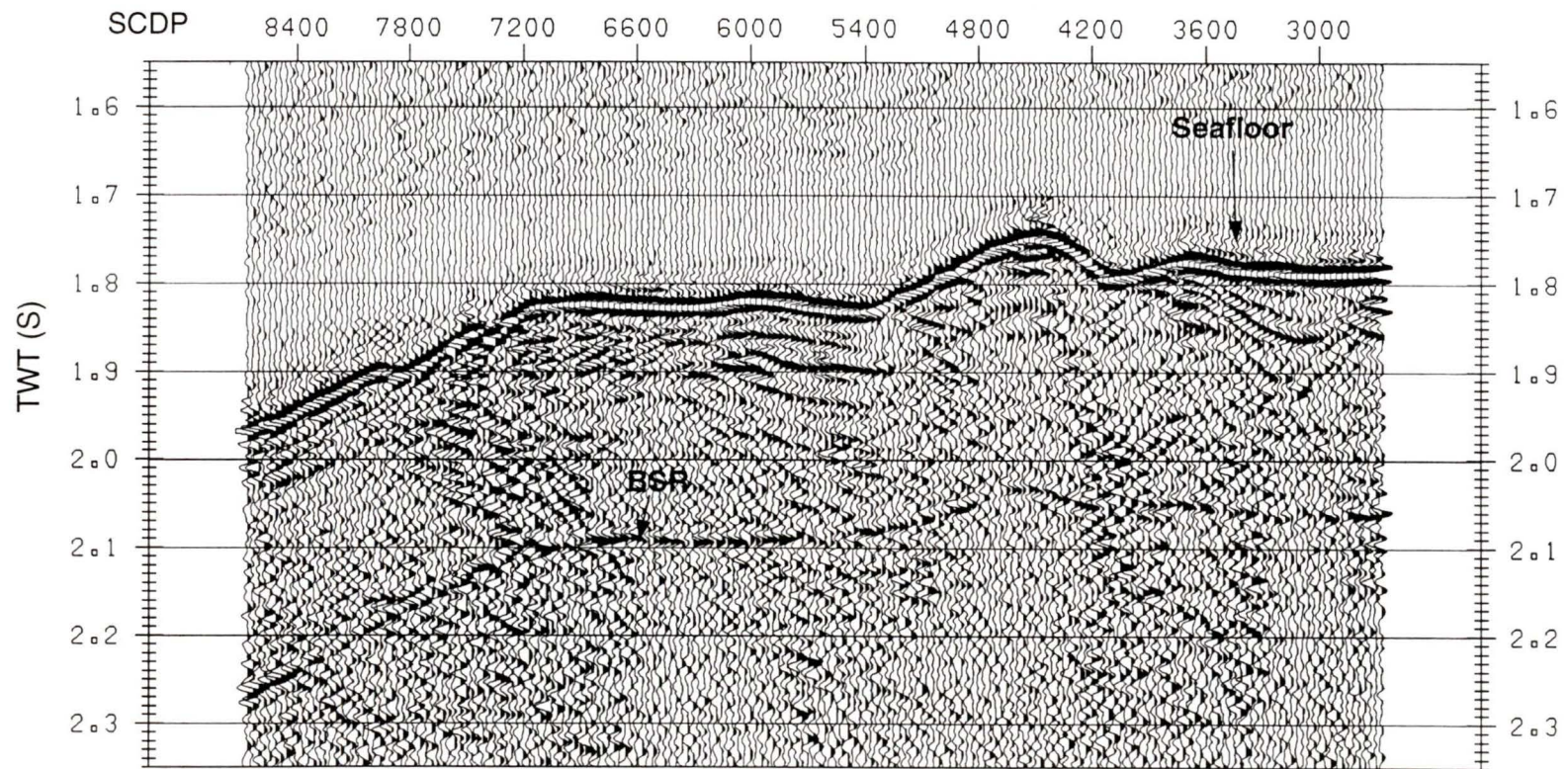


Figure 4.4 A portion of Line 10 in Area 2. A typical BSR has reversed polarity compared with the seafloor.

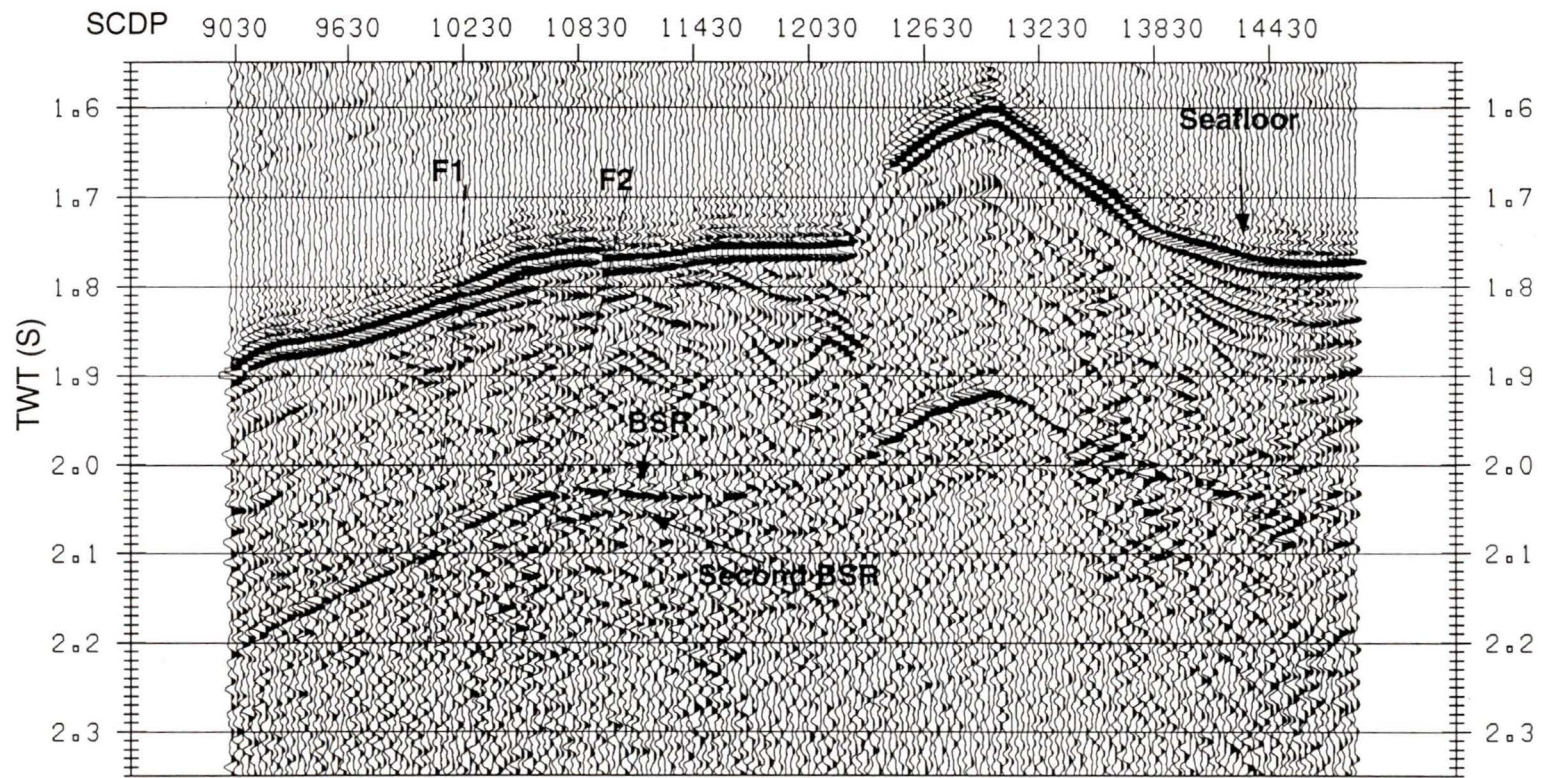


Figure 4.5 A portion of Line 13 in Area 2. A reflector 16~30 ms below the primary BSR is well resolved on the west flank of the local topography high. Sea floor and-BSR-cutting faults occur in the region above the reflector.

boundary because it is sub-parallel to the BSR and reflections in this deformed accretionary zone appear to be at high angle to the BSR and seafloor.

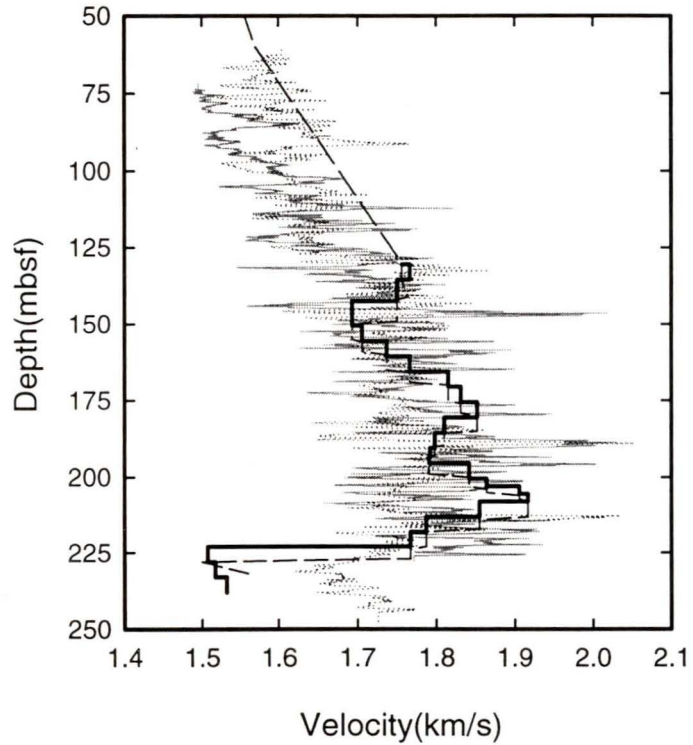
4.5 Forward Modeling on the Secondary BSR, Determination of Velocity and Density Structure

The reversed polarity of the secondary BSR indicates a negative acoustic impedance boundary. By matching the waveform of synthetic seismic data with the real seismic data, we tried to examine the velocity and density structure across this zone.

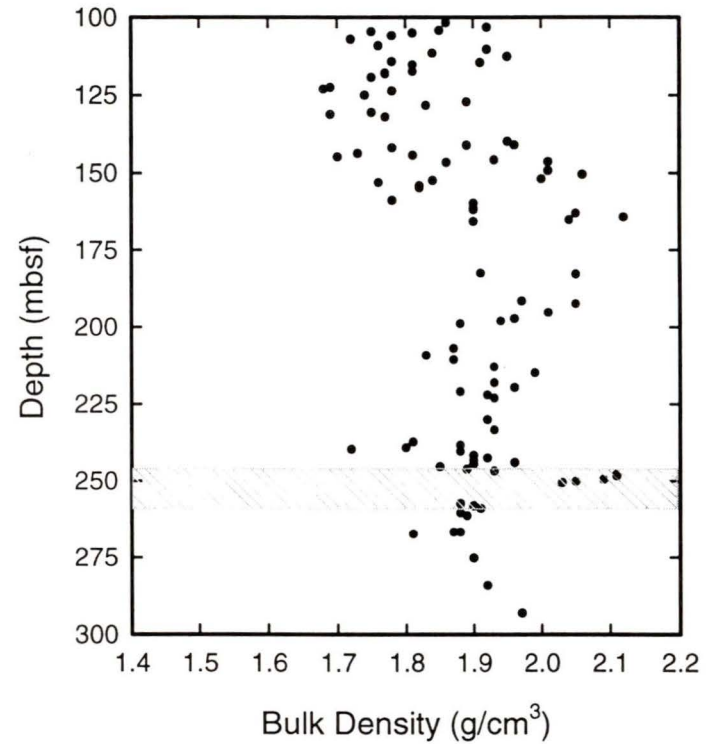
4.5.1 Model Preparation

A seawater velocity of 1480 m/s was selected, consistent with that from L89-08 [Yuan et al., 1994] and direct water column velocity measurements from a seismic survey near Site 889 in May, 1997 [Chapman and Walia, Cruise Report, 1998]. The velocity-depth function below the seafloor followed the vertical seismic profiling (VSP) interval velocities at Sites 889/890 [MacKay et al, 1994]. The VSP velocity function included interval velocities as low as 1520 m/s below the BSR, which was interpreted to be the effect of free gas. The shallowest VSP interval velocity was at 67 mbsf (figure 4.6 a). A velocity of 1500m/s, about the same as that of seawater, was assigned to the seafloor sediment and the velocity from 0 to 67 mbsf was linearly interpolated, following the velocity variation of the sonic log. The thickness between the primary and the secondary BSR was set to 22.5m, using a velocity of 1500m/s. The velocity function was uniformly blocked into 3 m-thick layers for the convenience of thickness adjustment.

Sonic and VSP Velocity at Hole 889A and 889B



Core Bulk Density of Hole 889 A



889A VSP ——— 889B Sonic 889A Sonic - - - - - Forward Modeling Velocity

Figure 4.6 (a) Sonic and VSP velocities at hole 889a and 889b. The 100m thick high velocity zone above the BSR is interpreted as the result of sediment being cemented by high velocity gas hydrate. The velocity enhancement should be considered as minimum because of the disassociation of gas hydrate during drilling. Velocity decrease observed in VSP velocity is sharp while that at 889B is rather gradual.

(b) There is a fairly large change of bulk density from 1.90 g/cm³ to 2.10 g/cm³ at 249 mbsf, which is about 25 ms deeper than the seismically determined BSR depth.

The negative acoustic boundary indicated by the secondary BSR can be produced by two velocity configurations, (1) A high velocity zone over a normal background velocity or (2) a normal background velocity zone over a low velocity zone. In both of the two velocity configurations, following the VSP measurements, the sediment velocity immediately drops to 1500 m/s for the free gas charged sediment from 1760 m/s of hydrated sediment, giving a typical BSR reflection. Below the BSR, in configuration (1), the velocity first increases to 1750 m/s and then decreases to a normal background velocity of 1650 m/s; in configuration (2), the velocity first increases to normal background velocity then decreases to a low velocity of 1500 m/s.

The bulk density profile followed the core bulk density variation trend at Site 889/890. Because there was no sediment recovered from 0mbsf to 20.2mbsf at Hole 889A, an average seafloor bulk density of 1600 kg/m^3 derived from the measurements on those piston cores was assigned to the seafloor. The values between were linearly interpolated. A constant bulk density of 1920 kg/m^3 was used across the primary and secondary BSR with the assumption that the density between them did not vary. The density values were blocked into 3 m thick layers and were smoothed by ignoring large fluctuation in thin layers (<3 m).

The input wavelet was extracted by averaging 100 stacked traces of the seafloor reflection in the region where the secondary BSR was resolved. It had a dominant frequency of 75Hz and was roughly minimum phase. The time response, amplitude spectrum and phase spectrum are shown in figure 4.7. Synthetic seismic data were calculated using Hampson Russell AVO modeling package.

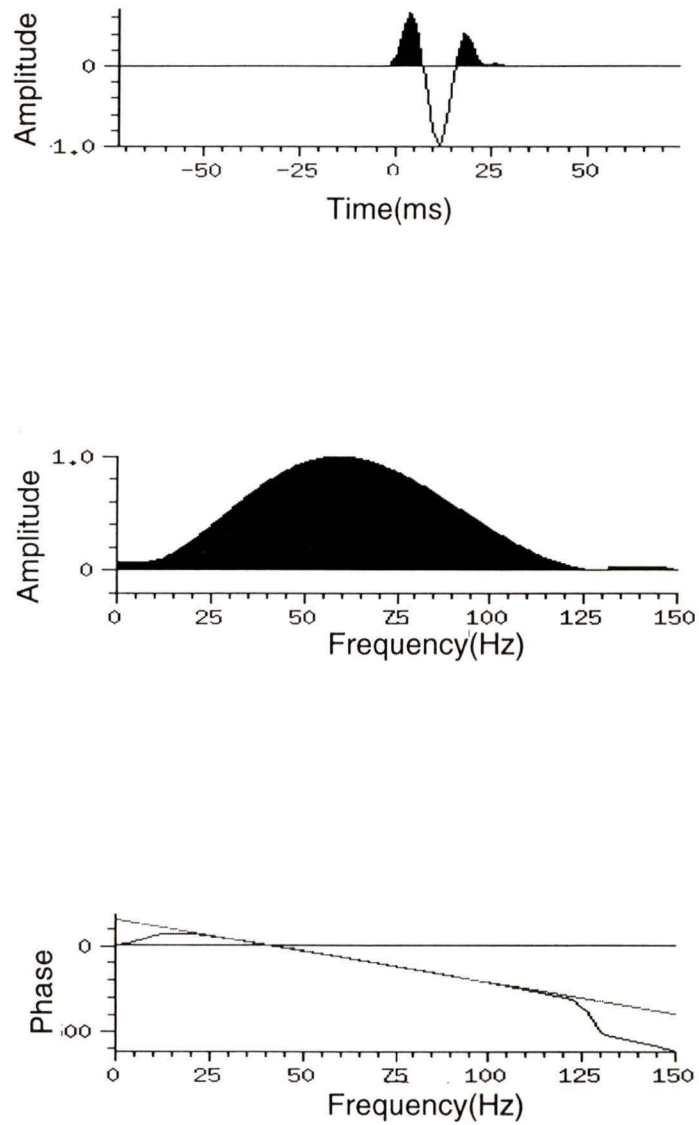


Figure 4.7 Time response, amplitude spectrum and phase spectrum of the wavelet used in forward modeling. Wavelet was extracted statistically from the real seismic data where the second BSR was observed.

4.5.2 Modeling Results: Upper bound of Thickness, Velocity and Density Contrast at the Secondary BSR

Both of the two velocity configurations gave rather good waveform matches to the real seismic data (figure 4.8). To evaluate the effect of bulk density variation on the secondary BSR, a slight bulk density decrement at the depth of the secondary BSR, from 2020 kg/m^3 to 1920 kg/m^3 , was used in the first velocity configuration. A slight bulk density decrease did not have much effect on the general waveform, while the amplitude of the secondary BSR was slightly increased. Further tests on the waveform variation with the thickness of the layer below the primary BSR showed that the waveform simulated that of the seafloor for thickness equal to or less than 12 m. A 15 m thickness generates a rather broad waveform in which the primary and the secondary BSR are still separable (figure 4.9).

4.6 Interpretations of Velocity and Density Structures Across BSRs

Based on the two velocity and density structures determined from the forward modeling, there are two corresponding interpretations.

4.6.1 Single Free Gas Zone and An Overconsolidated Layer

For velocity case 1, in which the velocity drops to background sediment velocity from higher values, we propose the presence of an overconsolidated sediment layer which is located immediately below the primary BSR and which terminates at the secondary BSR. The thickness of this layer is increased by periodic formation and dissociation of gas hydrate. At the time of hydrate formation, water is extracted from the sediments, which leads to higher density and velocity [Hovland et al, 1995].

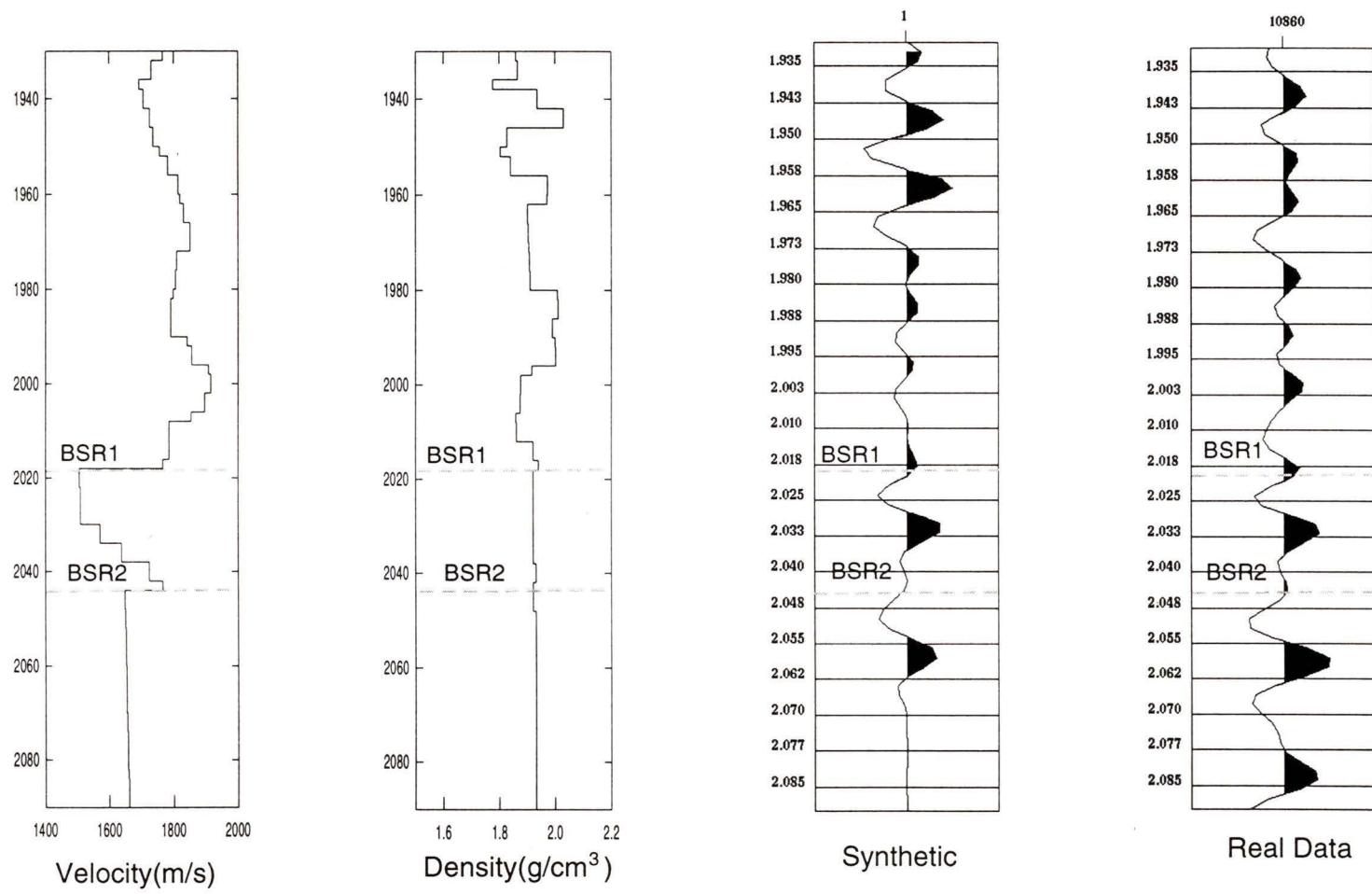


Figure 4.8 a. Velocity configuration I: High velocity over background velocity at the depth of second BSR. using constant density.

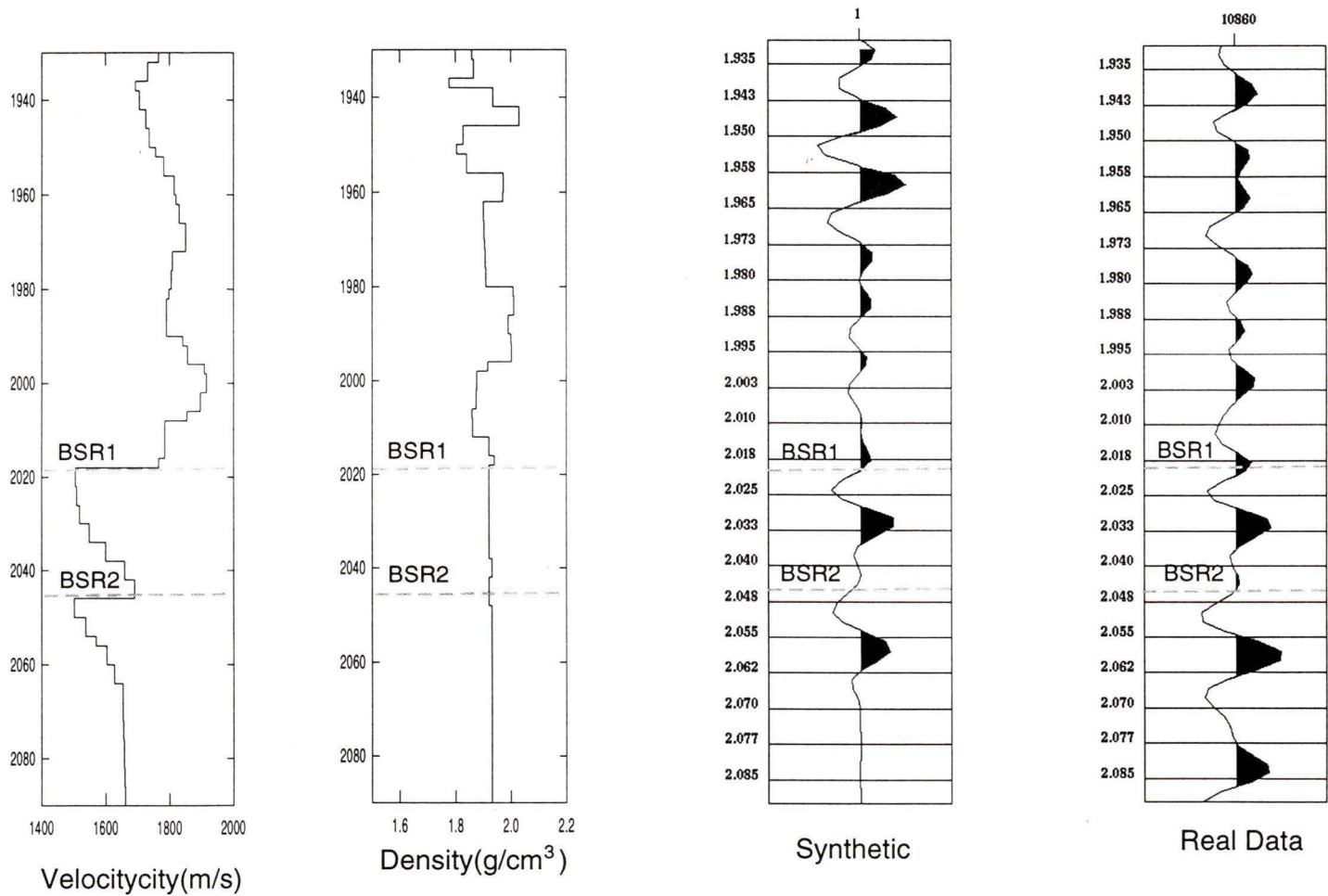


Figure 4.8 b. Velocity configuration I I: Background velocity over low velocity at the depth of second BSR. using constant density.

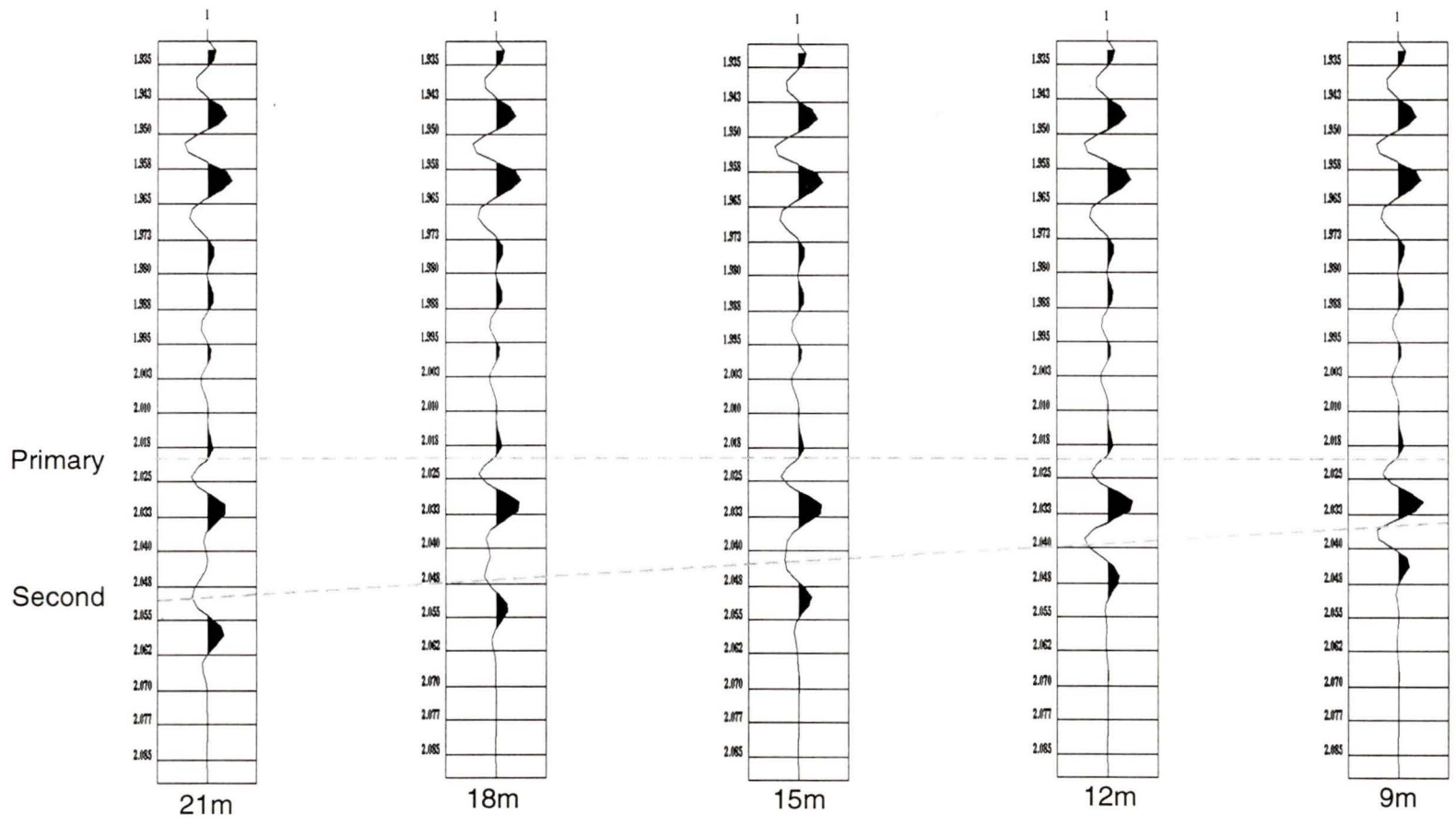


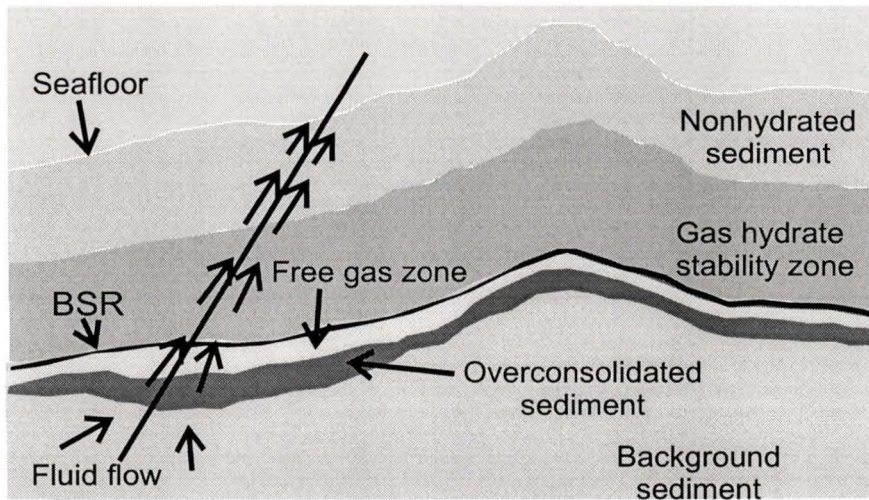
Figure 4.9 Primary and second BSR waveform variation with the thickness of the gradient velocity zone below the primary BSR. Their waveform simulates that of seafloor when thickness is less than 12 m,

Further hydrate formation and dissociation can only increase its density and hence velocity because the compaction process is non-reversible. The top portion of this over-consolidated layer is gas-charged so that it has lower velocity than either hydrated sediment or background sediment, while the bottom portion has higher velocity than background sediment so that a negative acoustic boundary is generated. As the base of the hydrate stability zone migrates upward, this layer can get thick enough so that its base can be resolved as a separate reflector.

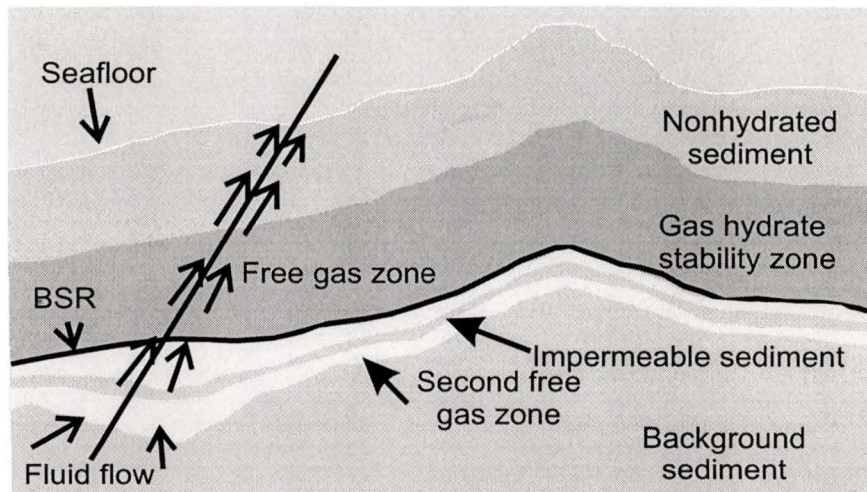
The periodic hydrate formation and dissociation may be controlled by the local seafloor-BSR penetrating fault zone. Active faults are good fluid migration channels. The activity of the fault zones enhances local fluid migration rates and promotes the dissociation of hydrate by increasing the local thermal gradient. The fluid migration rates may rebound to normal when the faults are closed, so that hydrate may form again in the zone which it used to occupy (figure 4.10 a).

As evidence of water extraction by gas hydrate formation from sediments, an unusually high water content clay layer up to 2m thick has been recovered within the gas hydrate stability zone in ODP Leg 146 at Site 892. [Westbrook et al., 1994]. This sediment was first believed to have been severely disturbed by the drilling process, but was later described as “soupy” or “mousse-like” because of the excessive water content. The pore fluid within this layer was also found to be Cl-depleted. They were therefore concluded to have contained gas hydrate, which had dissociated during the drilling process.

Water-depleted sediment was clearly observed at Site 892D. At 67.7 mbsf at Site 892, roughly the BSR depth, gamma ray attenuation porosity evaluation



(A) Higher velocity above second BSR is due to overconsolidated sediment.



(B) Lower velocity below second BSR is due to a second gas layer.

Figure 4.10 Two interpretation of the formation mechanism of the second BSR.

(GRAPE) measurements and index property measurements show a consistent sharp increase of bulk density from 1700 kg/m^3 to 2000 kg/m^3 , accompanied by a porosity decrease from 55% to 42%, as shown in figure 4.11. The sediment in this zone is highly fractured according to the core description.

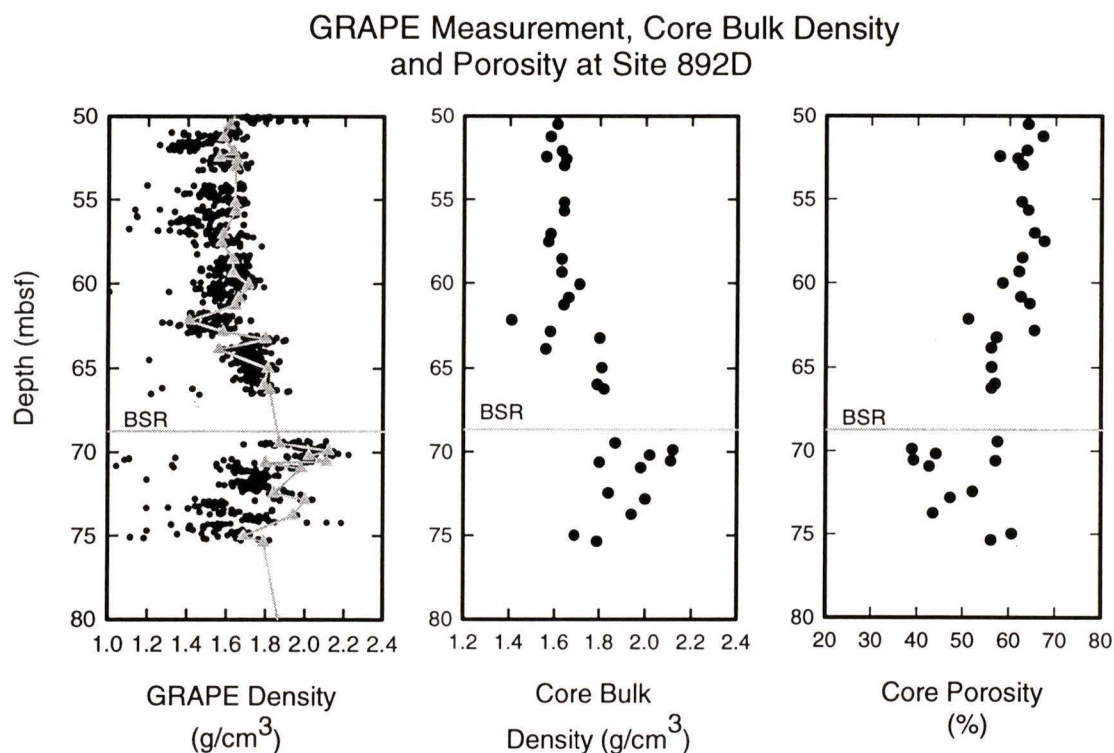


Figure 4.11 GRAPE density, core bulk density and porosity at Site 892. Water depleted sediment was clearly observed at Hole D. At 67.7mbsf, roughly the BSR depth, GRAPE density measurement and core bulk density measurement show consistent sharp increment of from 1.7 g/cm^3 to 2.0 g/cm^3 , accompanied by sharp porosity decrement from 55% to 42%. The sediment in this zone is very seriously fractured according to the core description.

The density contrast across the BSR at ODP Sites 889/890 is not as clear as that at Site 892. There does exist a fairly large change of bulk density from 1900 kg/m^3 to 2100 kg/m^3 at 249 mbsf (figure 4.6 b), which is about 25 m deeper than the seismically determined BSR depth. If this density change indicates the actual base of the gas hydrate zone, the velocity derived from the VSP used in estimating the BSR

depth should be generally 10% higher. This is unlikely to be true because VSP velocities are believed to be the best velocity measurements and because an excellent match was obtained between synthetic seismic data and the real seismic data at the drilling site.

The difference of density contrast at the two sites can be explained with their depth. The BSR appears at only about 74 mbsf where sediment normally has higher water content and lower bulk density. Water can be extracted more easily at this depth than from the sediment at a depth of 250 mbsf, where water content is lower and the bulk density is higher. Thus the deeper the BSR is, the less the corresponding density contrast.

4.6.2 The Presence of A Second Free Gas Zone

For velocity case 2, in which velocity drops from background sediment velocity to a low velocity compared with the free gas zone below the primary BSR, we propose the presence of a second free gas zone which is separated by a impermeable sediment layer from the first gas zone. In this case, the top of the second free gas zone is marked by the secondary BSR, while the bottom is not well constrained due to lack of reflection from the zone below (figure 4.10 b).

This reflection sequence is to some extent similar to that at Blake Ridge, where numerous reflections within a thick low velocity zone below the primary BSR indicates that free gas is trapped in numerous stratigraphic layers. The BSR itself is not the sole indicator of free gas, but simply marks the shallowest level at which free gas may be present. Compared with the 30 m-thick zone offshore Vancouver Island,

the free gas below the BSR at Blake Ridge may distribute in a series of zones over a 250 m-thick layer [Holbrook et al, 1996].

Chapter 5 Conclusions

Following the above discussion on the physical property analyses, seafloor and BSR reflection coefficient calculations, free gas and hydrate saturation estimation and forward modeling of a secondary BSR, we can draw the following conclusions:

1: The porosity-depth function for the topmost 6-7 m of sediment is different from the deeper trend. The exponential decay constant for porosity reduction is only 60 m for the shallow layer, in contrast to a value of 1500 m for the accretionary wedge sediments down to a depth of several kilometers. The shallow layer should be treated as a different unit which has not yet undergone the compaction process as that of deeper sediment.

2: Porosity is reliably predictable from resistivity (formation factor) measurements using Archie's Law. Archie's Law parameters from Site 888 and Site 889/890 are very close to the optimum parameters for data set I.

3: The contrast in seismic velocities at the seafloor is very small, as determined from the core velocity measurements. The reflectivity at the seafloor is mainly caused by the bulk density contrast between seawater and seafloor sediments. Average bulk density is 1650 kg/m^3 for the shallow water region and 1300 kg/m^3 for the deep water region. The corresponding reflection coefficients calculated from bulk densities are 0.23 and 0.11, respectively. In the shallow water region, the difference between average seismic reflection coefficient (0.20) and the bulk density reflection coefficient may be due to scattering. For 75 Hz frequency, simple scattering models predict a value of 0.95 m for the length scale of seafloor roughness. The difference of

seismic reflection coefficients between shallow-water and deep-water regions may be due to an intermediate-density layer at the seafloor, which is only ten's of centimeters in thickness in the shallow-water region but up to 2-3 m thick in the deep-water region.

4: The high seafloor reflection coefficients on the west flank of a local topographic high may indicate enhanced fluid flow in this region.

5: The BSR reflection coefficients have a slight correlation with the topographic high (not as strong as that in the adjacent survey region to the east as reported by Fink & Spence (1998)). Strong correlation with topographic highs is not a universal observation. Typical values range from 0.025 to 0.12, with the majority values of from 0.03 to 0.08, which corresponds to hydrate saturations between 5% and 15% of the pore space. The hydrate saturation, derived from the BSR reflection coefficient by using velocities from 1600 m/s to 1640 m/s for background sediment and a velocity of 1515 m/s for gas charged sediments, has maximum values of more than 15% on the local topographic high and its west flank. Free gas saturation remains difficult to estimate, but we can safely conclude that gas saturation should be less than 5% of the pore space.

6: A secondary BSR was observed about 16-30 ms below the primary BSR in a restricted region where local seafloor-BSR penetrating faults are present. Forward modeling shows two possible velocity configurations, which corresponds to an overconsolidated sediment layer and a second free gas zone. The waveforms of the primary and secondary BSR merge to a simple polarity-reversed version of the seafloor reflection if the distance between them is less than 12 m.

BIBLIOGRAPHY

Atkins, P.W., Physical Chemistry, 4th ed., New York, Freeman, 1990.

Brooks, J.M., H.B. Cox, W.R. Bryant, M.C. Kennicutt II, R.G. Mann, and T.J. MacDonald, 1987. Association of gas hydrate and oil seepage in the Gulf of Mexico: *Advanced Organic Geochemistry*, v 10, p. 221-234.

Courtney, R.C. and L. Mayer, Acoustic properties of fine-grained sediments from Emerald Basin: Toward an inversion for physical properties using the Biot-Stoll model, *Journal of Acoustical Society of America*, 93, 3193-3200.

Davis, E.E., Hyndman, R.D., and Villinger, H., 1990, Rate of fluid expulsion across the northern Cascadia accretionary prism: constraints from new heat flow and multichannel seismic reflection data, *Journal of Geophysical Research*, 95, 8869-8889.

Davis, E.E., and Hyndman, R.D., 1989, Accretion and recent deformation of sediments along the northern Cascadia subduction zone, *Geological Society of America Bulletin*, 101, 1465-1480.

Davis, E.E., and Riddihough, R.P., 1982, The Winona basin: Structure and tectonics, *Canadian Journal of Earth Sciences*, 19, 767-788.

Dickens, G.R., and Quinby-Hunt, M.S., 1994, Methane hydrate stability in seawater, *Geophysical Research Letters*, 21, 2115-2118.

Domenico, S.N., 1976, Elastic properties of unconsolidated porous sand reservoirs, *Geophysics*, 42, 1339-1368.

Englezos, P., and Bishnoi, R.P., 1988, prediction of gas hydrate formation in aqueous solutions, *American Institution of Chemical Engineers*, 34, 1718-1721.

Fink, R.F., 1995, Methane gas hydrate distribution offshore Vancouver Island from detailed single channel seismic studies, master's thesis.

Fink, R.F. & Spence, G.D., 1998, Hydrate distribution off Vancouver Island from multi-frequency single channel seismic reflection data, revised draft for submission to *Journal of Geophysical Research*, June, 1998.

Ganguly, N., Spence, G.D., Hyndman R.D., 1998, Heat flow variations from bottom simulating reflector on the Cascadia margin, revised draft for submission to *Marine Geology*, July, 1998.

Geertsma, J., 1961, Velocity-log interpretation: The effect of rock bulk compressibility, *Society of Petroleum Engineering Journal*, 1, 235-248.

Ginsburg, G.D., Soloviev, V.A., 1997, Methane migration within the submarine gas-hydrate stability zone under deep-water conditions, *Marine Geology*, 137, 49-57.

Hamilton, E.L., 1982 Acoustic properties of sediment, in *Acoustics and Ocean Bottom*, edited by Lara-Saenz, C. Ranz-Guerra, C. Carbo-Fite, pp 3-58.

Heffler, D., Atlantic Geoscience Centre Technical Report (902-426-6367): Core Resistivity, 1992.

Holbrook, W.S., H. Hoskins, W.T. Wood, R.A. Stephen, D. Lizarralde, Leg 146 Scientific Party, 1996, Methane Hydrate and free gas on the Blake Ridge from Vertical Seismic profiling.

Hovland, M., Lysne, D. and Whiticar, M.J.. 1995, Gas hydrate and sediment gas composition, Hole 892A. In Proceeding of the Ocean Drilling Program, Scientific Results, eds B. Carson, G.K. Westbrook, R.J. Musgrave and E. Suess, 146(Pt.1),151-161.

Hovland, M., Clennell, M.B., Lekvam, K.. 1997, Gas hydrate and free gas volumes in marine sediments: Example from the Niger Delta front, *Marine and petroleum geology*, v14 n3, 245.

Hyndman, R.D., and Spence, G.D., 1992, A seismic study of Methane hydrate marine Bottom simulating Reflectors, *Journal of Geophysical Research*, 97, 6683-6698.

Hyndman, R.D., and E.E. Davis, 1992, A mechanism for the formation of methane hydrate and seafloor bottom simulation reflectors by vertical fluid expulsion, *Journal of Geophysical Research*, 97, 7025-7041.

Hyndman, R.D., Yorath, C.J., Clowes, R.M., and Davis E.E., 1990, The northern Cascadia subduction zone at Vancouver Island: seismic structure and tectonic history, *Canadian journal of Earth Sciences*, 27, 313-329.

Hyndman, R.D., Riddihough, R.P., and Herzer, R., 1979, The Nootka fault zone – A new plate boundary of western Canada, *Royal Astronomical Society Geophysical Journal*, 58, 667-683.

Kvenvolden, K.A. and M.A. McMennamin, 1980, Hydrate and natural gas: a review of their geological occurrences, U.S. Geological Survey Circular No. 825.

Kvenvolden, K.A. and McDonald, T.J., 1985, Gas hydrate of middle America trench – DSDP leg 84, edited by R. von Huene, et al., in *Initial Reports Deep Sea Drilling Project*, 84, 667-682.

Kvenvolden, K.A., Ginsburg, G.D., Soloviev, V.A., Worldwide distribution of subaquatic gas hydrate, *Geo-marine letters*, 1993 v13n1, 32.

MacDonald, G.T., 1983, The many origins of natural gas, *Journal of Petroleum Geology*, 5:341-362.

MacDonald, G.T. 1990, The future of methane as an energy resource, *Annual Reviews of Energy*, 15, 53-83.

MacKay, M.E., Jarrard, R.D., Westbrook, G.K., Hyndman, R.D. and the Shipboard Scientific party of ODP Leg 146(1994), Origin of bottom-simulating reflectors: Geophysical evidence from the Cascadia accretionary prism. *Geology* 22,459-462.

Makogon, Y.F., 1974, *Hydrates of Natural Gas*, Nedra. Moscow, Russia.

Miller, J.J., M.W. Lee and R. von Huene, 1991, An analysis of a seismic reflection from the base of a gas hydrate zone, offshore Peru, *American Association of Petroleum Geologists Bulletin*, 75, 910-924.

Mishull, T. and R. White, 1989, Sediment compaction and fluid migration in the Makran accretionary prism, *Journal of Geophysical Research*, 94, 7387-7402.

Pearson, C.F., Halleck, P.M., McGuire, P.L., R. Hermes and M. Mathews, 1983, Natural gas hydrate: A review of in situ properties, *Journal of Physical Chemistry*, 87, 4180-4185. et al., 1983.

Potential Gas Committee, 1981, Potential supply of natural gas in the United States (as of December 31, 1980, Potential Gas Agency, Colorado School of Mines, Golden, Colo.

Riddihough, R.P., 1984, Recent movement of the Juan de Fuca plate system, *Journal of Geophysics Research*, 89, 6980-6994.

Ripmeester, J.A., Ratcliffe, C.A., Kluf, D.D., Tse, J.S., in (First) International Conference on Natural Gas Hydrates, *Annals of New York Academy of Sciences*, (Sloan, E.D., Happel, J., Hnatow, M.A., eds.), 715, 161 (1994)

Rogers, J.C. & J.L. Morak, 1980, Geophysical evidence of shallow nearshore permafrost, Prudhoe Bay, Alaska, *Journal of Geophysical Research*, 85(B9), 4845-4853.

Shine, K.P., R.G. Derwent, D.J. Wuebbles & J-J. Morcrette, 1990, Radiative forcing of climate. In *Climate Change, The IPCC Scientific Assessment*. J.T. Houghton, G.J. Jenkins & J.J. Ephraums, Eds.: 1-40, Cambridge University Press, Cambridge England.

Shipley, T.H. and Didyk, B.M., 1981, Occurrences of methane hydrate offshore southern Mexico, in *Initial Reports, Deep Sea Drilling Project*, 66,547-555.

Sloan, E.D., 1990, *Clathrate hydrates of natural gases*, 641 pp., Marcel Dekker, New York.

Spence, G.D., Hyndman, R.D., Davis, E.E., and Yorath, C.J., 1991a, Multichannel reflection profiles across the Vancouver Island continental shelf and slope, *Geological Survey of Canada, Open File No. 2391*.

Spence, G.D., Hyndman, R.D., Davis, E.E., and Yorath, C.J., 1991b, Seismic structure of the northern Cascadia accretionary prism: Evidence from new multichannel seismic reflection data, in *continental Lithosphere, Deep Seismic*

Reflections, edited by Meissner, et al., Geodyn. Ser. Vol. 22, pp. 257-263, AGU, Washington, D.C..

Sloan, E.D., 1990, Clathrate hydrates of natural gases, 641 pp., Marcel Dekker, New York.

Soloviev, V.A., Ginsburg, G.D., Water segregation in the course of gas hydrate formation and accumulation in submarine gas-seepage field, *Maine Geology* 137, 59-68, 1997.

Stoll, R.D., 1974, Effect of gas hydrate in sediments, 1974, in *Natural Gases in Marine Sediments*, edited by Kaplan, I.R., 235-248, Plenum, New York.

Stoll, R.D., Ewing, J., and Bryan, G.M., 1971, Anomalous wave velocities in sediments containing gas hydrate, *Journal of Geophysical Research*, 76, 2090-2094.

Watson, R.T., H. Rhodhe, H. Oeschger & U. Siegenthaler, 1990, Radiative forcing of climate. In *Climate Change, The IPCC Scientific Assessment*. J.T. Houghton, G.J. Jenkins & J.J. Ephraums, Eds.: 1-40, Cambridge University Press, Cambridge England.

Whalley, E., 1980, Speed of longitudinal sound in clathrate hydrate, *Journal of Geophysical Research*, 85, 2539-2542.

Westbrook, G.K., Carson, B., Musgrave, R.J., et al., (Eds.), 1994, *Proceedings of the ODP, Initial Reports, 146(Part I)*, College Station, TX (Ocean Drilling Program).

Yamamoto, T., 1995, Acoustic scattering in the ocean from velocity and density fluctuations in the sediments, *Journal of Acoustical Society of America*, 99, 866-879.

Yamanoto, M., Foucher, J.P., Kinoshita, M., Fisher, A., Hyndman, R.D., 1992ODP Leg 131 Shipboard Scientific Party, Heat flow and fluid flow regime in the western Nankai accretionary prism, *Earth and Planetary Science Letters*, 109, 451-462.

Yetsepina, O.Y., Buffet, B.A., Phase equilibrium of gas hydrate: Implications for the formation of hydrate in the deep-sea floor, *Geophysical Research Letters*, 1567, Jul 01, 1997, v24 n13, 1997.

Yuan, T., Hyndman, R.D., Spence, G.D., and Desmons, B., 1996, Seismic velocity increase and deep-sea gas hydrate concentration above a bottom-simulating reflector on the northern Cascadia continental slope, *Journal of Geophysical Research*, 101, 13,655-13,671.

Yuan, T., Spence, G.D., Hyndman, R.D., 1994, Seismic velocities and inferred porosities in the accretionary wedge sediment at the Cascadia margin, *Journal of Geophysical Research*, 99, 4413-4427.

Zonenshain, L.P., Murdmaa, I.O., Baranov, B.V., Kuznetsov, A.P., Kuzin, V.S., Kuzmin, M.I., Acdeiko, G.P., Stunzhas, P.A., Lukashin, V.N., Barash, M.S., Valyashko, G.M. and Dyomina, L.L., 1987, An underwater gas source in the Sea of Okhotsk west of Paramushir Island. *Oceanology*, 27(5), 598-602.

Vita

Surname: Mi

Given Name: Yanpeng

Place of Birth: Tong County, Beijing, People's Republic of China

Educational Institutions Attended:

University of Victoria 1996 to 1998

Peking University 1990 to 1995

Degree Awarded:

B.Sc. in Geosciences Peking University 1995

Honours and Awards:

Peking University Undergraduate Student Guanghua Prize 1993

PARTIAL COPYRIGHT LICENSE

I hereby grant the right to lend my thesis to users of the University of Victoria Library, and to make single copies only for such users or in response to a request from the Library of any other university, or similar institution, on its behalf or for one of its users. I further agree that permission for extensive copying of this thesis for scholarly purpose may be granted by me or a member of the University designated by me. It is understood that copying or publication of this thesis or financial gain shall not be allowed without my written permission.

Title of Thesis:

Seafloor Sediment Coring and Multichannel Seismic Studies of Gas Hydrate,
Offshore Vancouver Island

Author

A black rectangular redaction box covers the author's name. A horizontal line extends from the right side of the box.

Yanpeng Mi

August 10, 1998